

A COMPUTATIONAL MODEL OF NANOPARTICLE GROWTH

FROM SPARK ABLATION

B. E. VAN DER MAESEN

to obtain the degree of Master of Applied Mathematics
Computational Science & Engineering Track
to be defended publicly on November 16, 2018

DELFT UNIVERSITY OF TECHNOLOGY
Faculty of Electrical Engineering, Mathematics & Computer Science
Delft Institute of Applied Mathematics
Numerical Analysis Group

Bibianne E. van der Maesen *A Computational Model of Nanoparticle Growth,
from Spark Ablation,* November 16, 2018

STUDENT NUMBER:
4230426

THESIS COMMITTEE:
Prof. dr. ir. A. W. Heemink
Dr. ir. M.B. van Gijzen
Dr. M.F.J. Boeije

SUPERVISORS:
Dr. ir. M.B. van Gijzen
Dr. M.F.J. Boeije

ABSTRACT

Though the commercialization of nanotechnology began only 30 years ago, it has developed into one of the fastest growing industries in terms of research and design, with an unlimited amount of possibilities that will transform industries from how we know them today. The advancement of nanotechnology relies on the actual production, control and integration of nanoparticles. VSPARTICLE is a nano start-up which developed the VSP-G1, a generator that produces nanoparticle aerosols using a gas-phase process called spark ablation.

The aim of this thesis is to develop and validate a computational model of the nanoparticle production process in the VSP-G1. Such a model will simulate the effect of certain physical mechanisms on the composition of the produced aerosol and track the corresponding particle size distribution (PSD) throughout the production process.

Brownian coagulation and diffusion are identified as main aerosol mechanisms and form the mathematical basis of the model. Approximation formulas provide the initial conditions which directly depend on the VSP-G1 input parameters. The Log-Normal Method of Moments (Log-MoM) is used to approximate the model by deriving the geometric mean, standard deviation and total particle concentration of the PSD. Last, the solution is computationally approached using the Forward Euler numerical method.

A theoretical and experimental validation proved a sufficient accuracy of the model with respect to nanoparticle growth in the VSP-G1. In particular, the predictions of the mean particle size maintained nanometer accuracy in compliance with experiments. To assist future research, accuracy ranges are presented that provide compliance criteria between the modelled results and the actual output of the VSP-G1. Finally, an improved function for the particle size evolution due to pure, monodisperse coagulation is derived based on the experimental validation process.

The computational model will provide researchers with an analysis regarding the sensitivity of the VSP-G1 input parameters. Furthermore, the model framework, consisting of mathematical and physical processes, will provide a better scientific understanding of the system. Finally, the model can contribute to the production of pure, tailor-made nanoparticles by performing as an operational guide for the VSP-G1.

Bibianne van der Maesen
November, 2018

PREFACE

Every since I was little I expressed my interests in engineering, physics and mathematics. At age ten, I willingly studied the structure of the Eiffeltower before going to Paris on a family vacation. I discovered the high stability and strength of triangles to that of squares by performing self-made tests with K’NEX (a toy construction set similar to Lego). It was no surprise that I enrolled in a Civil Engineering Bachelors after I graduated high school. My bachelor thesis involved the development of a morphological, computational model of the sediment transport in the Wadden Sea. It was during this project that I realized that every physical process on Earth can be linked to a set of mathematical equations, and that in combination with a computer, it is possible to simulate reality. I needed to learn more.

Dr. ir. Martin van Gijzen, guided me through the transition program that allowed me to enroll in Applied Mathematics MSc. Even though I hadn’t followed any of his courses throughout the curriculum, it was a no brainer to ask him as my first supervisor for my thesis research. We took about three months to find the ideal thesis topic: a computational modelling project that allowed me to work through all phases of the development and validation processes. A special thanks to Martin for introducing me to Applied Mathematics in the first place, guiding me through the number of possible thesis topics, and for our weekly meetings once the project was up and running. Without your quick feedback I would have certainly have lost sight of the big picture.

Moreover, I would like to thank my company supervisor Maurits, for always begin happy to answer daily questions and pushing me to get the most out of this research. Most importantly, you’ve provided the experimental data that proves the success and accuracy of the model, contributing greatly to the positive result of this thesis.

For the people at VSPARTICLE, a big thanks for providing me with the needed equipment, time and friendly environment which motivated me to give it my best each day. A special thanks to Aike for bringing met on board in the first case, and Tobias for making time to be my sparring-partner in times when I got lost. Jurrian, thanks for teaching me the PYTHON basics, and finally my fellow graduate Tijmen; thanks for *always* begin on the same page as me in terms of work, motivation and humor.

I would like to thank the friends and family who helped me with visual thinking and Illustrator skills, and for supported me in moments where personal frustration took the overhand. Finally, I would like to thank my grandfather, Felix van der Maesen. Even though you left us long before we got to share our common fascination for physics and maths, I know that you would’ve been proud to watch me become a mathematician. This thought gave me the courage to switch to maths in the first place and has never left the back of my mind since.

CONTENTS

LIST OF FIGURES	VII
LIST OF TABLES	IX
1 INTRODUCTION	3
1.1 VSP-G1	4
1.2 research goal and approach	5
2 MATHEMATICAL MODEL	7
2.1 smoluchowski equation	7
2.2 coagulation	8
2.2.1 free molecular regime	9
2.2.2 continuum regime	9
2.2.3 transition regime	10
2.3 diffusion	11
2.4 mathematical model	11
2.5 agglomerates	12
3 METHOD OF MOMENTS	15
3.1 moment governing equation	15
3.2 derivation of odes using log-normal mom	17
3.2.1 log-normal method of moments	17
3.2.2 free molecular regime	18
3.2.3 continuum regime	19
3.2.4 transition regime	20
3.2.5 sink term	21
4 NUMERICAL ANALYSIS	23
4.1 numerical methods	23
4.2 stepsize	24
4.3 order of error	26
4.4 computational efficiency	27
4.5 conclusion	27
5 VALIDATION WITH THEORETICAL RESULTS	29
5.1 validation of mom	29
5.2 transition regime	32
5.3 diffusion effects	33
6 VALIDATION WITH EXPERIMENTAL RESULTS	37
6.1 process	38
6.1.1 experimental set-up	39
6.1.2 data conversion	40
6.1.3 uncertainties on measurements	41
6.2 approximation formulas	42
6.2.1 initial concentration	42
6.2.2 residence time	44
6.3 results	45
6.4 an improved formula for the mean particle size	47

7	DISCUSSION	49
7.1	choices for mathematical equations	49
7.2	solution method	50
7.3	error analysis	51
7.4	experimental results	51
8	CONCLUSIONS	53
	BIBLIOGRAPHY	55
A	MODEL FRAMEWORK MATHEMATICAL EQUATIONS	57
A.1	smoluchowski.	57
A.2	cunningham frequency constant	57
B	SOLUTION METHOD	59
B.1	overview of functions in model equation	59
C	EXPERIMENTAL RESULTS	61
C.1	experimental and modelled results	61
C.2	quantifying deposition for crossflow	62
C.2.1	experimental set-up	62
C.2.2	results	64
C.2.3	possible explanations	64
C.3	properties of airborne particles from Hinds [1]	67

LIST OF FIGURES

1.1	Nanoparticle size on a comparative scale.	3
1.2	Nanoparticle production process of the VSP-G1 (through flow).	4
1.3	Framework of physical model for crossflow.	5
2.1	Particle dynamics in continuum, transition and free-molecular regime [2–4]. gas particle (grey), solid particles (green)	8
2.2	Knudsen number and regimes based on the particle diameter at room temperature . .	9
2.3	Geometry of the collision model in the flux matching method [5]	10
2.4	Particle morphologies v.s. collision rate [3]	12
2.5	Agglomerate structures	13
4.1	Richardson Extrapolation performed on M_1 for Euler Forward.	25
4.2	stability regions for $\Delta\tau$ on $\Delta\tau\lambda$ -plane	25
4.3	Global Error for Forward Euler and Modified Euler numerical approximation methods. .	26
5.1	Computational model (left), theory from [6] (right), both free molecular regime.	31
5.2	Dimensionless particle size distribution converges to the self-preserving size distribution for initial conditions: $N_0 = 1e17$, $\sigma_0 = 1.8$ after around 1 s.	31
5.3	Asymptotic behaviour of geometric standard deviation generated by [7] (top) and model (bottom). Note, different x-scales are due to unknown scaling conditions in [7].	32
5.4	Characterizing dimensionless parameters N/N_0 , d/d_0 and σ under various N_0 in m^{-3} for the free molecular regime (left) and the entire regime (right).	33
5.5	Diffusion effects on the dimensionless total particle concentration (–) and dimensionless particle volume (–) for various σ_0 . Computational results (left), theoretical results (right) [8].	34
5.6	Diffusion effects on nanoparticle properties after 1 s for varying N_0 in cm^{-3}	35
5.7	particle size distribution for various moments in time, N_0 in m^{-3}	36
6.1	Experimental validation process.	38
6.2	Experimental Set-Up. VSP-G1 (A), tube (B), SPMS (C-E)	39
6.3	y-data transfer functions $f(ne)$	41
6.4	Hourly mass losses of gold electrodes for various power settings for $Q = 2lpm$	42
6.5	Standard Deviation of Power [%]	43
6.6	Deposition of particles on the electrode holder inside the G1	43
6.7	volume components relevant for the current validation process.	44
6.8	Modelled results (dots) vs. Experimental results (stars)	46
6.9	The model approximates the PSD of nanoparticles produced by the VSP-G1 within a certain range of accuracy.	46
6.10	(Geometric mean) particle diameter computed by the model $d_g(t)$: "–", monodisperse coagulation defined by Hinds [1] $d(t)_{coagulation}$: "–" and an improved function $d(t)_{new}$: "–". Note, sudden jumps occur in the results computed with Equation 6.11, these are due to the discrete values for K for a certain particle size range, tabulated in Appendix C.3.	47
6.11	Fit functions for coefficients m and K for the new formula for particle size increase due to coagulation over time.	48
7.1	[9] analyzing the behaviour of σ as a function of Kn for various models. Regime boundaries were added by this thesis.	50
7.2	A flowchart visualizing the relation between VSP-G1 inputs, model inputs, total concentration and particle size.	52

C.1	Diffusion validation using cross flow, gold electrodes and argon gas.	63
C.2	mass loss of electrode corresponding to mass of N_0 (green), experimental mass output (grey), modelled mass output (black)	64
C.3	Diffusion coefficients for transition- and free molecular regime	65
C.4	An increase in t_R does not close the gap between experimental- and modelled mass outputs.	65
C.5	Mass Output with A_a	66

LIST OF TABLES

2.1	coagulation constants for carrier gasses applicable for the VSP-G1 under standard conditions ³	10
4.1	Stability tests for various N_0 and h	24
4.2	Computational Efficiency tests	27
6.1	Coefficients for a_i in Function 6.7	41
6.2	Results from mass measurements for varying flow rates using gold electrodes and argon gas.	43
A.1	Parameters for Cunningham Slip Correction factor for different gasses in the transition regime according to [4] under standard conditions: $T_0 = 296.15$ K; $P_0 = 101.325$ kPa . .	57
C.1	Results corresponding to the validation process described in Chapter 6. Material = gold, gas = argon, flowtype = insert, tube length = 9 cm, ablation rate = 0.504 [nmol/J].	61
C.2	Properties of Airborne Particles[1], Calculated for standard density spheres at 293 K and 101 kPa.	67

LIST OF ABBREVIATIONS

CFD	Computational Fluid Dynamics
CPC	Condensation Particle Counter
DMA	Differential Mobility Analyser
DSA	Direct Simulation Algorithm
IVP	Initial Value Problem
LHS	Left Hand Side
MFA	Mass Flow Algorithm
MoM	Method of Moments
ODE	Ordinary Differential Equation
RHS	Right Hand Side
SMPS	Scanning Mobility Particle Sizer
SPSD	Self-Preserving Size Distribution
VSP-G1	VSPARTICLE - Generator 1

LIST OF SYMBOLS

Quantity	Symbol	Unit	Value
<i>Elementary Quantities</i>			
Activation Energy	E	J	
Current	I	mA	
Diameter	d	m or nm	
Dimensionless self-preserving size distribution	φ	-	
Electric Mobility	Z	$\text{m}^2\text{V}^{-1}\text{s}^{-1}$	
Exact Solution	y	-	
Flow rate	Q	lp m or m^3/s	
Gas Density	ρ_g	kg/m^3	
Gas viscosity	η	m^2s^{-1}	
Global error	e	-	
Jacobian matrix	J	-	
Knudsen number	Kn	-	
Length	L, l	m or nm	
Mean Velocity	\bar{u}	m/s	
Molecular mass	m_m	kgmol	
Numerical Solution	w	-	
Particle charge	ne	-	
Power	P	J/s	
Radius	r, R	m or nm	
Relative error	\bar{e}	-	
Spacial coordinate	z or x	m	
Stepsize	h	s	
Temperature	T	K	
Time	t	s	
Total amount of Setps	S	-	
Voltage	V	kV	
Volume	V	m^3 or cm^3	
<i>Defined Quantities</i>			
Ablation rate	m_A	mol/J	
Coagulation Constant, continuum	K_{Co}	m^3s^{-1}	
Coagulation Constant, free molecular	K_F	$\text{m}^{5/2}\text{s}^{-1}$	
Coefficient for non-linearisation of β_F	$b(\sigma)$	-	
Collision frequency kernel, continuum	β_{Co}	m^3s^{-1}	
Collision frequency kernel, Dahneke	β_D	m^3s^{-1}	
Collision frequency kernel, free molecular	β_F	$\text{m}^{5/2}\text{s}^{-1}$	
Concentration, particle number	N, n	cm^{-3} or m^{-3}	
Correction function for Dahnekes kernel	$a(\sigma)$	-	
Cunningham parameters	a, β, γ	-	
Cunningham Slip Correction Factor	$C(\text{Kn})$	-	
Diameter , solid particle	d_p	m or nm	

Quantity	Symbol	Unit	Value
Diameter, gas particle	d_g	m or nm	
Diameter, agglomerate	d_{ag}	m or nm	
Diameter, close packed	d_{cl}	m or nm	
Diameter, geometric mean	d_g	m or nm	
Diameter, singlet particle	d_s	m or nm	
Diffusion Coefficient	$D(r)$	m^2/s	
Dimensionless coefficient for b	$\tilde{B}(\tau_F)$	-	
Dimensionless k-th Moment	\tilde{M}_k	-	
Dimensionless k-th ODE, all	\tilde{f}_k	-	
Dimensionless k-th ODE, continuum	\tilde{h}_k	-	
Dimensionless k-th ODE, free molecular	\tilde{g}_k	-	
Dimensionless k-th ODE, sink	\tilde{l}_k	-	
Dimensionless self-preserving size distribution	φ	-	
Dimensionless time	τ	-	
Dimensionless timestep	$\Delta\tau$	-	
Geometric standard deviation	σ	-	
k-th Moment	M_k	m^{3k}	
Mass Fractal Dimension	D_F	-	
Mass, ablated (electrode mass loss)	$m_{\text{el, loss}}$	g/s	
Mean Free path	λ	m	
Mode of the PSD	d_M	m or nm	
Particle size distribution	$n(v, t)$	cm^{-3} or m^{-3}	
Radius, tube	R_t	m	
Raw particle counts	$y_{\text{raw}}(d_p)$	$\text{dp}^{-1}\text{m}^{-3}$	
Time, characterizing collision	t_C	s	
Time, characterizing sintering	t_S	s	
Volume, geometric mean particle	v_g	m^3	
Wiedensohlers charge distribution	$f(N_c)$	-	

<i>Constants</i>			
Boltzmann constant	k_B	$\text{m}^2\text{kg}/\text{s}^2\text{K}$	$1.38064852 \times 10^{-23}$
Avogadro's number	N_A	atoms mol^{-1}	6.0221409×10^{23}

1

INTRODUCTION

Nanoparticles are the smallest building blocks of all materials on Earth. In size, they range from 1 to 100 nm and consist of single or a combination of (in)organic molecules. To compare, the typical size of a nanoparticle to a football, is as a football to the Earth.

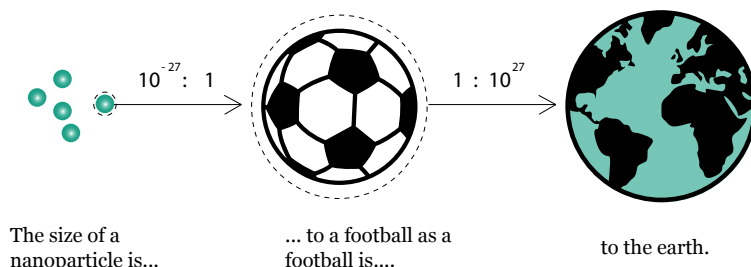


Figure 1.1: Nanoparticle size on a comparative scale.

While bulk materials have consistent physical properties regardless of their size, for nanoparticles the size dictates its physical and chemical properties [10]. For example, gold nanoparticles' interaction with light is strongly dependent on their size, resulting them to change in color to a rich red for particles in water of around 30 nm[11]. Graphite and its two-dimensional form: graphene is another example. Graphene was tested by MIT to be the strongest material ever known in 2009 [12], while graphite is so soft that it is used as ordinary pencil lead.

The ability to control material properties at nanoscale will allow the development of new materials with countless innovative applications in sectors like sustainable energy, health care and electronics. Although nanotechnology is a relatively new field of research, BBC Research revealed that the global nanotechnology market will increase from \$39.2 billion in 2016 to \$90.5 billion in 2021, growing at a five-year compound annual growth rate of 18.2% [13].

An essential part of the advancement of nanotechnology relies on the actual production, control and integration of nanoparticles. Traditionally, the production of tailor-made nanoparticles is performed with chemical techniques, often leading to material impurities and waste-streams. VSPARTICLE side-lined this approach by developing a system that makes producing nanoparticles as easy as pushing a button. The nanotech start-up was founded in 2014 and developed a user-friendly tool, the VSP-G1, which can produce any inorganic nanoparticle.

1.1. VSP-G1

The VSP-G1 is a nanoparticle generator that uses a physical process in the gas phase called spark ablation. This technique guarantees a user-friendly and fast production of ultra pure nanoparticles, making it ideal for aerosol research. The production process consist of three phases as is shown in Figure 1.2.

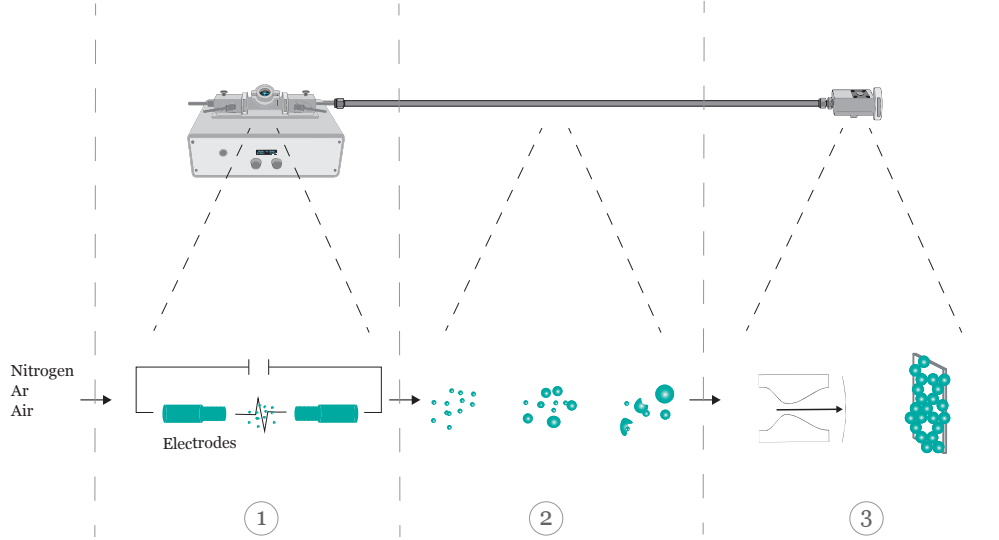


Figure 1.2: Nanoparticle production process of the VSP-G1 (through flow).

First, a potential difference causes a spark which locally evaporates a microscopic piece of the bulk material (electrodes). The material is ablated into single atoms forming a plasma of around 10^4 K in temperature [14]. At the same time, the vapor blends with a continuous flow of carrier gas, which is channeled perpendicular to- or through the electrodes. The gas is initially at room temperature and is composed of either nitrogen, argon or air. When vapor meets gas, the sudden drop in temperature causes the material to condensate, producing an aerosol of pure singlet nanoparticles [15] with a certain starting concentration N_0 . The aerosol leaving the reactor chamber is called "throughflow" when it is channeled through the electrodes and "crossflow" when channeled perpendicular to the electrodes. A third method attaches the tube, shown in phase two, with an "insert", extending the tube through the reactor chamber right to the spark.

In the second phase the aerosol is transported through a tube, allowing nanoparticles to interact due to Brownian Motion and various other mechanisms [14]. When two or more particles collide they either fuse into one larger, spherical particle or (loosely) stick together to form a non-spherical agglomerate. These mechanisms allow particles to "grow" in size and causes the total particle concentration to decrease. In addition, the total particle volume also decreases due to diffusion losses to the walls of the tube.

Particles are deposited onto a substrate in the third phase. There are three common deposition methods. A diffusion chamber lets particles randomly diffuse onto a surface, this creates a smooth coating used for instance for the development of microchips. Impaction, displayed in Figure 1.2, is a technique that accelerates a stream of particles through a nozzle, literally "impacting" on the substrate and making exact positioning of particles possible. Last, it is also possible to deposit particles of a certain size range by applying a filter with a corresponding mesh size.

1.2. RESEARCH GOAL AND APPROACH

VSPARTICLE aims for a highly efficient and fully controllable system generating nanoparticles of any desired quantity, particle size and shape. A computational model of the nanoparticle production process is required to develop a scientific understanding of the system, test the sensitivity of certain input parameters and eventually provide insights into how to operate the particle generator. It will contribute significantly to a completely controllable VSP-G1 system and the production of pure, tailor-made nanoparticles.

Mathematical and computational modelling are major concepts in this thesis. In general, modelling knows four main stages [16], the first consisting of three sub-stages:

1. The development of the model.
 - (a) Set physical framework.
 - (b) Define mathematical equations.
 - (c) Solve using numerical methods.
2. Validating the model with theory.
3. Validating the model with experimental results.
4. Putting the model to use.

This thesis conducts the first three stages and prospects on the fourth stage in the conclusion in Chapter 8.

DEVELOPMENT OF THE MODEL

First, it is necessary to define the system that going to be mathematically modelled. This thesis narrows its scope down to the nanoparticle growth occurring just after the spark until just before it enters the deposition chamber, leading to the underlying research goal:

Develop a numerical and computationally efficient model of the nanoparticle growth from spark ablation in the gas phase.

SET PHYSICAL FRAMEWORK

A framework for the model is constructed based on the physical properties of the system such as tube dimensions, ablation material, gas type and system settings for power and gasflow. It is impossible to compute the exact behaviour of hundreds of billions of nanoparticles. Therefore, underlying assumptions on the system and its environment are necessary. This thesis assumes nanoparticle growth occurs in a closed tube over a certain residence time t_R , from a certain starting concentration N_0 . The residence time corresponds to the time from when a particle is produced in phase one, until it reaches the end of the tube in phase two. The starting concentration is the amount of atoms in the aerosol produced in phase one. Particle growth is described exclusively by Brownian Motion and diffusion, while other, less prominent mechanisms are neglected.

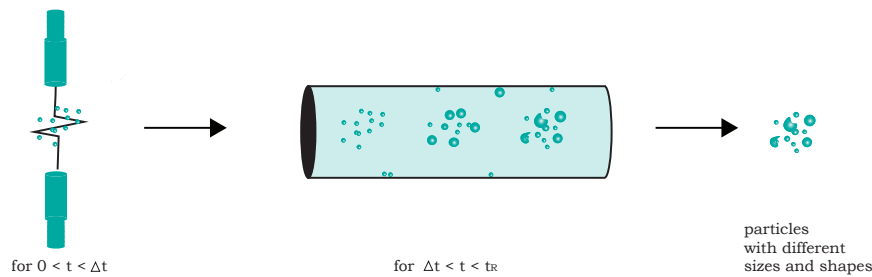


Figure 1.3: Framework of physical model for crossflow.

DEFINE MATHEMATICAL EQUATIONS

Mathematical equations that sufficiently describe the systems physical framework and particle growth mechanisms are chosen next. The Smoluchowski equation is applicable for simulating nanoparticle behaviour and is introduced in Chapter 2, along with approximation formulas for the residence time and initial particle concentration.

SOLVE USING NUMERICAL METHODS

Solving the original Smoluchowski equation to obtain the particle size distribution (PSD) results in a great deal of computation time. Therefore, the model itself is mathematically approximated using the Method of Moments (MoM) in Chapter 3. This method summarizes the statistics by deriving the mean, standard deviation and total particle concentration [16], providing the essential parameters to reconstruct the particle size distribution.

The MoM obtains a set of ordinary, non-linear differential equations (ODEs), forming an initial value problem (IVP). The solution is approached using numerical methods and computational power. Numerical methods divide continuous time into discrete intervals, and estimate the state of the system at the start of each interval [16]. The approximate solution changes through a series of steps and the numerical errors that accumulate are analyzed in Chapter 4.

VALIDATING THE MODEL WITH THEORY

Chapter 5 characterizes the qualitative behaviour of the model by analyzing the computed results in dimensionless form. Kyoong Won Lee is a prominent aerosol scientist who performed a great deal of research on (modelling) aerosol behaviour. His results, which are also in dimensionless form, are used to theoretically validate the model of nanoparticle growth in the VSP-G1. Population balance models, like the one in this study, obtain the qualitative feature that the long-term behaviour of the population is independent of the initial conditions [16]. This asymptotic behaviour is a key validation principle that the model must obtain.

VALIDATING THE MODEL WITH EXPERIMENTAL RESULTS

An important part of the modelling process is to validate the model with experimental data and thereby tailor it to VSPARTICLES needs. Various particle size distributions are measured from experiments conducted with the VSP-G1 under varying power P and flowrate Q settings. The corresponding values for P and Q are used in the approximation functions to derive initial conditions for the model. The model is experimentally validated when the computed particle size distributions comply with the measured, experimental results. The complete experimental model validation process and results are given in Chapter 6.

PUTTING THE MODEL TO USE

The experimental validation process shows that the model approximates the particle size at nanometer accuracy! Moreover, accuracy ranges are defined for the total concentration and geometric standard deviation of the PSD. These accuracy ranges can perform as benchmarks when interpreting results during future work. Furthermore, the model can be put to use for an input parameter sensitivity analysis and it also provides a better scientific understanding of the aerosol dynamics inside the system. Most importantly, it can function as a guide for operating the VSP-G1 to produce tailor-made nanoparticles.

2

MATHEMATICAL MODEL

A mathematical model is a description of a system using mathematical concepts. In this study, the system relates to physical nanoparticle growth in the VSP-G1 and the mathematical concept is defined by the Smoluchowski equation, given in Section 2.1. This governing equation is formulated to obtain two prominent particle growth mechanisms: coagulation and diffusion. The mathematical description of both terms is dependent on the environment and composition of the aerosol, which is treated in Sections 2.2 and 2.3. The governing equation of the mathematical model and corresponding initial conditions are formulated in Section 2.4. Finally, non-spherical particle growth is analyzed and mathematically approached in Section 2.5.

2.1. SMOLUCHOWSKI EQUATION

The evolution of aerosol particle behaviour originates from internal and external mechanisms, which are described by the Smoluchowski equation. Its original form only accounts for colloid coagulation [17]. A colloid is a mixture of microscopically dispersed particles which are incapable of being dissolved and suspended with another substance. Coagulation is an inter-particle mechanism which occurs when two particles collide and stick together to form a new, larger particle [3]. As coagulation takes place the mean particle size increases, the particle concentration decreases, while the total particle mass and volume stay constant. It is the most important nanoparticle growth mechanism to consider when simulating aerosol dynamics and the growth of particles in particular as it is the base of the Smoluchowski equation [3]:

$$\frac{\partial n(v, t)}{\partial t} = \frac{1}{2} \int_0^v \beta(v', v - v') n(v', t) n(v - v', t) dv' - n(v, t) \int_0^\infty \beta(v, v') n(v', t) dv' \quad (2.1)$$

Equation 2.1 is called a "population balance equation" and gives the rate of change of the particle size distribution in which v is the particle volume, t the time and n the particle size distribution [17]. The first term on the right hand side accounts for the formation of particles with volume v , by coagulation of smaller particles. The factor 1/2 avoids double counting collisions. The second term accounts for the loss of particles of volume v , by coagulation with others.

Coagulation is mainly driven by Brownian Motion of particles. In a homogeneous gas, Brownian Motion is the random motion of suspended particles due to their collisions with gas particles [3]. The number of collisions between particles of two different sizes is given by the collision frequency kernel $\beta(v, v')$.

Another mechanism is the continuous diffusion of aerosol particles to the surface (i.e. the wall of the transport tube), leading to a gradual decay in concentration [3]. Diffusion is modelled by adding a sink term to the Smoluchowski equation.

$$\frac{\partial n(v, t)}{\partial t} = \frac{1}{2} \int_0^v \beta(v', v - v') n(v', t) n(v - v', t) dv' - n(v, t) \int_0^\infty \beta(v, v') n(v', t) dv' + \frac{\partial n_{\text{sink}}(v, t)}{\partial t} \quad (2.2)$$

The model developed in the current research approximates a solution for Equation 2.2, which accounts for coagulation due to Brownian Motion and diffusion of nanoparticles in a closed space. The result is an approximation of the particle size distribution in the VSP-G1.

Note, the Smoluchowski equation can be extended to account for particle transport due to carrier gas flow by introducing a spacial coordinate x . Besides Brownian Motion, coagulation is also influenced by thermophoresis (the temperature rise of an aerosol) and inter-particle varying velocities. These concepts, along with most other aerosol mechanisms are incorporated in the extended Smoluchowski Equation given in Appendix A.1.

2.2. COAGULATION

Coagulating particles in a closed space are mathematically described by Equation 2.1 and the rate of coagulation is determined by the collision frequency kernel β .

The collision frequency kernel is dependent on the size-ratio between the ablated nanoparticles and the surrounding gas particles. It is necessary to introduce the gas mean free path λ and the Knudsen number Kn .

The gas mean free path is defined as the average distance travelled by a gas molecule between successive collisions [1]. The Knudsen number relates the gas mean free path to the particle diameter and determines in which "regime" particle motion takes place. Each regime consists of a unique expression for the collision frequency kernel β .

$$Kn = \frac{2\lambda}{d_p} \quad (2.3)$$

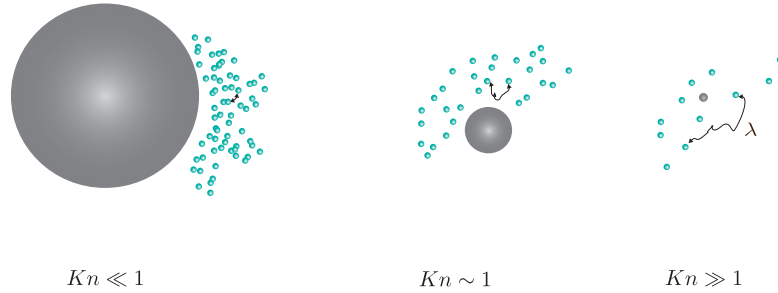


Figure 2.1: Particle dynamics in continuum, transition and free-molecular regime [2–4]. gas particle (grey), solid particles (green)

The gas mean free path is defined as:

$$\lambda = \frac{2\eta}{\sqrt{\frac{8RT}{\pi m_m}}}, \quad (2.4)$$

where R is the gas constant, T is the temperature, m_m is the molecular mass of the gas particle and η is the gas viscosity which is computed with the Sutherland constant, temperature and a reference-viscosity and temperature:

$$\eta = \eta_0 \left(\frac{T}{T_{ref}} \right)^{3/2} \frac{T_{ref} + Su}{T + Su}$$

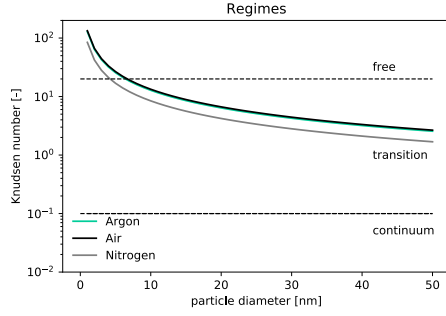


Figure 2.2: Knudsen number and regimes based on the particle diameter at room temperature

Previous studies ([1, 3, 4, 18]) have defined regimes based on the Knudsen number. Figure 2.2 visualizes these regimes for the particle size range and carrier gasses applicable for this research. The free molecular regime is considered for nanoparticles with diameters up to 5 nm. Particles exceeding this size enter the transition regime. Although the continuum regime is not considered initially, it is treated in this chapter as its properties are necessary for the definition of the collision kernel in the transition scheme (Section 2.2.3).

2.2.1. FREE MOLECULAR REGIME

In the free molecular regime, collisions take place by a ballistic process in which all particles can be treated as large molecules [3] (see Figure 2.1). The collision frequency kernel is defined as:

$$\beta_F(v, v') = K_F \left(\frac{3}{4\pi} \right)^{1/6} \left(\frac{1}{v} + \frac{1}{v'} \right)^{1/2} \left(v^{1/3} + v'^{1/3} \right)^2 \quad (2.5)$$

$$K_F = \left(\frac{6k_B T}{\rho_g} \right)^{1/2}, \quad (2.6)$$

where v and v' are particle volumes and k_B is the Boltzmann constant. Values for the coagulation constant K_F and gas density ρ_g under conditions applicable for this study are presented in Table 2.1.

2.2.2. CONTINUUM REGIME

Nanoparticles particles are in the continuum regime when their size is much larger than the mean free path ($\text{Kn} \ll 1$). Collisions are described by the collision frequency kernel for the continuum regime ¹:

$$\beta_C(v, v') = K_C \left(v^{1/3} + v'^{1/3} \right) \left(\frac{1}{v^{1/3}} + \frac{1}{v'^{1/3}} \right) \quad (2.7)$$

$$K_C = \frac{2k_B T}{3\eta}, \quad (2.8)$$

where η is the gas viscosity.

Non-continuum effects appear as the Knudsen number reaches its upper boundary: $\text{Kn} = 0.25$ [4], [18]. To account for these effects, the Cunningham Slip Correction factor $C(\text{Kn})$ is incorporated into Equation 2.7:

$$\beta_{Co}(v, v') = K_{Co} \left(v^{1/3} + v'^{1/3} \right) \left(\frac{C(\text{Kn})}{v^{1/3}} + \frac{C(\text{Kn}')}{v'^{1/3}} \right), \quad (2.9)$$

$$C(\text{Kn}) = 1 + \text{Kn} \left(\alpha + \beta \exp(-\gamma/\text{Kn}) \right) \quad (2.10)$$

where $K_{Co} = K_C$ and parameters α , β and γ are adjusted to best fit the carrier gas and corresponding regime. The following values hold in the transition regime for argon gas [7] ²:

$$\begin{cases} \alpha &= 1.227 \\ \beta &= 0.42 \\ \gamma &= 0 \end{cases} \quad (2.11)$$

¹For the current research, β_C is only necessary for the definition of the collision frequency kernel of the transition regime (Equation 2.13).

²Rader conducted research on the Slip Correction Factor for small particles in nine common gasses [4] and found different values for the parameters in 2.11, these are tabulated for various gasses in Appendix A.2

Table 2.1 lists the densities, viscosity's and corresponding coagulation constants for different gas types and regimes under standard conditions³.

Gas	ρ_g [kg/m ³]	K_F [m ^{5/2} /s]	μ [kg/ms]	K_C [m ³ /s]
Argon gas	1.645	1.221×10^{-10}	2.52×10^{-5}	1.820×10^{-16}
Air	1.192	1.435×10^{-10}	1.83×10^{-5}	2.239×10^{-16}
Nitrogen gas	1.165	1.451×10^{-10}	1.74×10^{-5}	2.328×10^{-16}

Table 2.1: coagulation constants for carrier gasses applicable for the VSP-G1 under standard conditions³

2.2.3. TRANSITION REGIME

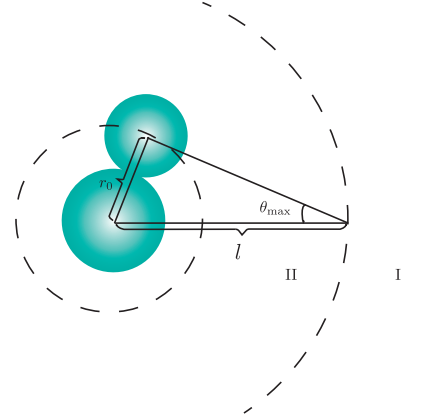
For particles with a diameter that is approximately the same as the gas mean free path ($d_p \approx \lambda$), coagulation occurs in the transition regime. Fuchs developed the flux matching method to combine the free molecular kernel β_F and continuum kernel β_{Co} to obtain the transition kernel [9].

The method assumes that outside a distance l , from the center of one of the colliding particles, the diffusion theory is considered and fluxes are described as they are in the continuum regime, (area I in Figure 2.3). Within distance l , particle fluxes are approached by the kinetic gas theory [19], (area II). Fluxes are matched at the distance l . The location of the boundary varies per method. The present research investigates the most basic method: the harmonic mean, and Dahneke (1983)'s method, which is also known for its accuracy and simplicity [9].

The harmonic mean matches the fluxes at the collision sphere [9], which is the distance between the centers of two particles at the moment of collision ($r_1 + r_2$). The collision frequency kernel following the harmonic mean method is equal to [19]:

$$\beta_H = \left(\frac{1}{\beta_{Co}(v, v')} + \frac{1}{\beta_F(v, v')} \right)^{-1} \quad (2.12)$$

Figure 2.3: Geometry of the collision model in the flux matching method [5]



Dahneke describes diffusion as a mean free path phenomenon [9] and matches the two fluxes at a distance equal to the mean free path of the particles. Various researchers prefer Dahneke's kernel β_D because of its accuracy relative to the harmonic mean, but also for its simplicity with respect to other methods found by Fuchs and Wright [18], [9], [19].

Dahneke's transition kernel allows the mathematically approximated particle environment to gradually shift from one regime to the other with increasing particle size. It is therefore applicable for the entire particle regime.

$$\beta_D = \beta_{Co} \frac{1 + Kn_D}{1 + 2Kn_D + 2Kn_D^2}, \quad (2.13)$$

$$Kn_D = \frac{\beta_{Co}(v, v')}{2\beta_F(v, v')}$$

³ $T_0 = 296.15$ K; $P_0 = 101.325$ kPa

2.3. DIFFUSION

Besides taking coagulation into account, Equation 2.2 also describes the affect of diffusion on the particle concentration. According to [8] the decay in particle concentration due to diffusion to the tube wall for a monodisperse aerosol in a circular tube is:

$$\frac{n}{n_0} = \exp\left(-\frac{4.117Dz}{R_t^2 \bar{u}}\right), \quad (2.14)$$

$$D(r) = \frac{k_B T}{6\pi\eta r} C(\text{Kn}), \quad (2.15)$$

where n_0 is the initial particle concentration, z is the position in the tube, R_t the tube radius, \bar{u} the mean transport velocity of the aerosol through the tube, D the diffusion coefficient of particles depositing on the wall, r is the particle radius, k_B the Boltzmann constant, η the gas viscosity, and $C(\text{Kn})$ the Cunningham Coefficient.

This study requires Equation 2.14 to fit the time- and volume dependent format: $\frac{\partial n_{\text{sink}}(v,t)}{\partial t}$. Therefore, the spacial coordinate z is converted to time with Equation 2.16, and the diffusion- and Cunningham coefficients are written in terms of v and K_{Co} . (Recall: $K_{Co} = \frac{2k_B T}{3\eta}$)

$$t = \frac{z}{\bar{u}} \quad (2.16)$$

$$D(v) = \frac{K_{Co}}{4\sqrt[3]{\frac{3}{4\pi}}\pi v^{1/3}} C(v) \quad (2.17)$$

$$C(v) = 1 + \frac{\lambda}{\sqrt[3]{\frac{3}{4\pi}}} v^{-\frac{1}{3}} \left(\alpha + \beta \exp\left(-\frac{\gamma}{\lambda} \sqrt[3]{\frac{3}{4\pi}} v^{\frac{1}{3}}\right) \right) \quad (2.18)$$

Differentiating (2.14) over time, and inserting Equation 2.17 yields an expression for the sink term that obtains a sufficient format to include in the original Smoluchowski equation:

$$\frac{\partial n_{\text{sink}}(v)}{\partial t} = -\frac{1.67}{R_t^2 \pi v^{1/3}} K_{Co} C(v) n(v, t) \quad (2.19)$$

2.4. MATHEMATICAL MODEL

The aim of this research is to solve the Smoluchowski equation using Dahneke's transition kernel (Equation ??) and diffusion effects formulated by the sink term in Equation 2.19:

$$\begin{aligned} \frac{\partial n(v, t)}{\partial t} = & \frac{1}{2} \int_0^v \beta_D(v', v-v') n(v', t) n(v-v', t) dv' - \\ & n(v, t) \int_0^\infty \beta_D(v, v') n(v', t) dv' - \frac{1.67}{R_t^2 \pi} K_{Co} C(v) n(v, t) \end{aligned} \quad (2.20)$$

Now that all terms are treated, Equation 2.20 is defined as the governing equation for the mathematical model. This function simulates an initial particle concentration N_0 that is exposed to coagulation and diffusion effects in a closed space over a residence time t_R .

RESIDENCE TIME

The residence time is the total time that a particle spends inside VSP-G1:

$$\begin{aligned} t_R = & \frac{V_{\text{chamber}}}{Q} + \frac{V_{\text{tube}}}{Q}, \quad (2.21) \\ V_{\text{tube}} = & \pi R_t^2 L \\ V_{\text{chamber}} = & \begin{cases} 52 \text{ cm}^3 & \text{cross flow} \\ 10 \text{ cm}^3 & \text{through flow} \\ 0.9 \text{ m}^3 & \text{insert} \end{cases} \end{aligned}$$

where R_t is the radius of the tube, L is the length of the tube and Q is the flow rate of the gas. The volume of the reactor chamber is defined per flowtype.

INITIAL CONCENTRATION

It is assumed that spark ablation initially creates an aerosol of pure, single atoms and the corresponding concentration is noted with N_0 . The initial concentration is determined by the spark frequency and intensity, the material of the electrodes, and the flowrate of the gas. The corresponding approximation function yields⁴:

$$N_0 = \frac{m_A N_A I V}{Q}, \quad (2.22)$$

where m_A [mol/J] is the material dependent ablation rate and is determined either from theory or experimental mass measurements (See Section 6.2). N_A is Avogadro's constant which defines the amount of atoms per mol. Finally, I is the current in mA (expressing spark frequency), V is the voltage in kV (representing spark intensity) and their product forms the power of the VSP-G1: $P = IV$.

Note, the approximation function suggests a linear relation between the ablation rate and the power. This assumption is met through an analysis given in Section 6.2.

2.5. AGGLOMERATES

If two solid particles collide, the result may be an agglomerate or a spherical particle, depending on the relative rates of fusion and collision. An agglomerate is a particle formed by two or more smaller particles which have not fully fused into a sphere [3]. The mechanism that causes two particles to fuse is called sintering. The rate of sintering is a strong function of temperature, particle size and material properties [3].

The characteristic collision time defines the importance of coagulation on aerosol dynamics and is equal to the time it takes for particles to reduce to a concentration which is half its initial value [3].

When the characteristic time for sintering t_S is greater than the characteristic collision time t_C , an agglomerate forms instead of a spherical particle.

$$t_C \approx \left(\left(\frac{3v}{4\pi} \right)^{1/6} K_F N_0^{5/6} \right)^{-1} \quad (2.23)$$

$$t_S = A d_p^4 \exp\left(\frac{E}{RT}\right) \quad (2.24)$$

where v is the total particle volume, N_0 the initial particle concentration and K_F is the coagulation constant in the free molecular regime as defined in Equation 2.6, E is the activation energy for diffusion, R is the gas constant and A is a constant.

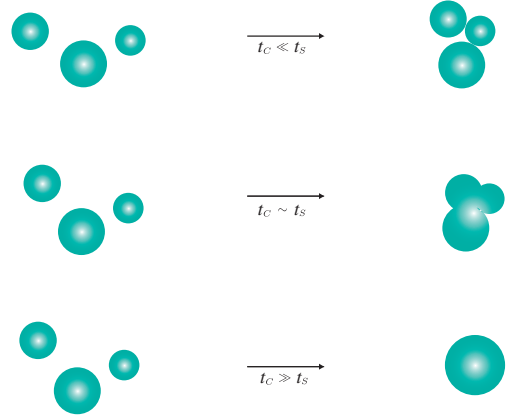


Figure 2.4: Particle morphologies v.s. collision rate [3]

⁴The approximation formula for N_0 is derived in collaboration with VSPARTICLE.

The transport properties of agglomerates are substantially different from spherical primary particle properties. The *mass fractal dimension*, D_F defines the irregular structure of the agglomerates in terms of its "openness" [3]. Typically D_F varies from 1 to 3. $D_F = 3$ defines a solid sphere, while $D_F = 1$ corresponds with primary particles stuck together in a single line. According to previous research [15], the VSP-G1 creates agglomerates with a fractal dimension between $1.7 < D_F < 2.2$.

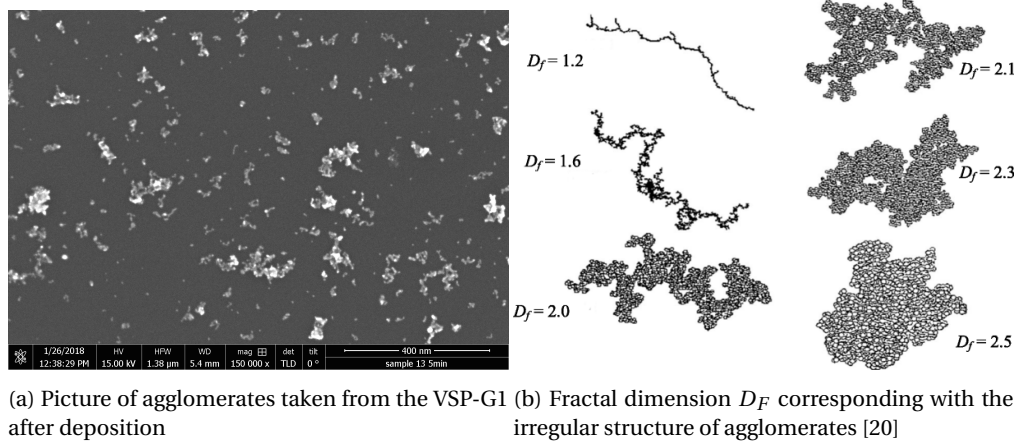


Figure 2.5: Agglomerate structures

IMPLEMENTATION IN MODEL

Agglomeration can be incorporated into the model when $t_c < t_s$. The empirical relation between the agglomerate diameter d_{ag} and corresponding singlet diameter d_s according to [21] is:

$$\frac{d_{ag}}{d_s} = \frac{d_{cl}^{3/D_F}}{d_s} \quad (2.25)$$

This is rewritten to formulate transfer functions between the agglomerate diameter and the close packed diameter d_{cl} , which is the diameter of a spherical particle of the equivalent mass as the corresponding agglomerate.

$$d_{ag} = d_s^{(1-F)} d_{cl}^F \quad (2.26)$$

$$d_{cl} = \left(\frac{d_{ag}}{d_s^{1-F}} \right)^{1/F} \quad (2.27)$$

where F is a function of agglomerate radius d_{ag} :

$$\begin{aligned} F &= (3/D_F - 1)(1 - e^{-2(d_{ag} - d_s)}) + 1 && \text{for } d_{ag} > d_s \\ F &= 1 && \text{for } d_{ag} < d_s, \end{aligned}$$

where $D_F = 2.18$ holds for conditions applicable for the VSP-G1.

Note, the transfer functions may be applied to the output of the model to incorporate agglomerates, but can also be used on experimental measurements. For example, measurement instruments characterize particle sizes based on their agglomerate diameter. With Equation 2.27 these empirical results are easily converted to formulate an equivalent output format as that of the model for validation purposes.

3

METHOD OF MOMENTS

The mathematical model of nanoparticle growth in the VSP-G1 is based on the Smoluchowski Equation using Dahneke's kernel.

$$\frac{\partial n(v, t)}{\partial t} = \frac{1}{2} \int_0^v \beta_D(v', v - v') n(v', t) n(v - v', t) dv' - n(v, t) \int_0^\infty \beta_D(v, v') n(v', t) dv' + \frac{\partial n_{\text{sink}}(v, t)}{\partial t} \quad (3.1)$$

The framework of the model and mathematical equations are described in Chapter 2, where the particle size distribution $n(v, t)$ is obtained after a certain residence time t_R . This chapter studies the solution method obtained by Pafnuty Chebyshev in 1887 to solve for $n(v, t)$. The Method of Moments (MoM) assumes particle volume conservation, and is therefore applicable for models approximating particle growth in a closed spaces.

The MoM has been applied in a wide range of fields such as electromagnetism [22], planetary formation [23], finances, data processing [24], but also aerosol dynamics and nanotechnology [6, 7, 17, 25–28]. Frenklach and Harris used the MoM in 1987 to simulate nanoparticle growth mechanisms like nucleation, surface reaction and coagulation [28]. Without having to track the behavior of the entire particle size distribution (PSD), the MoM extracts specific information from the Smoluchowski equation, so called "moments". The zeroth moment is equal to the total particle concentration $M_0(t) = N(t)$, the first moment resembles the total particle volume and the second moment is the total particle volume squared.

The result is a set of ordinary differential equations (ODEs) for the first three moments. Assuming a log-normal distribution provides the correct initial conditions and format to solve the set of ODEs. Nondimensionalization of the problem is required due to stiffness issues. Finally, the solution in terms of moments provides information that enables the reconstruction of the PSD.

3.1. MOMENT GOVERNING EQUATION

The first task of the MoM is to convert the original Smoluchowski equation into a momentum equation based on the size distribution [17]: the moment governing equation. The derivation of the moment governing equation of the present study is conducted according to [23]. However, to the best of our knowledge, including Dahneke's kernel *and* diffusion into the governing equation is new in this field of research.

The method of moments uses the fact that the k -th moment of the distribution, M^k , where k need not be an integer is defined as:

$$M_k(t) = \int_0^\infty v^k n(v, t) dv \quad (3.2)$$

Five steps lead to the moment governing equation.

STEP 1

Both sides of the equation 3.1 are multiplied by v^k and integrated over volume v . Also, Expression 3.2 is applied to the LHS.

$$\begin{aligned} \frac{dM_k}{dt} = \int_0^\infty v^k \frac{dn(v, t)}{dt} dv = \frac{1}{2} \int_0^\infty \int_0^v v^k \beta_D(v', v-v') n(v-v', t) n(v', t) dv' dv \\ - \int_0^\infty \int_0^\infty v^k \beta_D(v, v') n(v, t) n(v', t) dv' dv + \int_0^\infty v^k \frac{dn_{\text{sink}}(v, t)}{dt} dv \end{aligned} \quad (3.3)$$

STEP 2

A Heaviside function, $H(v-v')$, is introduced such that:

$$H(v-v') = \begin{cases} 1 & v-v' \geq 0 \\ 0 & v-v' < 0, \end{cases}$$

to extend the limits of the integral over v' from $(0, v)$ to $(0, \infty)$.

$$\begin{aligned} \frac{dM_k}{dt} = \frac{1}{2} \int_0^\infty \int_0^v v^k H(v-v') \beta_D(v', v-v') n(v-v', t) n(v', t) dv' dv \\ - \int_0^\infty \int_0^\infty v^k \beta_D(v, v') n(v, t) n(v', t) dv' dv + \int_0^\infty v^k \frac{dn_{\text{sink}}(v, t)}{dt} dv \end{aligned} \quad (3.4)$$

STEP 3

$u = v-v'$, $du = dv$ and $v^k = (u+v')^k$ are substituted into Equation 3.4. As the first integral is integrated over purely positive values for u , the Heaviside function is always equal to one.

$$\begin{aligned} \frac{dM_k}{dt} = \frac{1}{2} \int_0^\infty \int_0^\infty (u+v')^k \beta_D(u, v') n(u, t) n(v', t) dv' du \\ - \int_0^\infty \int_0^\infty v^k \beta_D(v, v') n(v, t) n(v', t) dv' dv + \int_0^\infty v^k \frac{dn_{\text{sink}}(v, t)}{dt} dv \end{aligned} \quad (3.5)$$

STEP 4

Without loss of generality, v is substituted for u , allowing the two integrals of the population balance equation to merge.

$$\frac{dM_k}{dt} = \int_0^\infty \int_0^\infty \left[\frac{1}{2} (v+v')^k - v^k \right] \beta_D(v, v') n(v, t) n(v', t) dv dv' + \int_0^\infty v^k \frac{dn_{\text{sink}}(v, t)}{dt} dv \quad (3.6)$$

STEP 5

Due to symmetry the equation above also holds for $v^k = v'^k$, and the expression for the moment governing equation is obtained.

$$\frac{dM_k}{dt} = \frac{1}{2} \int_0^\infty \int_0^\infty \left[(v+v')^k - v^k - v'^k \right] \beta_D(v, v') n(v, t) n(v', t) dv dv' + \int_0^\infty v^k \frac{dn_{\text{sink}}(v, t)}{dt} dv \quad (3.7)$$

Now the key is to convert the integral term on the RHS of Equation 3.7 to a set of closed ordinary differential equations for the zeroth-, first- and second moment.

3.2. DERIVATION OF ODES USING LOG-NORMAL MOM

Given the moment Equation 3.7 and Dahnekes kernel:

$$\begin{aligned}\beta_D &= \beta_{Co}(v, v') \frac{1 + Kn_D}{1 + 2Kn_D + 2Kn_D^2} \\ Kn_D &= \frac{\beta_{Co}(v, v')}{2\beta_F(v, v')} \\ \beta_{Co}(v, v') &= K_{Co} \left(v^{1/3} + v'^{1/3} \right) \left(\frac{C(v)}{v^{1/3}} + \frac{C(v')}{v'^{1/3}} \right) \\ \beta_F(v, v') &= K_F \left(\frac{3}{4\pi} \right)^{1/6} \left(\frac{1}{v} + \frac{1}{v'} \right)^{1/2} \left(v^{1/3} + v'^{1/3} \right)^2\end{aligned}$$

Due to non linearity (unlike for the free molecular and continuum kernels), it is not possible to integrate Dahnekes kernel directly using Expression 3.2. Therefore the solution is approached in the limiting regimes first, and are subsequently used to obtain an expression for the entire regime in terms of moments [9]. In addition, a separate moment function is defined for the sink term. The result is an ordinary differential equation for any k^{th} moment:

$$\begin{aligned}\frac{dM_k}{dt} &= \underbrace{\frac{dM_k}{dt} \Big|_{Co} \left(\frac{1 + Kn_{D,k}}{1 + a(\sigma)Kn_{D,k} + 2Kn_{D,k}^2} \right)}_{\frac{dM_k}{dt} \Big|_D} + \frac{dM_k}{dt} \Big|_{\text{sink}} \quad (3.8) \\ Kn_{D,k} &= \frac{1}{2} \left(\frac{dM_k}{dt} \Big|_{Co} \right) \left(\frac{dM_k}{dt} \Big|_F \right)^{-1} \\ a(\sigma) &= 2 + 0.7 \ln^2(\sigma) + 0.85 \ln^3(\sigma)\end{aligned}$$

Here $a(\sigma)$ is a correction function compensating for mathematical errors due to an increasing standard deviation [9].

In this section the log-normal method of moments is used to express each term in Equation 3.8 in terms of dimensionless moment functions. Starting with the limiting regimes $\frac{dM_k}{dt} \Big|_F$ and $\frac{dM_k}{dt} \Big|_{Co}$ to formulate Dahneke's transition kernel $\frac{dM_k}{dt} \Big|_D$. Finally, also the sink term $\frac{dM_k}{dt} \Big|_{\text{sink}}$ is expressed in terms of dimensionless moments.

3.2.1. LOG-NORMAL METHOD OF MOMENTS

The log-normal particle size distribution is defined as

$$n(v, t) = \frac{1}{3v} \frac{N(t)}{\sqrt{2\pi \ln \sigma(t)}} \exp \left[\frac{-\ln^2 v / v_g(t)}{18 \ln^2 \sigma(t)} \right], \quad (3.9)$$

where $N(t)$ is the total particle concentration at time t , $v_g(t)$ the geometric mean particle size, v the particle size and $\sigma(t)$ the geometric standard deviation [6, 7, 9].

The k^{th} moment of a log-normal size distribution is defined as [6, 7, 9]:

$$M_k = \frac{1}{3\sqrt{2\pi \ln \sigma(t)}} \int_0^\infty v^k \exp \left[\frac{-\ln^2 v / v_g(t)}{18 \ln^2 \sigma(t)} \right] \frac{dv}{v}, \quad (3.10)$$

and the properties of a log-normal function allow the following equation to hold for any k^{th} moment [6, 7]:

$$M_k = M_0 v_g^k \exp \left(\frac{9}{2} k^2 \ln^2(\sigma) \right), \quad (3.11)$$

Besides obtaining the total particle concentration from the zeroth moment $M_0 = N$, expressions for ν_g and σ are also necessary to compute the particle size distribution: Expression 3.9. These are obtained by writing Equation 3.11 for $k = 0, k = 1, k = 2$ and rearranging it in terms of ν_g and σ :

$$\nu_g = \frac{M_1^2}{M_0^{3/2} M_2^{1/2}} \quad (3.12)$$

$$\ln^2 \sigma = \frac{1}{9} \ln \left[\frac{M_0 M_2}{M_1^2} \right] \quad (3.13)$$

Equations 3.11 - 3.13 operate as tools to solve the ordinary differential equations in the limiting regimes first, and are later used in Equation 3.9 to express the particle size distribution.

3.2.2. FREE MOLECULAR REGIME

A set of ODEs is derived for both limiting regimes, starting with the free molecular regime. This corresponds to the following function when neglecting diffusion effects:

$$\left. \frac{dM_k}{dt} \right|_F = \frac{1}{2} \int_0^\infty \int_0^\infty \left[(v + v')^k - v^k - v'^k \right] \beta_F(v, v') n(v, t) n(v', t) dv dv' \quad (3.14)$$

In the free-molecular regime, it is difficult to expand the kernel β_F (Equation 2.5) into a power series [29]. Therefore, a coefficient b is introduced such that: $\sqrt{\frac{1}{v} + \frac{1}{v'}} = b \left(\sqrt{\frac{1}{v}} + \sqrt{\frac{1}{v'}} \right)$. The coefficient b is dependent on the polydispersity of the aerosol [7], which is represented by the geometric spread of the particle size distribution σ . The function b is fitted to only depend on σ by Park, Lee, Otto and Fissan in [7]:

$$b(\sigma) = 1 + 1.2 \exp(-2\sigma) - 0.646 \exp(-0.35\sigma^2) \quad (3.15)$$

The collision frequency kernel for the free-molecular regime is written as:

$$\beta_F(v, v') = b(\sigma) K_F \left(\frac{3}{4\pi} \right)^{1/6} \left(\sqrt{\frac{1}{v}} + \sqrt{\frac{1}{v'}} \right) (v^{1/3} + v'^{1/3})^2 \quad (3.16)$$

Inserting the new expression for β_F into the moment governing equation yields:

$$\begin{aligned} \left. \frac{dM_k}{dt} \right|_F &= \frac{b K_F}{2} \left(\frac{3}{4\pi} \right)^{1/6} \int_0^\infty \int_0^\infty \left[(v + v')^k - v^k - v'^k \right] \left(\sqrt{\frac{1}{v}} + \sqrt{\frac{1}{v'}} \right) (v^{1/3} + v'^{1/3})^2 n(v, t) n(v', t) dv dv' \\ &= \frac{b K_F}{2} \left(\frac{3}{4\pi} \right)^{1/6} \int_0^\infty \int_0^\infty \left[(v + v')^k - v^k - v'^k \right] \left(v^{1/6} v'^{1/6} \frac{2v^{1/3}}{v'^{1/6}} + \frac{2v'^{1/3}}{v^{1/6}} + \frac{v'^{2/3}}{v^{1/2}} + \frac{v^{2/3}}{v'^{1/2}} \right) n(v, t) n(v', t) dv dv' \end{aligned} \quad (3.17)$$

The current research is interested in the first three moments. Letting $k = 0, k = 1$ and $k = 2$ and using the expression for any k^{th} moment in Equation 3.11 formulates a set of unclosed ODEs.

$$\begin{cases} \left. \frac{dM_0}{dt} \right|_F = -b K_F \left(\frac{3}{4\pi} \right)^{1/6} (M_{1/6} M_0 + 2 M_{1/3} M_{-1/6} + M_{2/3} M_{-1/2}) \\ \left. \frac{dM_1}{dt} \right|_F = 0 \\ \left. \frac{dM_2}{dt} \right|_F = 2b K_F \left(\frac{3}{4\pi} \right)^{1/6} (M_{7/6} M_1 + 2 M_{4/3} M_{5/6} + M_{1/2} M_{5/3}) \end{cases} \quad (3.18)$$

Substituting Equations 3.11 - 3.13 closes the set of ODE's:

$$\begin{cases} \left. \frac{dM_0}{dt} \right|_F = -b \tilde{K}_F (M_0^{151/72} M_1^{-13/36} M_2^{19/72} + 2 M_0^{131/72} M_1^{7/36} M_2^{-1/72} + M_0^{127/72} M_1^{11/36} M_2^{-5/72}) \\ \left. \frac{dM_1}{dt} \right|_F = 0 \\ \left. \frac{dM_2}{dt} \right|_F = 2b \tilde{K}_F (M_0^{19/72} M_1^{-97/36} M_2^{31/72} + 2 M_0^{-1/72} M_1^{-77/36} M_2^{11/72} + M_0^{-5/72} M_1^{-73/36} M_2^{7/72}) \end{cases}, \quad (3.19)$$

where the collision constant is redefined to maintain clear notations: $\tilde{K}_F = \left(\frac{3}{4\pi} \right)^{1/6} \left(\frac{6k_B T}{\rho_g} \right)^{1/2}$.

NONDIMENSIONALIZATION

The set of ODE's is too stiff to solve. Therefore dimensionless moments \widetilde{M}_k and dimensionless time τ are introduced such that the following holds [6]:

$$M_k = \widetilde{M}_k N_0 v_{g0}^k \exp\left(\frac{9}{2} k^2 \ln^2 \sigma_0\right) \quad (3.20)$$

$$t = \tau (v_{g0}^{1/6} \widetilde{K}_F N_0)^{-1} \quad (3.21)$$

$$b(\sigma(t)) = B(\tau) \quad (3.22)$$

Substituting equations 3.20 - 3.22 into 3.19 results in the set of ordinary differential equations for the moments functions in the limiting molecular free regime.

$$\begin{aligned} \frac{d\widetilde{M}_0}{d\tau_F} \Big|_F &= -B(\tau_F) u \left(\widetilde{M}_0^{\frac{151}{72}} \widetilde{M}_1^{\frac{-13}{36}} \widetilde{M}_2^{\frac{19}{72}} \exp\left(\frac{25}{8} \ln^2 \sigma_0\right) \dots \right. \\ &\quad \dots + 2\widetilde{M}_0^{\frac{131}{72}} \widetilde{M}_1^{\frac{7}{36}} \widetilde{M}_2^{\frac{-1}{72}} \exp\left(\frac{5}{8} \ln^2 \sigma_0\right) \dots \\ &\quad \left. \dots + \widetilde{M}_0^{\frac{127}{72}} \widetilde{M}_1^{\frac{11}{36}} \widetilde{M}_2^{\frac{-5}{72}} \exp\left(\frac{1}{8} \ln^2 \sigma_0\right) \right) \\ &\equiv B(\tau_F) \widetilde{g}_0 \end{aligned} \quad (3.23)$$

$$\begin{aligned} \frac{d\widetilde{M}_1}{d\tau_F} \Big|_F &= 0 \\ &\equiv \widetilde{g}_1 \end{aligned} \quad (3.24)$$

$$\begin{aligned} \frac{d\widetilde{M}_2}{d\tau} \Big|_F &= 2B(\tau_F) \left(\widetilde{M}_0^{\frac{19}{72}} \widetilde{M}_1^{\frac{47}{36}} \widetilde{M}_2^{\frac{31}{72}} \exp\left(\frac{109}{8} \ln^2 \sigma_0\right) \dots \right. \\ &\quad \dots + 2\widetilde{M}_0^{\frac{-7}{72}} \widetilde{M}_1^{\frac{67}{36}} \widetilde{M}_2^{\frac{11}{72}} \exp\left(\frac{89}{8} \ln^2 \sigma_0\right) \dots \\ &\quad \left. \dots + \widetilde{M}_0^{\frac{-5}{72}} \widetilde{M}_1^{\frac{71}{36}} \widetilde{M}_2^{\frac{7}{72}} \exp\left(\frac{85}{8} \ln^2 \sigma_0\right) \right) / \exp(18 \ln^2 \sigma_0) \\ &\equiv B(\tau_F) \widetilde{g}_2 \end{aligned} \quad (3.25)$$

To maintain clear and understandable notations, the RHSs of Equations 3.23- 3.25 are noted in terms of \widetilde{g}_k and $B(\tau_F)$ for the remainder of this thesis.

3.2.3. CONTINUUM REGIME

Along the same route, a set of closed ordinary differential equations for the the first three moments in the continuum regime is derived from:

$$\frac{dM_k}{dt} \Big|_{Co} = \frac{1}{2} \int_0^\infty \int_0^\infty \left[(v+v')^k - v^k - v'^k \right] \beta_{Co}(v, v') n(v, t) n(v', t) dv dv' \quad (3.26)$$

From [2], for $Kn \ll 1$, the fractal set of ODEs is defined as:

$$\begin{cases} \frac{dM_0}{dt} \Big|_{Co} = -K_{Co} \left[M_0^2 + M_{1/3} M_{-1/3} + A\lambda \left(\frac{4}{3}\pi\right)^{1/3} (M_0 M_{-1/3} + M_{1/3} M_{-2/3}) \right] \\ \frac{dM_1}{dt} \Big|_{Co} = 0 \\ \frac{dM_2}{dt} \Big|_{Co} = 2K_{Co} \left[M_1^2 + M_{4/3} M_{2/3} + A\lambda \left(\frac{4}{3}\pi\right)^{1/3} (M_1 M_{2/3} + M_{4/3} M_{1/3}) \right] \end{cases} \quad (3.27)$$

Where:

$$\begin{aligned} K_{Co} &= \frac{2k_B T}{2\eta} \quad [\text{m}^3 \text{s}^{-1}] \\ A &= 1.591 \\ \lambda &= \text{gas mean free path} \end{aligned}$$

By applying Equations 3.11 - 3.13, a set of closed ODEs is derived in terms of M_0 , M_1 and M_2 .

$$\begin{cases} \left. \frac{dM_0}{dt} \right|_{Co} = -K_{Co} \left[M_0^2 + M_0^{19/9} M_1^{-2/9} M_2^{1/9} + A\lambda \left(\frac{4}{3}\pi \right)^{1/3} (M_0^{23/9} M_1^{-7/9} M_2^{2/9} + M_0^{25/9} M_1^{-11/9} M_2^{4/9}) \right] \\ \left. \frac{dM_1}{dt} \right|_{Co} = 0 \\ \left. \frac{dM_2}{dt} \right|_{Co} = 2K_{Co} \left[M_1^2 + M_0^{1/9} M_1^{16/9} M_2^{1/9} + A\lambda \left(\frac{4}{3}\pi \right)^{1/3} (M_0^{2/9} M_1^{17/9} M_2^{-1/9} + M_0^{4/9} M_1^{13/9} M_2^{1/9}) \right] \end{cases} \quad (3.28)$$

Using the dimensionless parameters from [9]:

$$\begin{aligned} M_k &= \widetilde{M}_k N_0 v_{g0}^k \exp\left(\frac{9}{2} k^2 \ln^2 \sigma_0\right) \\ t &= \tau_{Co} (N_0 K_{Co})^{-1} \end{aligned} \quad (3.29)$$

$$A = \tilde{A} \lambda^{-1} \left(-\frac{4}{3}\pi \right)^{1/3} \sqrt[3]{v_{g0}}, \quad (3.30)$$

the set of ODEs is nondimensionalized:

$$\begin{aligned} \left. \frac{d\widetilde{M}_0}{d\tau} \right|_{Co} &= - \left(\widetilde{M}_0^2 + \widetilde{M}_0^{19/9} \widetilde{M}_1^{-2/9} \widetilde{M}_2^{1/9} \exp(\ln^2 \sigma_0) \dots \right. \\ &\quad \left. \dots + \tilde{A} \left(\widetilde{M}_0^{23/9} \widetilde{M}_1^{-7/9} \widetilde{M}_2^{2/9} \exp\left(\frac{1}{2} \ln^2 \sigma_0\right) + \widetilde{M}_0^{25/9} \widetilde{M}_1^{-11/9} \widetilde{M}_2^{4/9} \exp\left(\frac{5}{2} \ln^2 \sigma_0\right) \right) \right) \\ &\equiv \tilde{h}_0 \end{aligned} \quad (3.31)$$

$$\begin{aligned} \left. \frac{d\widetilde{M}_1}{d\tau} \right|_{Co} &= 0 \\ &\equiv \tilde{h}_1 \end{aligned} \quad (3.32)$$

$$\begin{aligned} \left. \frac{d\widetilde{M}_2}{d\tau} \right|_{Co} &= 2 \left(\exp(9 \ln^2 \sigma_0) + \widetilde{M}_0^{1/9} \widetilde{M}_1^{16/9} \widetilde{M}_2^{1/9} \exp(10 \ln^2 \sigma_0) \dots \right. \\ &\quad \left. \dots + \tilde{A} \left(\widetilde{M}_0^{2/9} \widetilde{M}_1^{13/9} \widetilde{M}_2^{-1/9} \exp\left(\frac{13}{2} \ln^2 \sigma_0\right) + \widetilde{M}_0^{4/9} \widetilde{M}_1^{13/9} \widetilde{M}_2^{1/9} \exp\left(\frac{17}{2} \ln^2 \sigma_0\right) \right) \right) / \exp(18 \ln^2 \sigma_0) \\ &\equiv \tilde{h}_2 \end{aligned} \quad (3.33)$$

To maintain clear and understandable notations, the RHSs of Equations 3.31- 3.33 are noted in terms of \tilde{h}_k for the remainder of this thesis.

3.2.4. TRANSITION REGIME

Now that the differential moment equations in the limiting regimes $\left. \frac{d\widetilde{M}_k}{d\tau} \right|_{Co}$ and $\left. \frac{d\widetilde{M}_k}{d\tau} \right|_F$ are defined, it is possible to combine them using Dahneke's method to formulate an expression for the entire regime. Equation 3.8 (sink term excluded) is defined as:

$$\left. \frac{d\widetilde{M}_k}{d\tau} \right|_D = \left. \frac{d\widetilde{M}_k}{d\tau} \right|_{Co} \frac{1 + \frac{d\widetilde{M}_k/d\tau_{Co}}{2d\widetilde{M}_k/d\tau_F}}{1 + a(\sigma) \frac{d\widetilde{M}_k/d\tau_{Co}}{2d\widetilde{M}_k/d\tau_F} + 2 \left(\frac{d\widetilde{M}_k/d\tau_{Co}}{2d\widetilde{M}_k/d\tau_F} \right)^2} \quad (3.34)$$

The transition kernel contains two dimensionless expressions for time. However under the same conditions, both obtain the same value for t when converted back to dimensional time. Therefore, the timestep applicable for the free molecular regime can be expressed in terms of the timestep for the continuum regime:

$$d\tau_F = \frac{d\tau_{Co} v_{g0}^{1/6} K_F}{K_{Co}} \quad (3.35)$$

Recall the notation for the dimensionless moment differential equations in the free molecular regime $B(\tau_F) \tilde{g}_k$. Using Equation 3.35 it is possible to express $\left. \frac{d\widetilde{M}_k}{d\tau_F} \right|_F$ in terms of τ_{Co} . Note that [29] states

$B(\tau_F) \approx B(\tau_{Co})$ which is validated by calculations in this research. This leads to the following derivation:

$$\begin{aligned} \frac{d\tilde{M}_k}{d\tau_F} \Big|_F &= B(\tau_F) \tilde{g}_k \\ \Rightarrow \frac{d\tilde{M}_k}{d\tau_{Co}} \Big|_F \cdot \frac{K_{Co}}{\nu_{g0}^{1/6} K_F} &= B(\tau_{Co}) \tilde{g}_k \\ \Rightarrow \frac{d\tilde{M}_k}{d\tau_{Co}} \Big|_F &= B(\tau_{Co}) \frac{\nu_{g0}^{1/6} K_F}{K_{Co}} \tilde{g}_k \end{aligned}$$

The current research uses τ_{Co} to obtain a solution for the moment governing ordinary differential equation 3.8. Therefore, this report will use notation: $\tau = \tau_{Co}$ in further research content. Also, the extended correction function $B(\tau) \frac{\nu_{g0}^{1/6} K_F}{K_{Co}}$ is noted as: $\tilde{B}(\tau)$.

Concluding, the new expression for the differential moment equation for Brownian coagulation applicable for the entire regime yields:

$$\frac{d\tilde{M}_k}{d\tau} \Big|_D = \tilde{g}_k \left[\frac{1 + \tilde{B}(\tau) \frac{\tilde{g}_k}{2h_k}}{1 + a(\sigma) \tilde{B}(\tau) \frac{\tilde{g}_k}{2h_k} + 2 \left(\tilde{B}(\tau) \frac{\tilde{g}_k}{2h_k} \right)^2} \right] \quad (3.36)$$

3.2.5. SINK TERM

The last term to deal with is the sink term $\frac{dM_k}{dt} \Big|_{\text{sink}}$. Recall from Section 2.3:

$$\frac{\partial n_{\text{sink}}(v)}{\partial t} = - \frac{1.67}{R^2 \pi v^{1/3}} K_{Co} C(v) n(v) \quad (3.37)$$

$$C(v) = 1 + \frac{\lambda}{\sqrt[3]{\frac{3}{4\pi}}} v^{-\frac{1}{3}} \left(\alpha + \beta \exp \left(- \frac{\gamma}{\lambda} \sqrt[3]{\frac{3}{4\pi}} v^{\frac{1}{3}} \right) \right), \quad (3.38)$$

where $\alpha + \beta = 1.67, \gamma = 0$ [8].

Applying the MoM requires multiplying both sides of Equation 3.37 with v^k and integrating over the entire particle size range.

$$\int_0^\infty v^k \frac{dn_{\text{sink}}(v)}{dt} dv = \frac{d\tilde{M}_k}{dt} \Big|_{\text{sink}} = - \frac{1.67}{R^2 \pi} K_{Co} \int_0^\infty \left(v^{-\frac{1}{3}} + 2.69 \lambda v^{-\frac{2}{3}} \right) v^k n(v) dv$$

Applying Expression 3.2 for $k = 0, k = 1$ and $k = 2$ yields:

$$\begin{cases} \frac{d\tilde{M}_0}{dt} \Big|_{\text{sink}} = - \frac{1.67}{R^2 \pi} K_{Co} (M_{-1/3} + 2.69 \lambda M_{-2/3}) \\ \frac{d\tilde{M}_1}{dt} \Big|_{\text{sink}} = - \frac{1.67}{R^2 \pi} K_{Co} (M_{2/3} + 2.69 \lambda M_{1/3}) \\ \frac{d\tilde{M}_2}{dt} \Big|_{\text{sink}} = - \frac{1.67}{R^2 \pi} K_{Co} (M_{5/3} + 2.69 \lambda M_{4/3}) \end{cases}$$

Once more, Equations 3.11 - 3.13 allows closure of the set of ODEs:

$$\begin{cases} \frac{d\tilde{M}_0}{dt} \Big|_{\text{sink}} = - \frac{1.67}{R^2 \pi} K_{Co} (M_0^{\frac{14}{9}} M_1^{-\frac{7}{9}} M_2^{\frac{2}{9}} + 2.69 \lambda M_0^{\frac{20}{9}} M_1^{-\frac{16}{9}} M_2^{\frac{5}{9}}) \\ \frac{d\tilde{M}_1}{dt} \Big|_{\text{sink}} = - \frac{1.67}{R^2 \pi} K_{Co} (M_0^{\frac{2}{9}} M_1^{\frac{8}{9}} M_2^{-\frac{1}{9}} + 2.69 \lambda M_0^{\frac{5}{9}} M_1^{\frac{5}{9}} M_2^{-\frac{1}{9}}) \\ \frac{d\tilde{M}_2}{dt} \Big|_{\text{sink}} = - \frac{1.67}{R^2 \pi} K_{Co} (M_0^{-\frac{1}{9}} M_1^{\frac{5}{9}} M_2^{\frac{5}{9}} + 2.69 \lambda M_0^{-\frac{1}{9}} M_1^{\frac{8}{9}} M_2^{\frac{2}{9}}) \end{cases} \quad (3.39)$$

The final step is to nondimensionalize 3.39 using Expressions 3.20 and 3.21.

$$\begin{aligned} \left. \frac{d\widetilde{M}_0}{d\tau} \right|_{\text{sink}} &= -\frac{1.67}{N_0 R^2 \pi} \left(\widetilde{M}_0^{\frac{14}{9}} \widetilde{M}_1^{-\frac{7}{9}} \widetilde{M}_2^{\frac{2}{9}} \nu_{g0}^{-\frac{1}{3}} \exp\left(\frac{1}{2} \ln^2 \sigma_0\right) \dots \right. \\ &\quad \left. \dots + 2.67 \lambda \widetilde{M}_0^{\frac{20}{9}} \widetilde{M}_1^{-\frac{16}{9}} \widetilde{M}_2^{\frac{5}{9}} \nu_{g0}^{-\frac{2}{3}} \exp(2 \ln^2 \sigma_0) \right) \\ &\equiv \tilde{l}_0 \end{aligned} \quad (3.40)$$

$$\begin{aligned} \left. \frac{d\widetilde{M}_1}{d\tau} \right|_{\text{sink}} &= -\frac{1.67}{N_0 R^2 \pi} \left(\widetilde{M}_0^{\frac{20}{9}} \widetilde{M}_1^{-\frac{16}{9}} \widetilde{M}_2^{\frac{5}{9}} \nu_{g0}^{-\frac{1}{3}} \exp(2 \ln^2 \sigma_0) \dots \right. \\ &\quad \left. \dots + 2.67 \lambda \widetilde{M}_0^{\frac{5}{9}} \widetilde{M}_1^{\frac{5}{9}} \widetilde{M}_2^{-\frac{1}{9}} \nu_{g0}^{-\frac{2}{3}} \exp\left(\frac{1}{2} \ln^2 \sigma_0\right) \right) / \exp\left(\frac{9}{2} \ln^2 \sigma_0\right) \\ &\equiv \tilde{l}_1 \end{aligned} \quad (3.41)$$

$$\begin{aligned} \left. \frac{d\widetilde{M}_2}{d\tau} \right|_{\text{sink}} &= -\frac{1.67}{N_0 R^2 \pi} \left(\widetilde{M}_0^{-\frac{1}{9}} \widetilde{M}_1^{\frac{5}{9}} \widetilde{M}_2^{\frac{5}{9}} \nu_{g0}^{-\frac{1}{3}} \exp\left(\frac{25}{2} \ln^2 \sigma_0\right) \dots \right. \\ &\quad \left. \dots + 2.67 \lambda \widetilde{M}_0^{-\frac{1}{9}} \widetilde{M}_1^{\frac{8}{9}} \widetilde{M}_2^{\frac{2}{9}} \nu_{g0}^{-\frac{2}{3}} \exp(8 \ln^2 \sigma_0) \right) / \exp(18 \ln^2 \sigma_0) \\ &\equiv \tilde{l}_2 \end{aligned} \quad (3.42)$$

To maintain clear and understandable notations, the RHSs of Equations 3.40- 3.42 are noted in terms of \tilde{l}_k for the remainder of this thesis.

FINAL EXPRESSION FOR MOMENT GOVERNING ODE

Now that all terms are defined, Equation 3.36 is extended to formulate the expression for the dimensionless time derivative of the k^{th} moment accounting for coagulation and diffusion for the entire regime. This is an ordinary, nonlinear differential equation and is numerically approached in the next chapter.

$$\frac{d\widetilde{M}_k}{d\tau} = \tilde{g}_k \left[\frac{1 + \tilde{B}(\tau) \frac{\tilde{g}_k}{2\tilde{h}_k}}{1 + a(\sigma) \tilde{B}(\tau) \frac{\tilde{g}_k}{2\tilde{h}_k} + 2 \left(\tilde{B}(\tau) \frac{\tilde{g}_k}{2\tilde{h}_k} \right)^2} \right] + \tilde{l}_k \quad (3.43)$$

The dimensionless initial conditions are derived by writing Equation 3.20 in terms of \widetilde{M}_k :

$$\widetilde{M}_k(0) = \frac{1}{M_k(0)} N_0 \nu_{g0}^k \exp\left(\frac{9}{2} k^2 \ln^2 \sigma_0\right) = 1 \quad 0 < \tau < \tau_R \quad (3.44)$$

Note, all quantities in Equation 3.43 have been defined in previous sections and an overview is listed in Appendix B.1.

4

NUMERICAL ANALYSIS

The ordinary, nonlinear differential equation for the dimensionless k^{th} moment accounting for coagulation and diffusion of nanoparticles for the entire regime is repeated here:

$$\frac{d\widetilde{M}_k}{d\tau} = \widetilde{g}_k \left[\frac{1 + \widetilde{B}(\tau) \frac{\widetilde{g}_k}{2\widetilde{h}_k}}{1 + a(\sigma)\widetilde{B}(\tau) \frac{\widetilde{g}_k}{2\widetilde{h}_k} + 2\left(\widetilde{B}(\tau) \frac{\widetilde{g}_k}{2\widetilde{h}_k}\right)^2} \right] + \widetilde{l}_k \quad (4.1)$$

Recall that all terms are defined in Appendix B.1.

Equation 4.1 is too complex to solve analytically, therefore the solution is approximated using numerical methods. To do so, the model applies the Forward Euler- and Modified Euler numerical discretization method, explained in Section 4.1. The corresponding stepsize $\Delta\tau$ is analyzed to obtain a value which is computationally attractive and which leads to acceptable truncation errors in Section 4.2. The accuracy of the implementation of the model is analyzed by estimating the order of the error in Section 4.3 and the computational efficiency is presented in Section 4.4. A motivation for applying Forward Euler is given in the final section.

4.1. NUMERICAL METHODS

To maintain simple notations, the right-hand side of Equation 4.1 is joined to formulate one nonlinear function \widetilde{f}_k . The corresponding first - order initial value problem yields:

$$\begin{cases} \frac{d\widetilde{M}_k}{d\tau} = \widetilde{f}_k(\tau, \widetilde{M}_0, \widetilde{M}_1, \widetilde{M}_2) & \tau > \tau_0, \quad k = \{0, 1, 2\} \\ \widetilde{M}_k(\tau_0) = \widetilde{M}_{k,0} \end{cases} \quad (4.2)$$

Integrating and approximating the solution for a discrete timestep τ_{n+1} obtains:

$$\widetilde{M}_{k,n+1} = \widetilde{M}_{k,n} + \int_{\tau_n}^{\tau_{n+1}} \widetilde{f}_k(\tau, \widetilde{M}_0, \widetilde{M}_1, \widetilde{M}_2) d\tau \quad (4.3)$$

The integral in Equation 4.3 considers only one time interval, therefore single-step numerical methods are used to approximate the solution [30]. Forward Euler is a relatively simple, explicit method and is initially applied to the model. It approximates the step by multiplying the step length by the derivative at the start of the interval [16]:

$$\widetilde{M}_{k,n+1} = \widetilde{M}_{k,n} + \Delta\tau \widetilde{f}_k(\tau_n, \widetilde{M}_{0,n}, \widetilde{M}_{1,n}, \widetilde{M}_{2,n}) \quad (4.4)$$

Modified Euler is another easy to implement, explicit numerical method and has a higher accuracy when approximating the solution.

$$\begin{aligned} \text{predictor: } \widetilde{M}_{k,n+1}^* &= \widetilde{M}_{k,n} + \Delta\tau \widetilde{f}_k(\tau_n, \widetilde{M}_{0,n}, \widetilde{M}_{1,n}, \widetilde{M}_{2,n}) \\ \text{corrector: } \widetilde{M}_{k,n+1} &= \widetilde{M}_{k,n} + \frac{\Delta\tau}{2} \left(\widetilde{f}_k(\tau_n, \widetilde{M}_{0,n}, \widetilde{M}_{1,n}, \widetilde{M}_{2,n}) + \widetilde{f}_k(\tau_n, \widetilde{M}_{0,n+1}^*, \widetilde{M}_{1,n+1}^*, \widetilde{M}_{2,n+1}^*) \right) \end{aligned} \quad (4.5)$$

Both schemes are implemented in the model and analyzed in terms of stability, accuracy, running time and their impact on results.

4.2. STEPSIZE

An input of the model that has no physical representation (in contrast to the initial concentration or tube length) but that is of great importance for the performance of the model, is the dimensionless stepsize $\Delta\tau$. It is dependant on the dimensional stepsize by:

$$\Delta\tau = hN_0K_{Co},$$

where h it the stepsize:

$$h = \frac{t_R}{S}$$

Here, t_R is the residence time and S^1 is the total amount of steps.

CHOICE OF h

A first estimation for h is done based on the physical problem. A typical residence time is approximately equal to one second. Obviously, a stepsize of $h = 0.5s$ is unsuitable. Furthermore, the stability of the model is determined by Δt , which is defined by the product of h , N_0 and the coagulation constant K_{Co} . Test runs were performed to derive a stability condition. Computational errors prevented the model to finish calculations if the stepsize is taken too large for large N_0 . Table 4.1 lists the results for stability tests which were performed for both schemes². This leads to an empirical condition for a stable stepsize which is N_0 -dependant.

$$\text{Forward Euler} \quad hN_0 < 1 \times 10^{14} \quad (4.6)$$

$$\text{Modified Euler} \quad hN_0 < 2 \times 10^{14} \quad (4.7)$$

Test	N_0 [m ⁻³]	Euler Forwards			Modified Euler		
		h	S	stability	h	S	stability
1	1×10^{17}	1.14×10^{-3}	441	yes	2.08×10^{-3}	241	yes
2	1×10^{17}	1.16×10^{-3}	431	no	2.17×10^{-3}	231	no
3	1×10^{18}	1.22×10^{-4}	4101	yes	2.38×10^{-4}	2101	yes
4	1×10^{18}	1.25×10^{-4}	4001	no	2.5×10^{-4}	2001	no
5	1×10^{19}	1.22×10^{-5}	41001	yes	2.38×10^{-5}	21001	yes
6	1×10^{19}	1.25×10^{-5}	40001	no	2.5×10^{-5}	20001	no
7	1×10^{20}	1.24×10^{-6}	400001	yes	2.38×10^{-6}	210001	yes
8	1×10^{20}	1.25×10^{-6}	390001	no	2.5×10^{-6}	200001	no

Table 4.1: Stability tests for various N_0 and h

¹In numerical mathematics, the total amount of steps in a numerical problem is usually noted with N . However, this thesis already defines N as the total concentration of nanoparticles. To avoid confusion the total amount of steps is notated with S in this research.

²Note, K_{Co} is gas dependent and was calculated for argon during these tests. Conditions 4.6 and 4.7 may need to be redefined for other gases.

THEORETICAL ANALYSIS OF h

[30] states that the stepsize h is stable if the order of the global error of the numerical method can be estimated by:

$$\frac{M_{k,t,h/2} - M_{k,t,h}}{M_{k,t,h/4} - M_{k,t,h/2}} \approx 2^p, \quad (4.8)$$

where $M_{k,t,h}$ is the solution computed by the model at time t using stepsize h and p is the order of the numerical method ($p = 1$ for Forward Euler, $p = 2$ for Modified Euler). Equation 4.8 is called the linearity test and is executed using Richardson Extrapolation [30].

The linearity test is performed for the maximum stable stepsize under the conditions 4.6 and 4.7. It is met for over 98% of the time for both methods. The remaining 2% are outliers. This occurs when two values in Equation 4.8 differ by many orders of magnitude and cannot be treated correctly by floating-point operations [31]. These outliers decrease for smaller timesteps and do not indicate any instability of h . An example is shown in Figure 4.1, where the linearity test is performed for the first moment computed with the Forward Euler method.

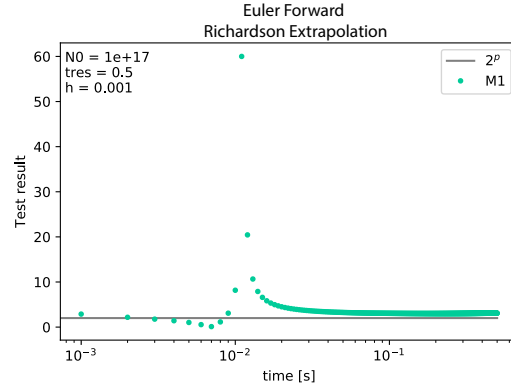


Figure 4.1: Richardson Extrapolation performed on M_1 for Euler Forward.

THEORETICAL ANALYSIS OF $\Delta\tau$

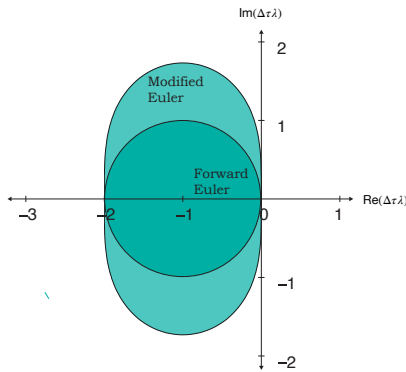
For most ordinary differential problems, both numerical methods obtain equivalent stepsize stability conditions. However, this is shown not to be the case in the present study. In theory, it is possible to compute the exact stability of the stepsize $\Delta\tau$ [30]. For this it is necessary to compute the eigenvalues $\lambda = \mu + i\nu$ of the Jacobian matrix:

$$J_n = \begin{bmatrix} \frac{\partial \tilde{f}_0}{\partial \tilde{M}_0} & \frac{\partial \tilde{f}_0}{\partial \tilde{M}_1} & \frac{\partial \tilde{f}_0}{\partial \tilde{M}_2} \\ \frac{\partial \tilde{f}_1}{\partial \tilde{M}_0} & \frac{\partial \tilde{f}_1}{\partial \tilde{M}_1} & \frac{\partial \tilde{f}_1}{\partial \tilde{M}_2} \\ \frac{\partial \tilde{f}_2}{\partial \tilde{M}_0} & \frac{\partial \tilde{f}_2}{\partial \tilde{M}_1} & \frac{\partial \tilde{f}_2}{\partial \tilde{M}_2} \end{bmatrix}_n$$

The theoretical stability conditions for $\Delta\tau$ are defined by:

$$\text{Forward Euler: } |1 + \Delta\tau| < 1 \quad (4.9)$$

$$\text{Modified Euler: } |1 + \Delta\tau + \frac{1}{2}(\Delta\tau\lambda)^2| < 1, \quad (4.10)$$



The corresponding stability regions for the complex $h\lambda$ -plane are shown in Figure 4.2. The extent and the non-linearity of Equation 4.1 makes the analytical computation of the Jacobian and its eigenvalues unfeasible. However, the difference in stable stepsize observed in Table 4.1 implies that the eigenvalues are complex, since real eigenvalues yield equal stability conditions for the two numerical methods.

Figure 4.2: stability regions for $\Delta\tau$ on $\Delta\tau\lambda$ -plane

4.3. ORDER OF ERROR

A model is stable if a small deviation of the input parameters gives a small deviation of the solution [30].

Definition 1 *The global truncation error is the cumulative error caused by many iterations and defined as:*

$$e_n = y_n - w_n, \quad (4.11)$$

where e_n is the global error after n time steps, y is the exact solution and w is the numerical approximation of the solution.

The global errors are computed for both schemes at $n = S$ (i.e. at time t_R) for $h, \frac{h}{2}, \frac{h}{4}, \frac{h}{8}, \frac{h}{16}, \frac{h}{32}$. By absence of an analytical solution, the "exact" solution is approximated using a stepsize which is one thousand times smaller than the original stepsize: $h_{\text{exact}} = \frac{h}{1000}$. Both models use the same initial conditions:

$$N_0 = 1 \times 10^{17}, \quad t_R = 0.5\text{s}, \quad h = 0.001$$

The relative error \bar{e} is obtained by scaling the global error with the exact k^{th} moment at time t_R .

$$\bar{e}_{k,h} = \frac{|M_{k,t_R,\text{exact}} - M_{k,t_R,h}|}{M_{k,t_R,\text{exact}}} \quad (4.12)$$

The global and relative error of Euler Forwards is $O(h)$ [30], meaning that the error is proportionate to the stepsize h . Figure 4.3 shows indeed that the numerical error resulting from Forward Euler obtains the same slope as the stepsize (blue), complying with the theory. Modified Euler obtains an error of $O(h^2)$, meaning that the error is proportionate to h^2 . In other words, given stepsize h with error \bar{e} , then the halved stepsize $h/2$ yields a numerical error of $\bar{e}/4$. This corresponds with the results in Figure 4.3.

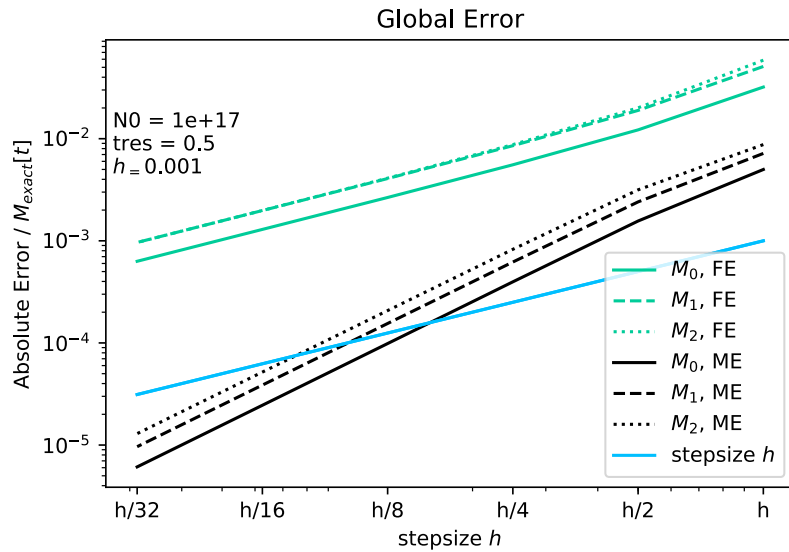


Figure 4.3: Global Error for Forward Euler and Modified Euler numerical approximation methods.

4.4. COMPUTATIONAL EFFICIENCY

The efficiency of the model and numerical methods is analyzed in terms of computational time. Model runs were performed for three initial conditions which correspond to a range applicable for the VSP-G1. For each test, the maximum stepsize was used according to Conditions 4.6 and 4.7.

N_0 [m ⁻³]	Computational time [s]	
	Forward Euler	Modified Euler
1×10^{18}	1.1	1.13
1×10^{19}	10.4	10.7
1×10^{20}	111.7	115.8

Table 4.2: Computational Efficiency tests

Table 4.2 shows that the computational time is proportionate to the initial concentration. The maximum running time is just under two minutes, which is acceptable for this study.

4.5. CONCLUSION

The Modified Euler numerical method is proven to be more accurate in terms of numerical errors than Euler Forward. However, Euler Forward is simpler to implement and slightly faster than Modified Euler, hence computationally more attractive.

Moreover, the model is based on a list of assumptions to approximate the actual behaviour of hundreds of billions of nanoparticles. The errors originating from these assumptions are quantified in Chapter 6 and estimated to be considerably larger than any numerical error. Therefore, the contribution of the Modified Euler method in terms of model accuracy is negligible, allowing the Forward Euler method to be sufficient for this research.

5

VALIDATION WITH THEORETICAL RESULTS

It is important to validate the model with theoretical results. This chapter uses various works of Lee et. al. to test certain aspects of the model.

In 1984, Lee et. al. [6] used the method of moments to obtain a particle size distribution for aerosol particles in a closed space in the free molecular regime. Characterizing parameters such as the dimensionless particle concentration N/N_0 , mean geometric volume v_g/v_{g0} and geometric spread of the size σ were used to reconstruct the dimensionless PSD. The results obtained from Lee's research are used to validate the mathematical model of the current research. In theory, when coagulation occurs in a closed space the corresponding particle size distribution approaches a log-normal size distribution with constant geometric standard deviation σ_∞ [1]. This principle is tested in Section 5.1.

The transition regime is implemented using the set of ODEs derived in Section 3.2.4 and tested by analyzing the characteristic, asymptotic behaviour of the geometric standard deviation. Section 5.2 quantifies the impact of adding the transition regime to the original model.

The sink term is analyzed with respect to previous research conducted by Lee and Gieseke ?? in Section 5.3. Diffusion effects are computed to determine its theoretical impact on nanoparticle growth.

Note that all parameters in this chapter are in dimensionless form, scaled to their corresponding values at $t = 0$. The initial values used in the theory are unknown to the present study. Therefore, the scales obtained in this study may not comply with the theoretical plots in absolute sense. Still, the model is sufficiently validated when obtaining equivalent qualitative behaviour between theoretical- and computed results.

5.1. VALIDATION OF MOM

The model in its simplest form simulates pure coagulation of spherical nanoparticles in the constant free molecular regime and neglects diffusion effects. It obtains the following format for the Smoluchowski equation:

$$\frac{\partial n(v, t)}{\partial t} = \frac{1}{2} \int_0^v \beta_F(v', v - v') n(v', t) n(v - v', t) dv' - n(v, t) \int_0^\infty \beta_F(v, v') n(v', t) dv'$$

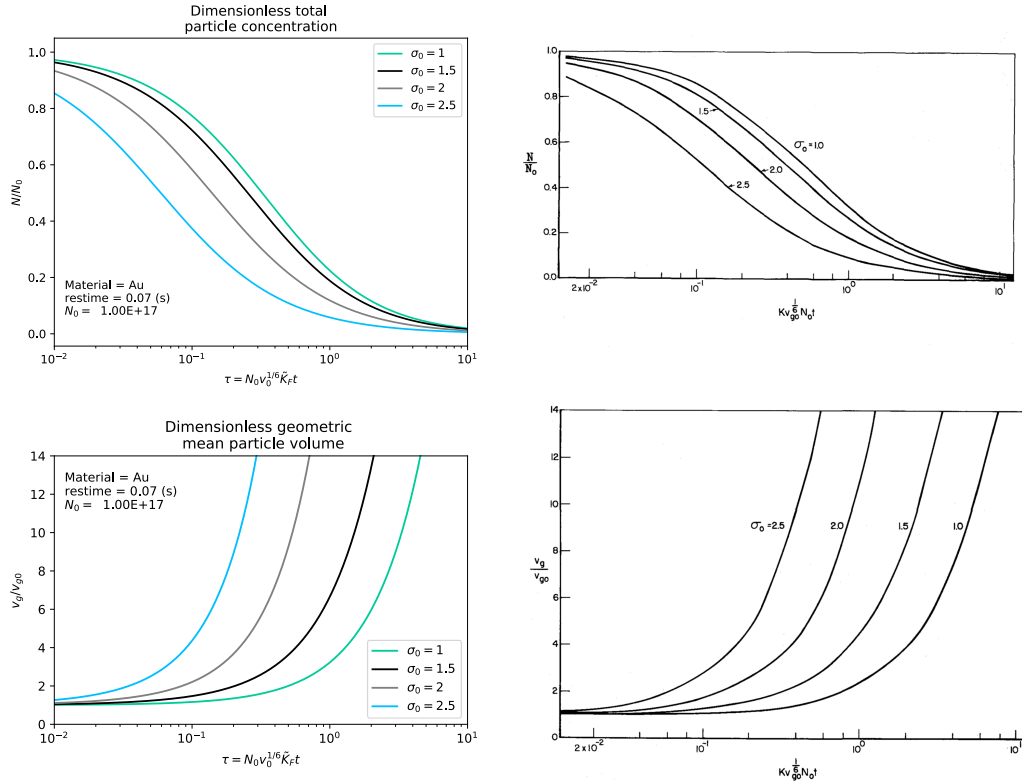
which is converted to a set ordinary differential problem in Section 3.2.2. Recall Equations 3.23 - 3.25:

$$\begin{aligned}\frac{d\widetilde{M}_0}{d\tau_F} &= -B(\tau) \left(\widetilde{M}_0^{\frac{151}{72}} \widetilde{M}_1^{-\frac{13}{36}} \widetilde{M}_2^{\frac{19}{72}} \exp\left(\frac{25}{8} \ln^2 \sigma_0\right) \dots \right. \\ &\quad \dots + 2\widetilde{M}_0^{\frac{131}{72}} \widetilde{M}_1^{\frac{7}{36}} \widetilde{M}_2^{-\frac{1}{72}} \exp\left(\frac{5}{8} \ln^2 \sigma_0\right) \dots \\ &\quad \left. \dots + \widetilde{M}_0^{\frac{127}{72}} \widetilde{M}_1^{\frac{11}{36}} \widetilde{M}_2^{-\frac{5}{72}} \exp\left(\frac{1}{8} \ln^2 \sigma_0\right) \right) \\ \frac{d\widetilde{M}_1}{d\tau_F} &= 0 \\ \frac{d\widetilde{M}_2}{d\tau_F} &= 2B(\tau) \left(\widetilde{M}_0^{\frac{19}{72}} \widetilde{M}_1^{\frac{47}{36}} \widetilde{M}_2^{\frac{31}{72}} \exp\left(\frac{109}{8} \ln^2 \sigma_0\right) \dots \right. \\ &\quad \dots + 2\widetilde{M}_0^{-\frac{7}{72}} \widetilde{M}_1^{\frac{67}{36}} \widetilde{M}_2^{\frac{11}{72}} \exp\left(\frac{89}{8} \ln^2 \sigma_0\right) \dots \\ &\quad \left. \dots + \widetilde{M}_0^{-\frac{5}{72}} \widetilde{M}_1^{\frac{71}{36}} \widetilde{M}_2^{\frac{7}{72}} \exp\left(\frac{85}{8} \ln^2 \sigma_0\right) \right) / \exp(18 \ln^2 \sigma_0)\end{aligned}$$

for $0 < \tau < \tau_R$ and initial conditions:

$$\begin{aligned}\widetilde{M}_0(0) &= \frac{1}{M_0(0)} N_0 = 1 \\ \widetilde{M}_1(0) &= \frac{1}{M_1(0)} N_0 \nu_{g0} \exp\left(\frac{9}{2} \ln^2 \sigma_0\right) = 1 \\ \widetilde{M}_2(0) &= \frac{1}{M_2(0)} N_0 \nu_{g0}^2 \exp(18 \ln^2 \sigma_0) = 1\end{aligned}$$

The plots in Figure 5.1 are derived by solving equations listed above and correspond to those obtained from Lee et. al [6]. The results show equivalent trends and are even comparable in absolute sense, confirming a correct implementation of the method of moments.



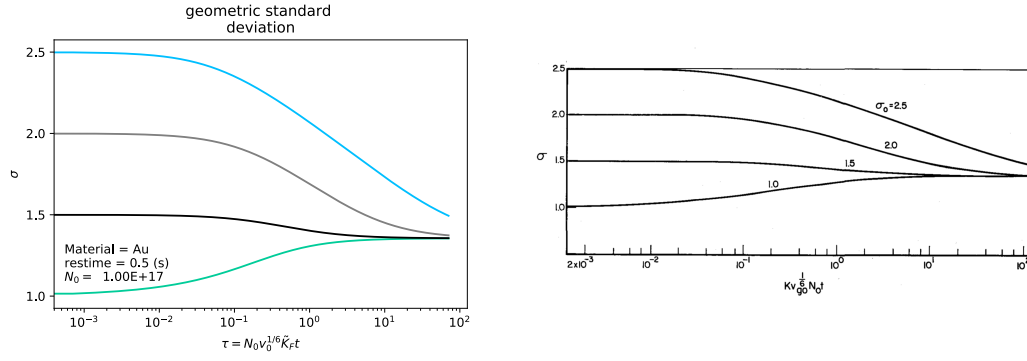


Figure 5.1: Computational model (left), theory from [6] (right), both free molecular regime.

SELF-PRESERVING SIZE DISTRIBUTION

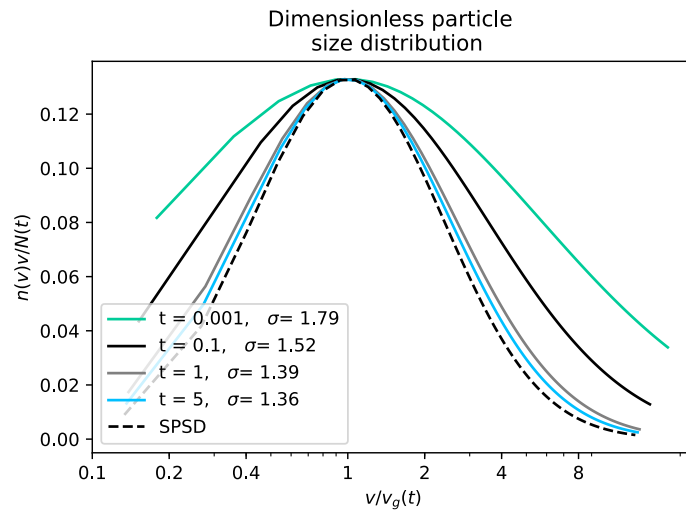
When coagulation occurs in a closed space, it is possible to write the PSD in dimensionless form [3], becoming invariant with respect to time. The dimensionless PSD approaches a log-normal distribution with a constant geometric standard deviation $\sigma_\infty = 1.355$ as $t \rightarrow \infty$. The so called self-preserving size distribution (SPSD) is a function of the dimensionless volume $\eta = \frac{v}{v_g}$:

$$\varphi(\eta) = \frac{n(v)v}{N} = \frac{1}{3\sqrt{2\pi}\ln\sigma_\infty} \exp\left[\frac{-\ln^2(\eta)}{18\ln^2(\sigma_\infty)}\right], \quad (5.1)$$

where v_g is the geometric mean particle volume and N is the total particle concentration. An equivalent, time-dependent form of the distribution function is derived when writing the PSD defined in Equation 3.9 in terms of $N/N(\tau)$ and $v/v_g(\tau)$,

$$\frac{n(v, \tau)v}{N(\tau)} = \frac{1}{3\sqrt{2\pi}\ln\sigma(\tau)} \exp\left[\frac{-\ln^2(v/v_g(\tau))}{18\ln^2(\sigma(\tau))}\right], \quad (5.2)$$

The dimensionless particle size distribution computed by the model is expected to approach Equation 5.1. The time required to reach the SPSP depends on the dispersity of the initial size distribution σ_0 and initial particle concentration N_0 . Figure 5.2 shows that the model satisfies the property of approaching a self-preserving size distribution with σ_∞ .

Figure 5.2: Dimensionless particle size distribution converges to the self-preserving size distribution for initial conditions: $N_0 = 1e17$, $\sigma_0 = 1.8$ after around 1 s.

5.2. TRANSITION REGIME

An important element to incorporate in the model is the effect of entering a new regime. Once the particle diameter exceeds a value of five nanometers, the collision frequency kernel will gradually shift from free-molecular to transition [9] due to increasing continuum effects. The implementation of the transition regime required the introduction of $\tilde{B}(\tau)$ which converts the dimensionless timestep τ_F (Recall Section 3.2.4). To the best of our knowledge, this method for the implementation of the transition regime is new to this field of research, therefore a proper validation process is necessary.

The geometric standard deviation is characterized by its asymptotic behaviour regardless of the regime an aerosol originates from [7] or the initial dispersity. The value of the asymptote characterizes the regime in which nanoparticles endure (Figure 5.3). In the free molecular regime, the geometric spread starts at $\sigma_\infty = 1.335$, then decreases a bit in the transition regime before climbing to 1.320 in the continuum regime. The equivalent behaviour is shown for the computed geometric standard deviation using β_D for the regime range applicable for this research.

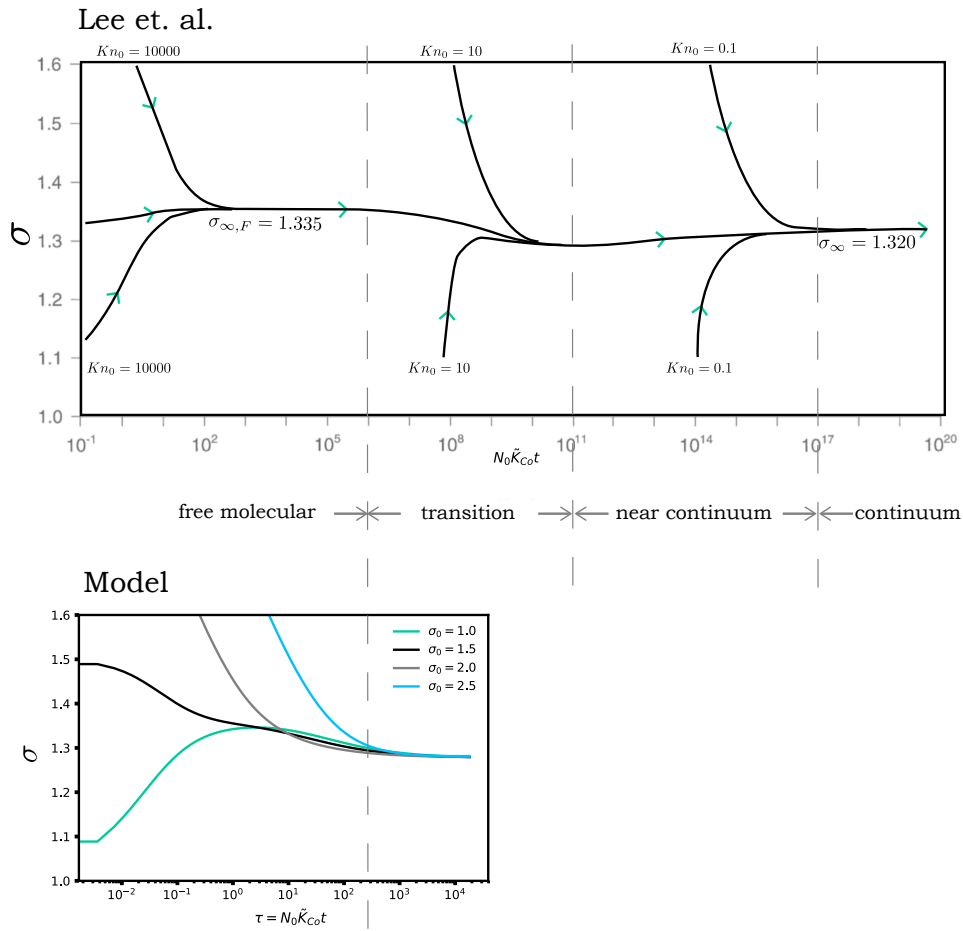


Figure 5.3: Asymptotic behaviour of geometric standard deviation generated by [7] (top) and model (bottom). Note, different x-scales are due to unknown scaling conditions in [7].

Note, to compute σ up to the continuum regime, the model requires the incorporation of a logarithmic increasing computational stepsize. Instead, this research choose to use another validation approach by analyzing the physical behaviour of entering the transition regime in the next section¹.

¹A third validation method using the geometric standard deviation that ensures equivalent x-axis values is discussed in Chapter 7

ENTERING THE TRANSITION REGIME VS. REMAINING IN THE FREE MOLECULAR REGIME

Since it is known that the expression for β_D gradually shifts from β_F to β_{Co} , the transition model should provide the same results as the free molecular model for small particles ($d_p < 5$ nm). In other words, particles haven't "entered" the transition regime yet and the kernel is not affected by continuum mechanisms. This hypothesis is shown to be true in Figures 5.4a and 5.4b where the initial particle concentration is 1×10^{14} particles per m^{-3} and the residence time is 0.5 s.

By increasing the initial concentration to $N_0 = 1 \times 10^{19} m^{-3}$, the chance of particle collisions and fusion increases significantly (Figures 5.4c and 5.4d). The result is a faster decrease in particle concentration, and an overall increase in particle diameter.

Particles gradually enter the transition regime around the dotted line. Under these conditions and after a residence time of 1 s, there is no visible difference between the two models in terms of particle concentration (green). However, there is a sufficient distinction when analyzing the particle diameter growth over time (black). This concludes that the transition regime is especially important to take into account when aiming to control particle sizes at nanometer accuracy.

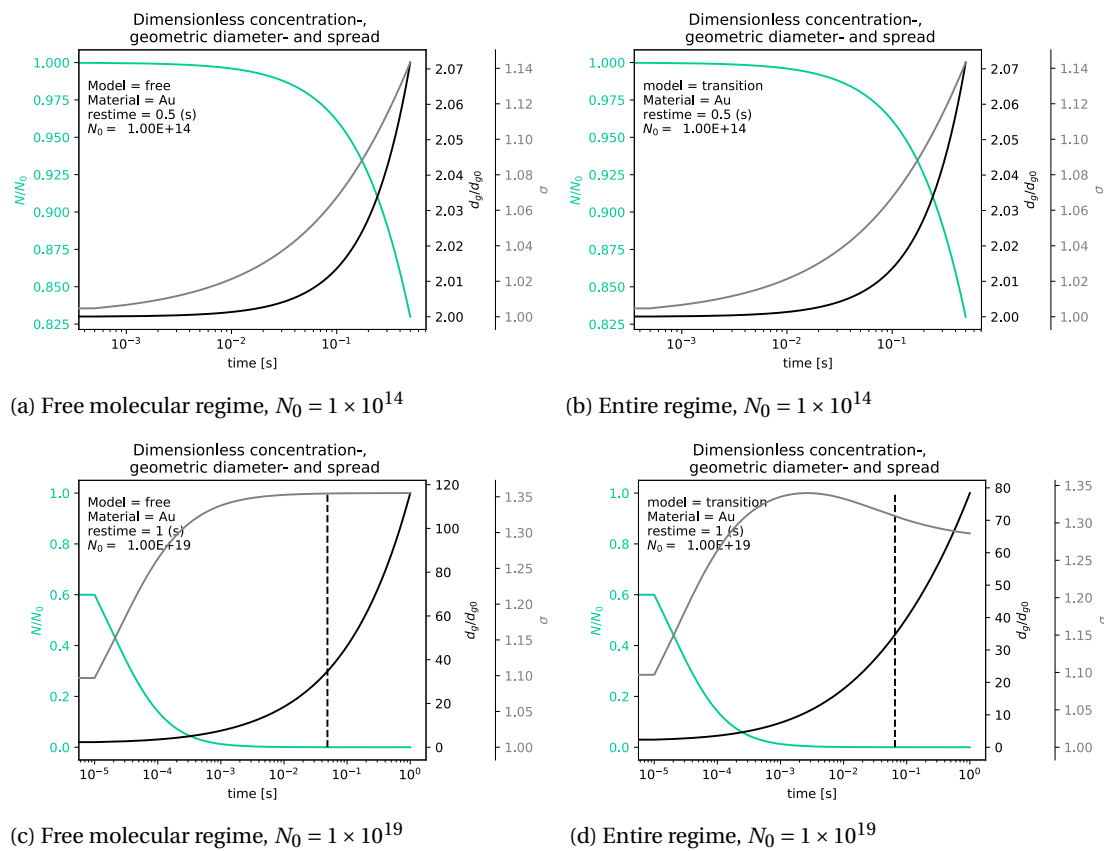


Figure 5.4: Characterizing dimensionless parameters N/N_0 , d/d_0 and σ under various N_0 in m^{-3} for the free molecular regime (left) and the entire regime (right).

5.3. DIFFUSION EFFECTS

Now that the transition model and the implementation of the method of moments is validated, it remains to study behaviour of the sink term. The penetration of aerosol in transport is defined as the percentage of the total initial particle concentration that is *not* deposited onto the tube wall throughout the time of transport. Lee and Gieseke presented an approach using the method of moments for calculating the fractional penetration of a log-normally distributed aerosol in a circular channel [8]. The current research nondimensionalized Lee's set of ODE's and converted it to be dependant on time

instead of space. Recall the moment equation consisting of diffusion effects only from Section 3.2.5

$$\frac{dM_k}{dt} \Big|_{\text{sink}} = -\frac{1.67}{R^2\pi} K_{Co} \int_0^\infty (v^{-\frac{1}{3}} + 2.69\lambda v^{-\frac{2}{3}}) v^k n(v, t) dv,$$

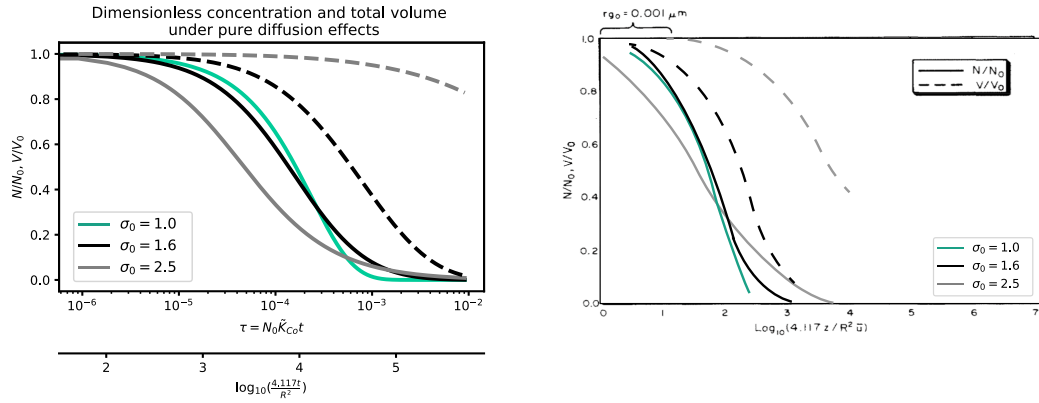
and corresponding the ordinary differential equations:

$$\begin{aligned} \frac{d\widetilde{M}_0}{d\tau} \Big|_{\text{sink}} = & -\frac{1.67}{N_0 R^2 \pi} \left(\widetilde{M}_0^{\frac{14}{9}} \widetilde{M}_1^{-\frac{7}{9}} \widetilde{M}_2^{\frac{2}{9}} v_{g0}^{-\frac{1}{3}} \exp\left(\frac{1}{2} \ln^2 \sigma_0\right) \dots \right. \\ & \left. \dots + 2.67\lambda \widetilde{M}_0^{\frac{20}{9}} \widetilde{M}_1^{-\frac{16}{9}} \widetilde{M}_2^{\frac{5}{9}} v_{g0}^{-\frac{2}{3}} \exp(2 \ln^2 \sigma_0) \right) \end{aligned}$$

$$\begin{aligned} \frac{d\widetilde{M}_1}{d\tau} \Big|_{\text{sink}} = & -\frac{1.67}{N_0 R^2 \pi} \left(\widetilde{M}_0^{\frac{20}{9}} \widetilde{M}_1^{-\frac{16}{9}} \widetilde{M}_2^{\frac{5}{9}} v_{g0}^{-\frac{1}{3}} \exp(2 \ln^2 \sigma_0) \dots \right. \\ & \left. \dots + 2.67\lambda \widetilde{M}_0^{\frac{5}{9}} \widetilde{M}_1^{\frac{5}{9}} \widetilde{M}_2^{-\frac{1}{9}} v_{g0}^{-\frac{2}{3}} \exp\left(\frac{1}{2} \ln^2 \sigma_0\right) \right) / \exp\left(\frac{9}{2} \ln^2 \sigma_0\right) \end{aligned}$$

$$\begin{aligned} \frac{d\widetilde{M}_2}{d\tau} \Big|_{\text{sink}} = & -\frac{1.67}{N_0 R^2 \pi} \left(\widetilde{M}_0^{-\frac{1}{9}} \widetilde{M}_1^{\frac{5}{9}} \widetilde{M}_2^{\frac{5}{9}} v_{g0}^{-\frac{1}{3}} \exp\left(\frac{25}{2} \ln^2 \sigma_0\right) \dots \right. \\ & \left. \dots + 2.67\lambda \widetilde{M}_0^{-\frac{1}{9}} \widetilde{M}_1^{\frac{8}{9}} \widetilde{M}_2^{\frac{2}{9}} v_{g0}^{-\frac{2}{3}} \exp(8 \ln^2 \sigma_0) \right) / \exp(18 \ln^2 \sigma_0) \end{aligned}$$

Solving this ordinary differential problem results in Figure 5.5a. These computational results are used to validate the sink term with theoretical results obtained by [8] in Figure 5.5b. Though the two plots do not match in terms of absolute values due to different values for tube radius R and time t (= flow velocity u and tube length z in theoretical definition) the trends definitely agree, implying a sufficient implementation.



(a) dimensionless parameters computed by the model

(b) dimensionless parameters by Lee and Gieseke

Figure 5.5: Diffusion effects on the dimensionless total particle concentration (—) and dimensionless particle volume (---) for various σ_0 . Computational results (left), theoretical results (right) [8].

IMPACT OF SINK TERM

The addition of the sink term should generate a larger decrease in particle concentration and break the preservation of total particle volume (represented by M_1). Figure 5.6 shows the impact of the sink term on the course of four critical parameters over time, for two initial concentrations (black and green). Overall it is shown that diffusion has a greater impact on aerosol with relatively small N_0 , suggesting that the impact of diffusion is not proportional to the particle concentration.

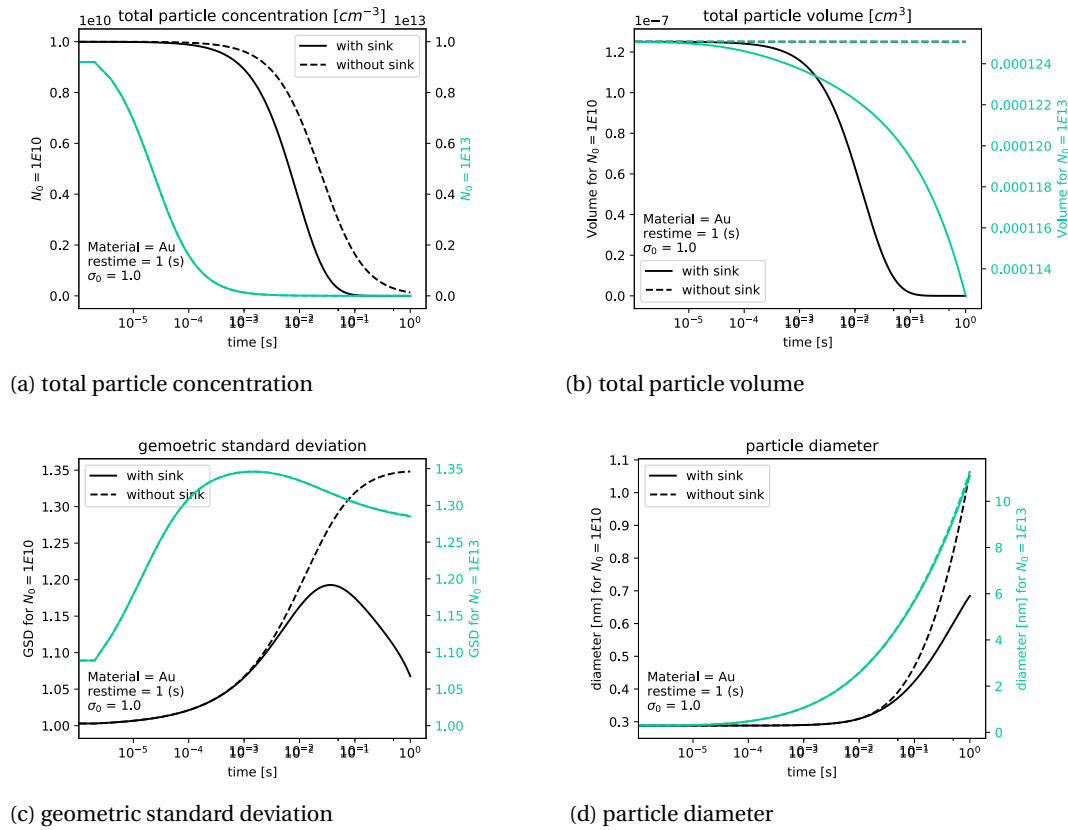


Figure 5.6: Diffusion effects on nanoparticle properties after 1 s for varying N_0 in cm^{-3}

For an initial concentration $N_0 = 1 \times 10^{10} \text{ cm}^{-3}$ (black), the affect of particle diffusion influences the particle growth (Figure 5.6d). Incorporating diffusion results in a mean particle diameter of 6 nm after 1 s, while neglecting the sink term allows particles to grow to 10 nm in diameter. Figure 5.6b shows that the total particle volume is preserved when diffusion of nanoparticles to the walls is excluded. Logically, this property ceases when the sink term is included. For aerosols with small initial concentrations all particles have endured diffusion effects after a certain amount of time, leaving almost no particles in the aerosol concentration. The result is a sudden decrease in geometric standard deviation, disregarding its asymptotic behaviour (Figure 5.6c).

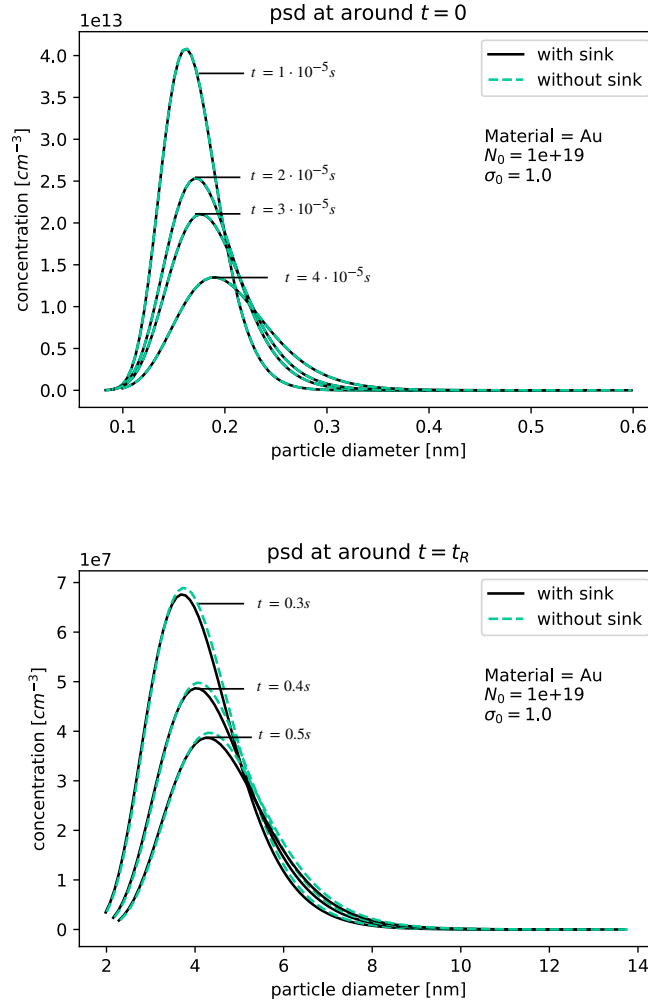


Figure 5.7: particle size distribution for various moments in time, N_0 in m^{-3}

The green plots in Figure 5.6 are computed results with initial conditions corresponding to the standard settings of the VSP-G1. Since the values for both models (with- and without sink) overlap, it is stated that under these conditions, diffusion implemented according to [8] has no significant affect on the characteristic properties of the aerosol. Never the less, the values for N , d_p and σ are used to construct the particle size distribution for various moments in time, shown in Figure 5.7. The top graph analyzes the first period of the residence time while the bottom graph zooms in on the last few tenths of the second. Though the effect is minimal, over time the PSD slightly skews to the left when including the sink term. This corresponds to the physical mechanisms in the VSP-G1: the longer the duration of particles inside the system, the more particles diffuse towards the wall, leading to a lower concentration of interacting particles, hence a lower particle growth rate.

6

VALIDATION WITH EXPERIMENTAL RESULTS

Now that model complies with the theory, the model is tested to comply with the output of the VSP nanoparticle generator. This is done by comparing numerical results obtained from the model with measurements obtained from actual experiments.

Twenty experiments have been performed to obtain the mode, the total concentration and the geometric standard deviation of the particle size distribution for various VSP-G1 settings. The mode is equal to the particle size with the highest concentration (i.e. the local maximum of the PSD). The experimental results were compared to the model predictions using initial conditions that are based on the experimental settings. In order to obtain the same format for the particle size distribution as that of the model, the raw measurements undergo a data conversion. This validation process is described in detail in Section 6.1.

The initial conditions for the model are computed by means of approximation formulas which are in direct relation with the settings of the experiment. Recall that the model is deterministic, meaning that it ignores random variation, and will always predict the same outcome from a given input ?? (i.e. system settings). Nanoparticle growth is influenced by Brownian Motion. Consequently, the probability that the VSP-G1 will output the exact equivalent aerosol composition for multiple experiments with constant system settings is extremely low. Therefore, upper and lower bounds for the model output are computed by taking uncertainty factors for the initial conditions into account. The approximation formulas and corresponding uncertainty factors are introduced in Section 6.2.

Next, the experimental and model results are presented in Section 6.3, completing the validation process. A suitable relation is presented between the VSP-G1 settings for power and flowrate, and the mode of the PSD. Accuracy ranges are presented for the mode, total concentration and geometric standard deviation in terms maximum deviation between the modelled predictions and experimental results.

Section 6.4 compares the modelled increase in geometric mean particle size over time with a theoretical formula corresponding to pure, monodisperse coagulation [1]. When assuming that the model predictions hold a sufficient accuracy, a corrected formula is presented for the evolution of the particle size.

The results presented in this chapter provide an improved scientific understanding of the VSP-G1, insights on the sensitivity of the main input parameters, and can perform as an operational guide for the particle generator.

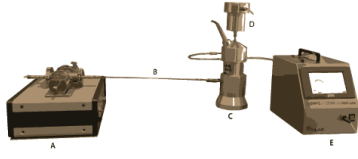

	Experiment	Model
SET-UP		
INPUT	<ul style="list-style-type: none"> • Tube dimensions V • Power P • Flow- and gastype Q • Material • Ablation rate m_A (provided by mass measurements) 	<ul style="list-style-type: none"> • Initial concentration N_0 • Residence time t_R
PROCESS	<p>SPMS measures raw data</p> <p>✓ data conversion</p> <p>$n(d_p), N(t_R)$</p> <p>✓ log-normal fit</p>	<p>Model computations</p> <p>✓</p> <p>$v_g, \sigma, N(t_R)$</p> <p>✓ log-normal fit</p>
OUTPUT	<ul style="list-style-type: none"> • Mode d_M • Total concentration $N(t_R)$ • Geometric std σ 	<ul style="list-style-type: none"> • Mode d_M • Total concentration $N(t_R)$ • Geometric std σ

Figure 6.1: Experimental validation process.

6.1. PROCESS

The input for the model is derived by means of the following approximation formulas¹:

$$N_0 = \frac{m_A N_A P}{Q}, \quad (6.1)$$

$$t_R = \frac{V}{Q}, \quad (6.2)$$

where m_A is the material dependent ablation rate in [mol/J], N_A is Avogadro's number, P is the power in [J/s], Q is the flowrate in [m³/s], and V is the combined volume of the VSP-G1 reactor chamber, the tube and the measuring system itself. Most parameters in Formulas 6.1 and 6.2 follow directly from the experimental input settings (see Figure 6.1). In contrast, the ablation rate is derived empirically from mass measurements which were performed parallel to particle size distribution measurements of the gas.

¹Derived in collaboration with VSPARTICLE engineers

The size of nanoparticles can be measured using direct or indirect methods. Direct methods are based on microscopy and indirect methods are based on the interaction of these particles with electromagnetic fields. An indirect method is used in the current research. Indirect methods can directly measure an aerosol but always a derivative property is measured and not the actual size. This complicates analyses of particle size distributions and prevents a direct comparison with the model. Therefore, data transformations are needed to convert the "raw" data to match the format of the model. A log-normal fit extracts the critical parameters: mode d_M , total concentration $N(t_R)$ and geometric standard deviation σ . Note, the mode is computed with the geometric mean size and σ [32]:

$$d_M = \exp(\ln d_g - \ln \sigma^2) \quad (6.3)$$

6.1.1. EXPERIMENTAL SET-UP

The experimental set-up is shown in Figure 6.2. Nanoparticles are produced in the VSP-G1 (A) and transported through a tube (B). The electrical mobility of charged particles in an electric field is measured by a Differential Mobility Analyser (DMA) (C).

The electric mobility is the velocity of a charged particle in an electric field of unit strength. The DMA is connected to a Faraway Cup (D), which detects charged particles by measuring the current. A flowbox (E) analyzes the data in terms of particle sizes. When this procedure is performed in scanning mode (by ramping the voltage and grouping the particle sizes in bins) the setup is called a Scanning Mobility Particle Sizer (SMPS).

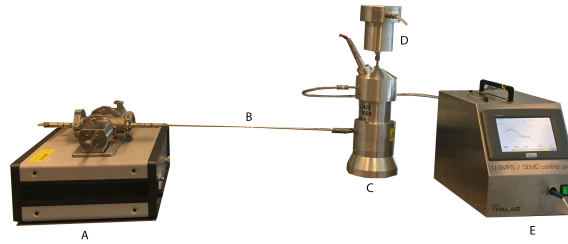


Figure 6.2: Experimental Set-Up. VSP-G1 (A), tube (B), SPMS (C-E)

Twenty experiments were conducted using gold electrodes and argon gas. The tube was extended right to the spark via an insert with the equivalent diameter to the tube $d_t = 0.4$ cm. The use of an insert minimizes the volume in the reactor chamber and reduces the possibility of turbulent flow. While the tube with length 9cm is fixed, the power P in [J/s] and flowrate Q in [lpm] were varied per experiment.

$$P = [1, 2.8, 5.4, 8.8, 13]$$

$$Q = [9, 7, 5, 3]^2$$

Unfortunately the VSP-G1 ran into some issues for most of the experiments with $Q = 5$ lpm, therefore all corresponding measurements are excluded from further analysis. This results in 15 usable empirical values for the mode, total concentration and geometric standard deviation (see Figure 6.1).

In parallel, mass measurements were performed to determine the ablation rate of gold electrodes under conditions applicable for this experimental set-up. Spark ablation causes a microscopic part of the electrode to vaporize into an aerosol. The ablation rate corresponds to the amount of material in [mol/J] and is defined as:

$$m_A = \frac{m_{el,loss} N_A}{m_m P}, \quad (6.4)$$

where $m_{el,loss}$ is the "ablated mass" in [g/s] and is quantified by weighing the electrodes after each experiment. Furthermore, m_m in [g] is the mass of one atom.

Note, for both the experiments and model, the inputs and results corresponding to all 15 experiments are listed in Appendix C.1.

²Note, the flow rate must be converted to [m³/s] before it can be inserted into Equation 6.1.

6.1.2. DATA CONVERSION

The SPMS produces raw data that requires a number of procedures to reconstruct the particle size distribution in the desired format. First, the electric mobility is converted to a particle diameter based on the mass dependence of the mobility. This affects the x-axis of the PSD. The data corresponding with the y-axis requires three steps. Then, the particle count per bin is normalized by dividing by the binsize, this ensures that each bin covers the same particle size range. Next, the particle concentration is calculated by taking into account the volumetric flow rate of the carrier gas. Finally, the total aerosol PSD (including non-charged particles) is reconstructed by applying Wiedensohlers' charge distribution[33].

X-CONVERSION

Measuring particles based on their electrical mobility is a common technique used in chemistry and aerosol science. It is based on charged particles that are subject to an electrical field that influence their orbits. Using Stokes law that calculates the drag force, the relation between the mobility and the particle diameter is given by the Millikan mode (standardized in ISO 15900): [34]

$$d = \frac{neC(\text{Kn})}{3\pi\eta Z} \quad (6.5)$$

where ne is the particle charge, $C(\text{Kn})$ is the Cunningham Slip Correction factor, η is the gas viscosity and Z the electrical mobility. These parameters depend on the gas type, the temperature and the pressure.

For small nanoparticles the diameter of the gas molecules d_g also plays a role, and by subtracted it from d , the diameter of the solid particle is defined:

$$d_p = d - d_g$$

The software used in this experiment converts the mobility to a particle size using argon as carrier gas. A scaling factor is used to compute the mobility diameter for other gasses as well:

$$d_p = \frac{C(\text{Kn})_{\text{Ar}} \cdot \eta_{\text{gas}}}{C(\text{Kn})_{\text{gas}} \cdot \eta_{\text{Ar}}} d - d_g \quad (6.6)$$

As explained in Section 2.5, agglomerates start to form for large residence times. This conversion uses the empirical relation between the agglomerate diameter d_{ag} and corresponding singlet diameter d_s [?]. The measured particle diameter of an agglomerate (hence let $d_p = d_{ag}$) is converted to a diameter corresponding to a sphere of the equivalent mass d_{cl} .

$$d_{cl} = \left(\frac{d_{ag}}{d_s^{1-F}} \right)^{1/F}$$

where F is a function of agglomerate diameter d_{ag} :

$$\begin{aligned} F &= (3/D_F - 1)(1 - e^{-(d_{ag}-d_s)}) + 1 & \text{for } d_{ag} > d_s \\ F &= 1 & \text{for } d_{ag} < d_s, \end{aligned}$$

where $D_F = 2.18$ holds for conditions applicable for the VSP-G1.

Y-CONVERSION

The charged particles enter the Faraday Cup and impact on a metal plate, causing a minuscule current. This current is measured and translated into a number of particles. After the counted particles are corrected per binsize $y_{\text{raw}}(d_p)$, they are converted to a concentration by dividing by the volumetric flow rate Q . Throughout the experiment, the flowrate through the DMA was kept fixed by using a critical orifice³ of 0.791 lpm. The preliminary result obtains a size distribution of only the charged particles.

³Critical orifice flow devices are used to maintain a constant flow rate under varying load conditions. [35]. During this experiment, the aerosol through the DMA maintains a constant flow rate of 0.791 lpm.

An empirical expression to convert a charged distribution to a total particle size distribution is derived by Wiedensohler [33]. The approximation formula for the charge distribution is:

$$f(ne) = 10^{\left[\sum_{i=0}^5 a_i(ne) \cdot \left(\log \frac{d_p}{nm} \right)^i \right]}, \quad (6.7)$$

where f is the percentage of particle size d_p that carry ne charge units⁴. For the current research the DMA was set to attract particles with charge $ne = +1$, which corresponds to the following coefficients:

a_0	a_1	a_2	a_3	a_4	a_5
-2.3484	0.6044	0.48	0.0013	-0.1553	0.0320

Table 6.1: Coefficients for a_i in Function 6.7

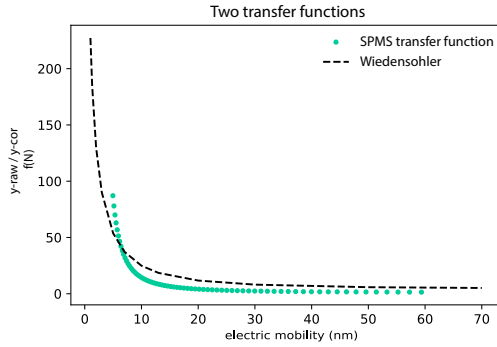


Figure 6.3: y-data transfer functions $f(ne)$

The SPMS has settings which make it possible to output a particle count that directly compensates for the uncharged particles, yielding so called "corrected data". The SPMS transfer function is initially unknown but is derived by dividing raw- by corrected data, it is plotted against Equation 6.7 in Figure 6.3 to test both functions. It is shown that both functions have the same trend, however differ enough in absolute values to proceed with caution.

This study uses Equation 6.7 with the coefficients in Table 6.1 to complete the y-conversion resulting in the concentration per particle diameter $N(d_p)$ in $[\text{cm}^{-3}]$:

$$N(d_p) = \frac{1}{Q} \frac{y_{\text{raw}}(d_p)}{f(1)} \quad (6.8)$$

Last, a Savitzky-Golay filter is applied to compensate for any unwanted noise from the Faraday cup. This is a digital filter for the purpose of smoothing data and is achieved by fitting successive sub-sets of adjacent data points with a low-degree polynomial by the method of linear least squares [?].

6.1.3. UNCERTAINTIES ON MEASUREMENTS

For proper empirical results, the experimental process shown on the left side of Figure 6.1 requires an accurate measuring system and a reliable data conversion method. Though both are well-thought out of, it is necessary to identify possible factors that could affect the accuracy of the measurements:

- The efficiency of the Faraway Cup, defined by the percentage of correctly counted charged particles, is unknown.
- The accuracy of the conversion from a charged particle concentration using Wiedensohler is questionable. Figure 6.3 shows two transfer functions. Applying either one could affect the concentration with as much as a factor two (especially for particles with lower mobility diameters).
- A high DMA measuring rate (a fast changing electrical field) may result in overlapping particle size measurements. Even though a slow DMA rate of three minutes is used for all measurements, overlaps in particle size measurements may still occur.

⁴In this approximation formula, ne corresponds to the charge unit of the measured particles and *not* the total particle concentration.

6.2. APPROXIMATION FORMULAS

The initial conditions for the model N_0 (6.1) and t_R (6.2) are approximated, not measured. The logical next step is to identify uncertainty factors that could induce deviations between the actual- and approximated values. These uncertainty factors are quantified by measuring fluctuations, making well-founded estimations and by mathematically analyzing the empirical data. Once quantified, it is possible to incorporate them in the model by calculating upper and lower bounds for each PSD parameter.

6.2.1. INITIAL CONCENTRATION

Recall the approximation function for the initial concentration:

$$N_0 = \frac{m_A N_A P}{Q}.$$

Various uncertainty factors on N_0 are identified here and analysed below.

- The ablation rate is computed by mass measurements and its corresponding standard deviation is transmitted to the uncertainty on N_0 .
- Power fluctuations are measured by the VSP-G1 and directly indicate a 15% possible deviation on N_0 .
- Based on previous experiments, other less quantifiable factors are estimated to have a combined deviation on N_0 of 5%.

ABLATION RATE

The approximation formula for N_0 states that the number of ablated atoms is linearly dependent on the power P . A previous mass experiment validates this assumption by showing a linear relation between the mass loss of the electrodes (ablated material) and the power of the VSP-G1.

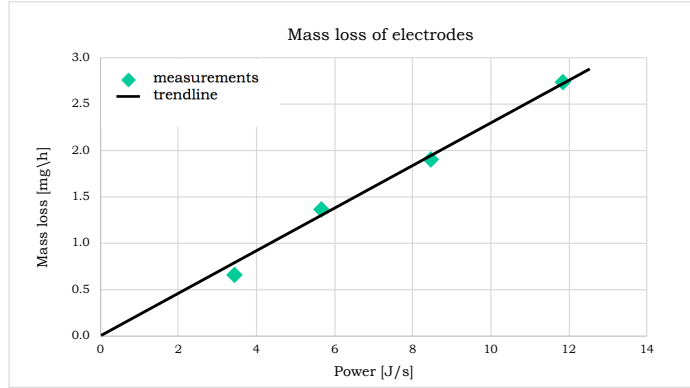


Figure 6.4: Hourly mass losses of gold electrodes for various power settings for $Q = 21 \text{ pm}$.

Recall the ablation rate:

$$m_A = \frac{m_{\text{el,loss}} N_a}{m_m P}$$

The expression for m_A suggests that the ablation rate is primarily power and material dependant. However, experiments suggests that the flowrate also plays an import role. Therefore, the current experiment measured mass losses for various flow rates. Since the linear dependence on the power was already proven, it was sufficient to conduct four mass measurements varying in flowrate but using a moreover constant power of $P \approx 5.5 \text{ J/s}$. The results turned out to fluctuate randomly with no direct relation to Q (see Table 6.2):

flow rate Q [lpm]	power P [J/s]	electrode mass loss [mg/h]	ablation rate [nmol/J]
9	6.03	2.4	0.561
7	5.09	1	0.277
5	5.50	0.9	0.231
3	5.20	3.5	0.950
average			0.504
standard deviation			0.33

Table 6.2: Results from mass measurements for varying flow rates using gold electrodes and argon gas.

It follows to use an ablation rate of $m_A = 0.504$ J/s in the validation process. Furthermore, its corresponding standard deviation is used to quantify the deviation of N_0 in Equation 6.1.

POWER

The power P in [J/s] is determined by the current I and the voltage V settings of the VSP-G1:

$$P = I \cdot V \quad (6.9)$$

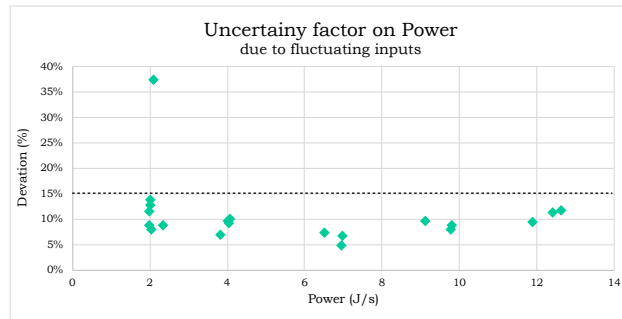


Figure 6.5: Standard Deviation of Power [%]

Both inputs are observed to be unstable sources. Measuring the fluctuations and using Equation 6.9 quantifies the deviation on N_0 . Figure 6.5 shows the measured power deviations in percentages. The majority is situated under 15%, independently of P . This has a direct affect on the initial concentration and it follows to take the same deviation on N_0 into account for further calculations.

OTHER UNCERTAINTIES

A less measurable factor of uncertainty is the deposition of particles onto surface areas inside the system that are not taken into account in the model. Examples of such areas are the electrode holders and the adapter between the G1 and the tube.

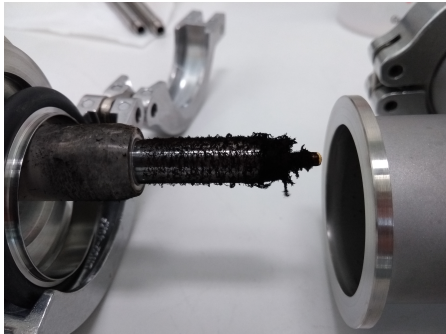


Figure 6.6: Deposition of particles on the electrode holder inside the G1

Note that for cross flow the diameter inside the reactor chamber is approximately 10 times larger than the tube diameter. This sudden change results in particles depositing and sticking onto the surface of the adapter and is analyzed in Appendix C.2. However, the current experiment uses an insert which minimizes this effect (explained in Section 6.1.1). Another deviation on N_0 could result from imprecise alignment of the electrodes after disassembling and reassembling the VSP-G1 in between experiments. A third possible effect is the temperature rise of the electrode, which is also expected to influence the ablation rate m_A . These three factors are estimated to ensure a merged maximum deviation of 5% on the initial concentration ⁵.

⁵Estimated in by VSPARTICLE engineers

6.2.2. RESIDENCE TIME

Throughout the experimental validation process, the residence time corresponds to the total duration of a particle inside the system, from spark to measuring moment. It is approximated by dividing the total volume, consisting of three main components (shown in Figure 6.7), by the flow rate Q .

$$t_R = \frac{V_1 + V_2 + V_3}{Q}, \quad (6.10)$$

where $V_1 = 0.9\text{cm}^3$ is the volume of the spherical area at the electrode gap, $V_2 = 1.13\text{cm}^3$ corresponds to the tube and insert dimensions, and $V_3 = 4\text{cm}^3$ is the estimated volume inside the DMA.

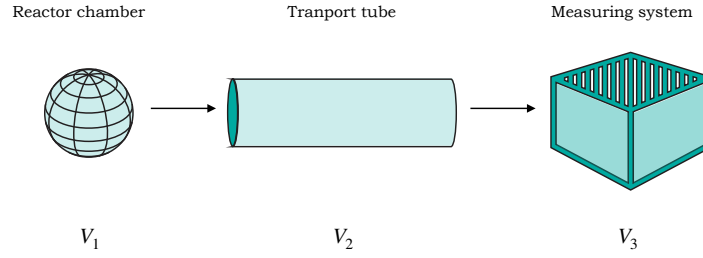


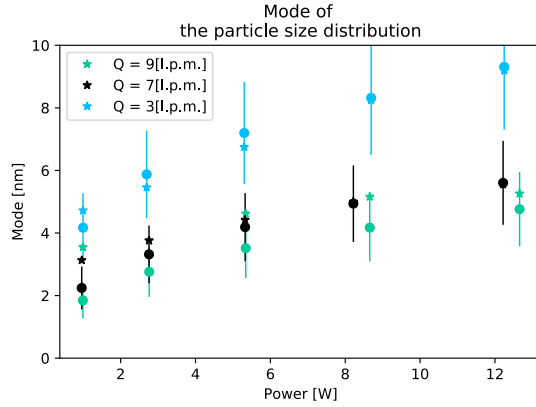
Figure 6.7: volume components relevant for the current validation process.

The residence time as approximated by Formula 6.10 could be underestimated for two reasons:

- The flow is assumed to be fully laminar while turbulent flow at the in and outlet of the tube can lead to an increase in t_R .
- According to [36], the exact value of V_3 is unknown but is somewhere in the range: $4 - 13\text{cm}^3$. The lower bound is taken in this study.

6.3. RESULTS

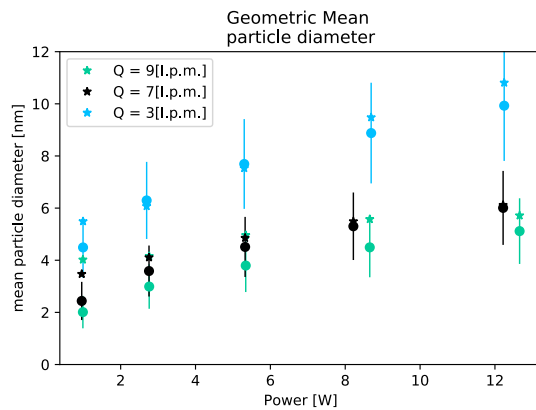
The experimental results are the mode, mean, total concentration and standard deviation of the particle size (stars) as a function of power and flow rate. These values are plotted against the modelled results (dots) computed with corresponding initial conditions. The upper and lower bounds on the modelled results are computed by taking uncertainty factors for N_0 into account. The observations are discussed with respect to physical phenomena of aerosol theory in Section 7.4.



(a)

Observations:

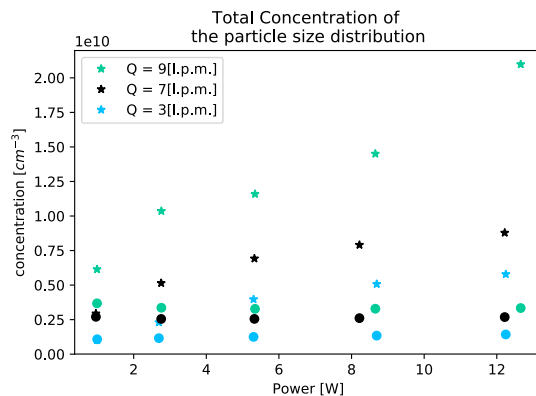
- Results agree within a range of 1 nm.
- Overall higher mode for lower flow rate.
- Overall higher mode for higher power rate.
- Better agreement of results for higher power rate.



(b)

Observations:

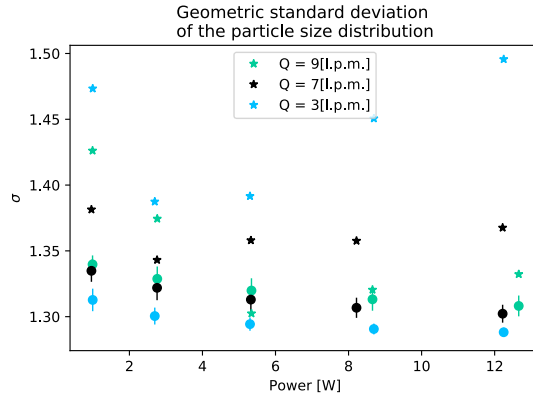
- Results agree within a range of 1 nm.
- Overall higher mean diameter for lower flow rate.
- Overall higher mean diameter for higher power rate.
- Range of best agreements varies with flowrate: where $P = 3 - 5$ [J/s] for lowest flow rate, and $P = 8 - 13$ [J/s] for higher flow rates.



(c)

Observations:

- Modelled values are consistently lower than experimental results with a factor ranging between 1.1 and 6.3.
- Better agreement for lower powers.
- Higher experimental total concentration for higher power.
- Modelled total concentration remains more or less constant regardless of power.
- Overall higher total concentration for higher flow rate.



(d)

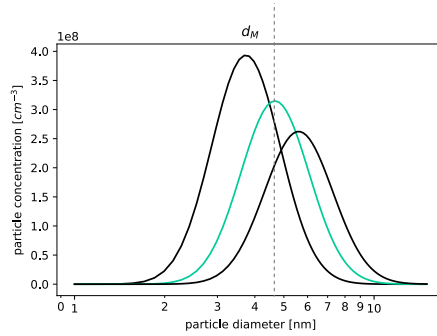
Figure 6.8: Modelled results (dots) vs. Experimental results (stars)

Observations:

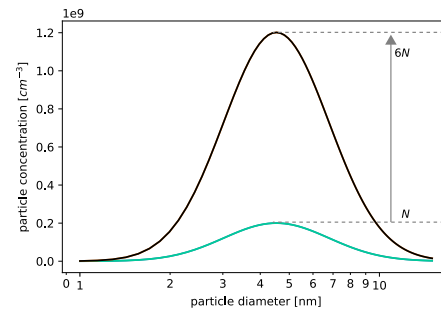
- The modelled results are consistently lower than experimental results.
- Higher modelled σ for higher flow rates
- Asymptotic behaviour of modelled sigma
- No direct relation between experimental sigma and flow rates.
- Decreasing experimental sigmas for $P = 1 - 5 \text{ [J/s]}$. Increasing experimental sigmas for $P = 6 - 13 \text{ [J/s]}$.

ACCURACY RANGES

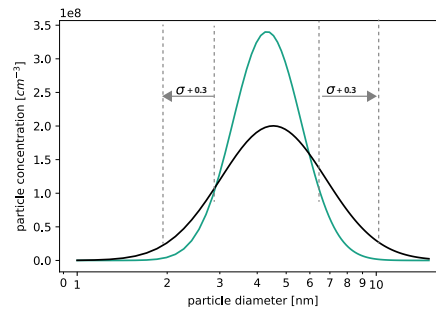
The results from the validation process provide accuracy ranges for the models approximation of the nanoparticles production in the VSP-G1, with respect to the particle size distribution. Overall, the mode is approximated at 1 nm accuracy, the measured total concentration is at most 6.3 times larger than computed by the model, and the geometric standard deviation is underestimated by a maximum of 0.3.



(a) Accuracy range for the mode



(b) Accuracy range for the concentration



(c) Accuracy range for geometric standard deviation

Figure 6.9: The model approximates the PSD of nanoparticles produced by the VSP-G1 within a certain range of accuracy.

6.4. AN IMPROVED FORMULA FOR THE MEAN PARTICLE SIZE

Hinds presented a function for the evolution the particle diameter increase for simple monodisperse coagulation [1]. Monodispersity implies that all particles have the same size.

$$d_{\text{coagulation}}(t) = d_0(1 + N_0 K t)^m, \quad (6.11)$$

where $m = 1/3$, d_0 is the initial particle diameter (i.e. atomic diameter), N_0 is the initial concentration and K is the coagulation coefficient which is defined by [1] for certain particle sizes and tabulated in Appendix C.3. Equation 6.11 is a simplified version of the simplest Smoluchowski equation in 2.1, neglecting diffusion. Recall, the model provides a more detailed definition for the coagulation frequency coefficient depending on the particle size, gas properties and regime (noted as β in Section 2.2).

Since the model approximates the particle diameter at nanometer accuracy throughout the validation process, it is interesting to compare Equation 6.11 with the modelled particle size evolution over time. Figure 6.10 shows a significant gap between $d_{\text{coagulation}}$ (" - -") defined by Hinds [1] and the modelled results (" -").

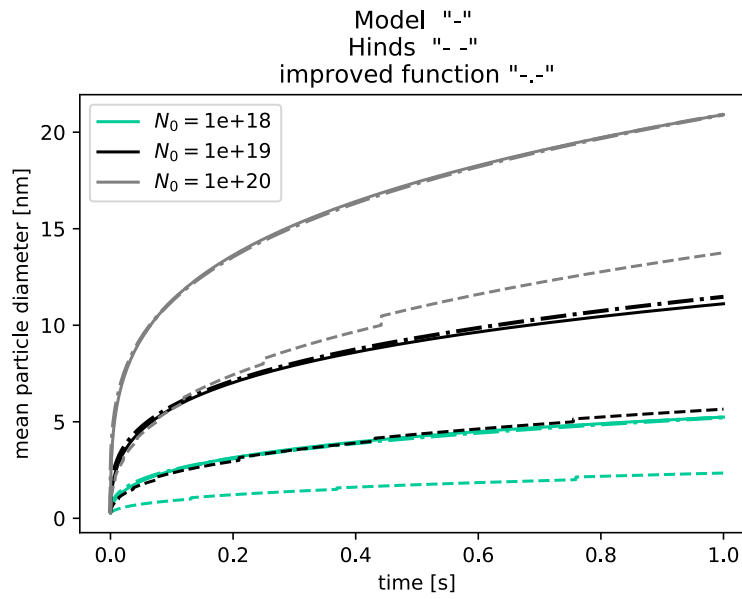


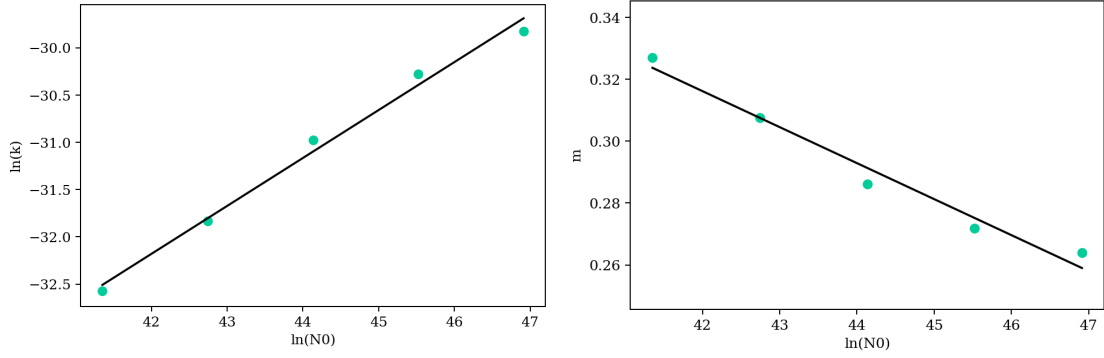
Figure 6.10: (Geometric mean) particle diameter computed by the model $d_g(t)$: "-", monodisperse coagulation defined by Hinds [1] $d(t)_{\text{coagulation}}$: "- -" and an improved function $d(t)_{\text{new}}$: "-.-". Note, sudden jumps occur in the results computed with Equation 6.11, these are due to the discrete values for K for a certain particle size range, tabulated in Appendix C.3.

A new, simple and improved formula for the evolution of the particle size is obtained by deviating the exponent m and the coagulation coefficient K in Equation 6.11 such that the corresponding particle diameter of the improved formula d_{new} fits the modelled geometric mean particle diameter d_g under equivalent circumstances. This is performed for various initial particle concentrations resulting in $\ln(N_0)$ -dependant fit-functions for the coefficients m and K , shown in Figure 6.11.

$$d_{\text{new}}(t) = d_0(1 + N_0 K t)^m \quad (6.12)$$

$$m = m_1 \ln(N_0) + m_2 \quad \begin{cases} m_1 = -0.011638365612901876 \\ m_2 = 0.80500871055215839 \end{cases} \quad (6.13)$$

$$K = k_1 N_0^{k_2} \quad \begin{cases} k_1 = 5.8653957138541767 \times 10^{-24} \\ k_2 = 0.50743367521464389 \end{cases} \quad (6.14)$$



(a) Fit function for coagulation coefficient K in $d(t)_{\text{new}}$. (b) Fit function for exponent coefficient m in $d(t)_{\text{new}}$.

Figure 6.11: Fit functions for coefficients m and K for the new formula for particle size increase due to coagulation over time.

Equation 6.12 is used to compute the particle size evolution for three initial conditions in Figure 6.10; $N_0 = 1 \times 10^{18}$ [atoms/m³] resembles the lowest possible concentration produced by the VSP-G1 while $N_0 = 1 \times 10^{20}$ [atoms/m³] corresponds to the largest. Both extremes show an excellent overlap for $d_{\text{new}}(t)$ ("--") and $d_g(t)$ ("-").

It concludes that the model's approximation for the evolution of the mean particle size can be computed with Equation 6.12. This is useful when a low computational time (< 1 sec) is required, mathematical simplicity is preferred, and the interest lies exclusively in the geometric mean particle size (rather than all properties of the PSD).

For a reversed approach, where the validation process is assumed to be sufficient and the model results are stated as accurate, Equation 6.12 with Coefficients 6.13 and 6.14 is seen as an improved function for the evolution of the particle size to that of Hinds [1].

7

DISCUSSION

This thesis obtained and validated a mathematical model that tracks the particle size distribution of aerosol produced by a nanoparticle generator that uses a technique called spark ablation. This chapter discusses certain assumptions, choices and results obtained throughout this thesis with respect to previous work in this field of research.

Section 7.1 highlights choices for mathematical equations describing nanoparticle growth, the implementation of the transition regime and the definition for the Cunningham Slip Correction factor. The motivation for applying the Method of Moments to obtain a solution for the Smoluchowski equation is discussed by comparing it with two other solution methods in Section 7.2. Next, the magnitude of numerical errors and errors due to uncertainty factors is discussed in Section 7.3. This chapter concludes by relating results obtained from the validation process with scientific knowledge of nanoparticle and aerosol physics.

7.1. CHOICES FOR MATHEMATICAL EQUATIONS

NANOPARTICLE GROWTH MECHANISMS

The original Smoluchowski equation was the first discrete governing equation for coagulation (1917) [17]. As of today, it has developed into a nonlinear partial differential equation including a great deal of aerosol mechanisms [17] (Appendix A.1). In this thesis, the model is based on Smoluchowski [3] and contains equations that mathematically define coagulation due to Brownian Motion and diffusion. In the development of a model, the most important mechanism is incorporated first. The choice to include coagulation was trivial because it acts as the main driving force for small particles ($< 1\mu\text{m}$) [8, 17, 27, 37, 38]. The runner-up was identified to be diffusion due to the massive particle deposition on surface areas inside the VSP-G1 observed in Figure 6.6. However, Section 5.3 showed that the impact of diffusion, as defined by [8], is almost negligible for VSP-G1 standard settings.

TRANSITION REGIME

Figure 2.2 in Section 2.2 shows that (gold) particles enter the transition regime when the particle diameter exceeds 5 nm, which corresponds with a Knudsen number equal to 28.12 for argon gas (Equation 2.3). This criteria was set in collaboration with VSPARTICLE engineers and is based on their experience with the generator and aerosol science in general. Various publications obtain different criteria for when the transition regime holds. Kodas [3] states that the transition regime applies for $1 < \text{Kn} < 50$ while according to Rader [4, 37] it is defined much lower: $0.4 < \text{Kn} < 20$. Even so, the location of the boundary is not incorporated into the model and therefore does not affect results. It is only identified after computations have been conducted as shown in Figures 5.3, 5.4b and 5.4d.

Dahneke's kernel was introduced in Section 2.2.3 and approached with the method of moments in Section 3.2.4. It enables the model to gradually shift from one limiting regime to the other, incorporating the transition regime. The implementation and affects of the transition regime were analyzed

in Section 5.2 and the theoretical validation in Figure 5.3 shows asymptotic behaviour of σ over time. An absolute difference in x-axis values is noticed between the results obtained by Lee et. al. [7] and the plot generated in this study, this due to the unknown scaling factors used by Lee et. al. to non-dimensionalize the moment functions. A similar analysis was conducted by [9] where the geometric standard deviation is a function of the Knudsen number instead of dimensionless time. The Knudsen number is dependent on the particle diameter which doesn't involve scaling. Not only will this lead to an improved validation of Dahneke's kernel, it will also provide better insights in particle sizes (or Knudsen numbers) in the transition regime.

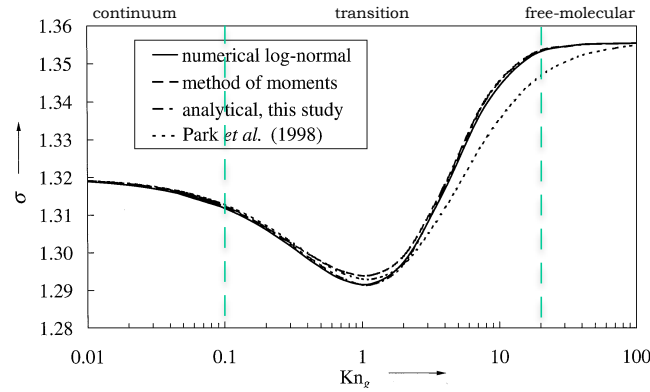


Figure 7.1: [9] analyzing the behaviour of σ as a function of Kn for various models. Regime boundaries were added by this thesis.

CUNNINGHAM SLIP CORRECTION FACTOR

Recall the Cunningham Slip Correction Factor introduced in Section 2.2.2:

$$C(Kn) = 1 + Kn \left(\alpha + \beta \exp(-\gamma/Kn) \right)$$

which accounts for non-continuum effects when the Knudsen number reaches its upper boundary: $Kn = 0.25$ [4, 18]. It is included in the continuum collision frequency kernel β_{Co} and diffusion term in Sections 2.2.2 and 2.3. The parameters were chosen according to [7–9] which sets $\gamma = 0$ and therefore excludes the natural logarithm from the equation.

Rader [4] conducted research on the Slip Correction Factor for small particles in nine common gasses, the corresponding parameters for the transition regime are tabulated in Appendix A.2. Excluding the natural logarithm does not hold for values obtained by Rader. Applying the method of moments for the Smoluchowski equation using Raders parameters for $C(Kn)$ would result in different moment functions h_k and l_k (See Section 3.2).

The diffusion coefficient $D(r)$ in the sink term is a function of $C(Kn)$ (See Equation 2.15). Appendix C.2.3 compares $D(r)$ where the Slip Correction Factor is interpreted by Rader versus Lee et. al.. Though no sufficient deviation is observed here, it is also interesting to adjust the coagulation equations to fit Raders parameters and study the new results.

7.2. SOLUTION METHOD

The method of moments is used to obtain a solution for the Smoluchowski equation. However, [17] presents two other methods to solve the Smoluchowski equation which are worth investigating.

SECTIONAL METHOD

The sectional method solves the Smoluchowski Equation at every interval in terms of timestep, particle size and spacial location [23] and can therefore be applied to the extended Smoluchowski equation presented in Equation A.1. The solution is obtained using numerical discretization methods such as Runge Kutta to approximate the Smoluchowski integrals. A finite element scheme can be applied for

the spacial coordinate of the transport equation [38]. The sectional method is used to study the evolution of the PSD over time [23], and generates the most detailed outcome. However, the massive increase in computational costs make it quite impractical [17].

Monte Carlo Method

A stochastic particles approach is the other alternative for mathematically modelling of nanoparticle growth. This method allows coagulation of two particles to occur with a certain probability and contains various algorithms; the direct simulation algorithm (DSA) and the mass flow algorithm (MFA) are the most popular [39], [40]. The stochastic particles approach or, *Monte Carlo method*, allows the PSD to fully be determined along with the moments of the distribution. Also, it has proven to be computationally less expensive compared to the sectional method [40]. A draw back is that the derivation of a stochastic coagulation model is mathematically complex and requires a thorough understanding of probability theory. Moreover, the incorporation of computational fluid dynamics (CFD) is still limited [17].

Motivation for the Method of Moments

The Method of Moments is described in detail in Chapter 3. The computational expense of the sectional method, and the complexity and limits of Monte Carlo are non-existent in the Method of Moments. Although the original MoM is unable to trace the evolution of the particle size distribution, the log-normal MoM overcomes this by reconstructing the PSD from a log-normal distribution.

7.3. ERROR ANALYSIS

Chapter 4 motivated the use of the Forward Euler numerical method to approximate a solution for the moment equations. Recall that the Forward Euler is the simplest method obtaining a relatively high order error. Applying a numerical method with a lower order of error seems as a logical next step to improve model accuracy. However, the uncertainty factors presented in Sections 6.1.2 and 6.2 result in error ranges that are much larger than any numerical error due to Forward Euler. Adjusting the models framework and approximation formulas in Section 6.2 is needed to obtain a better compliance with experimental results and therefore has a higher priority.

7.4. EXPERIMENTAL RESULTS

Figure 6.8 shows the experimental and modelled results for the mode, geometric mean particle size, total concentration and the geometric standard deviation of the PSD for varying VSP-G1 settings in terms of power and flow rate. These results and observations are discussed and related to aerosol theory, measurement uncertainties and the approximation formulas for the initial conditions:

$$N_0 = \frac{m_A N_a P}{Q},$$

$$t_R = \frac{V}{Q}.$$

Aerosol Theory

Overall, a higher mode and mean particle diameter is observed for increasing powers and decreasing flow rates (see Figures 6.8a and 6.8b). These settings imply a high initial concentration and a long residence time, which increases the chance of particle collisions over a relatively long period of time. This leads to an increase in mean particle size which is proportionate to the mode by Equation 6.3. This relation is visualized in Figure 7.2.

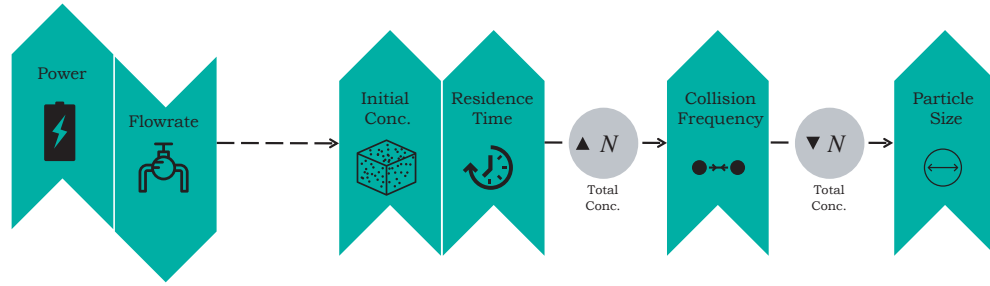


Figure 7.2: A flowchart visualizing the relation between VSP-G1 inputs, model inputs, total concentration and particle size.

The high experimental total concentrations for increasing power settings in Figure 6.8c is directly related to the linear dependence of the ablation rate to power (Figure 6.4). Also, higher flow rates imply lower residence times i.e. shorter coagulation times resulting in higher concentrations. The model however, shows asymptotic behaviour for the total concentration which is a characterizing property of the population balance equation for coagulation due to Brownian Motion. This implies that coagulation overrules diffusion, complying with observations in Section 5.3.

Moreover, the model assumes coagulation in a closed space which induces the asymptotic behaviour of σ observed in Figure 6.8d. The geometric standard deviation approaches its self-preserving value for lower flow rates, i.e. longer residence times. The measured values for σ are consistently higher than the modelled results. This is likely due to the aerosol being exposed to other mechanisms which are neglected by the model, such as the fact that the tube is open and coagulation does not actually occur in a closed space.

UNRELIABLE PARTICLE CHARGE TRANSFER FUNCTION

The second uncertainty factor described in Section 6.1.3 regards the charge transfer function displayed in Figure 6.3. Notice that a miss-measurement in the electric mobility implies a large deviation in the charged particle fraction due to its exponential behaviour for small particles. This affects the reliability of all experimental results and explains the deviation in total concentration in particular (Figure 6.8c).

8

CONCLUSIONS

The advancement of nanotechnology relies on the actual production, control and integration of nanoparticles. VSPARTICLE developed a generator, the VSP-G1, which produces nanoparticles with a gas-phase technique called spark ablation. The objective of this thesis was to develop a computational model that simulates the nanoparticle production and obtains the particle size distribution of the aerosol throughout the process. Recall the research goal:

Develop a numerical and computationally efficient model of the nanoparticle growth from spark ablation in the gas phase.

This goal is met through the development of a numerical model that tracks the nanoparticle growth at nanometer accuracy within an acceptable computational time. This was achieved by identifying the physical framework of the model, defining mathematical equations, and using the method of moments to obtain the particle size distribution for a certain initial concentration and residence time. A theoretical and experimental validation proved a sufficient accuracy of the model with respect to nanoparticle growth in the VSP-G1.

The computational model will provide researchers with an analysis regarding the sensitivity of the input parameters. The framework of the model consisting of mathematical and physical processes, will provide a better scientific understanding of the system. Finally, the model can be used as operational guide to produce pure, tailor-made nanoparticles.

NEW CONTRIBUTIONS

Lee et. al. [9] presented an analytical solution for the log-normal size distribution of pure Brownian aerosol coagulation for the entire particle size regime. Lee and Gieseke [9] obtained an expression for particle decay in aerosol transported through a circular tube as a function of tube length. This thesis combines these results and presents a numerical solution for the log-normal size distribution of Brownian aerosol coagulation and diffusion for the entire particle size regime.

The numerical approach for coagulation starts by deriving ordinary differential equations using the MoM for the limiting regimes: free molecular and continuum. The entire particle regime is approached by inserting these ODEs into Dahneke's Kernel, and by expressing the molecular-free dimensionless timestep τ_F , in terms of the dimensionless timestep of the continuum regime τ_{Co} (See Section 3.2.4 in particular).

Furthermore, the diffusion term for aerosol was analyzed apart from coagulation by Lee and Gieseke in [8] in 1980. The expression for particle decay as a function of a spacial coordinate is rewritten to be time-dependent and converted to a set of ordinary differential equations by applying the MoM (See Sections 2.3 and 3.2.5).

The moment equations describing coagulation and diffusion are joined to form one set of ODEs and solved using the Forward Euler numerical method. The solution provides the particle size distribution of an aerosol which is exposed to coagulation and diffusion over time.

RECOMMENDATIONS

The model is able to compute particle growth for any material and gas. However, it has only been experimentally validated with gold electrodes and argon carrier gas. For an all-round reliable model, it is necessary to repeat the validation process described in Chapter 6 with other materials and gasses.

Moreover, the same argument applies for the flowtype. While an insert is used in this research, the depositing particles in Figure 6.6 are observed for cross- and through flow. This effect is not incorporated into the model. Quantifying it is necessary to obtain accurate results for all flow types.

The validation process will greatly improve when using particle counting systems that have a higher accuracy and reliability, such as a condensation particle counter (CPC). This method counts all particles, excluding the use of a charge distribution in the experimental data conversion (Section 6.1.2). Also, quantifying the other uncertainty factors will provide accuracy ranges with a higher reliability (presented in Section 6.3).

Besides Brownian Motion, coagulation of nanoparticles occurs due to thermophoresis, inter-particle varying velocities and van der Waals forces. Taking one step back, besides coagulation and diffusion, other dynamic processes also influence the composition of aerosol such as condensation and turbulence. Before extending the model, these mechanisms should be evaluated on importance for the nanoparticle growth process. After a sufficient mechanism is identified, it should be incorporated into the model by applying the method of moments.

BIBLIOGRAPHY

- [1] W. C. Hinds, *Aerosol technology: Properties, Behavior and Measurement of Airborne Particles*. (1999).
- [2] P. Tunved, *An introduction to crossbow hunting*, University Lecture (2000).
- [3] T. Kudas and M. Hampden-Smith, *Aerosol Processing of Materials* (Wiley, 1999).
- [4] D. J. Rader, *Momentum slip correction factor for small particles in nine common gases*, Journal of Aerosol Science **21**, 161 (1990).
- [5] Kaye and Laby, *Tables of physical chemical constants*, (1995).
- [6] K. W. Lee, J. Chen, and J. A. Gieseke, *Log-normally preserving size distribution for brownian coagulation in the free-molecule regime*, Aerosol Science and Technology **3**, 53 (1984), <https://doi.org/10.1080/02786828408958993>.
- [7] S. Park, K. Lee, E. Otto, and H. Fissan, *The log-normal size distribution theory of brownian aerosol coagulation for the entire particle size range: Part i—analytical solution using the harmonic mean coagulation kernel*, Journal of Aerosol Science **30**, 3 (1999).
- [8] K. Lee and J. Gieseke, *Simplified calculation of aerosol penetration through channels and tubes*, Atmospheric Environment (1967) **14**, 1089 (1980).
- [9] E. Otto, H. Fissan, S. Park, and K. Lee, *The log-normal size distribution theory of brownian aerosol coagulation for the entire particle size range: part ii—analytical solution using dahneke's coagulation kernel*, Journal of Aerosol Science **30**, 17 (1999).
- [10] M. Ananya Mandal, *Properties of nanoparticles*, (2018).
- [11] S.-A. Products, *Gold nanoparticles: Properties and applications*, (2018).
- [12] D. L. Chandler, *A material for all seasons*, (2009).
- [13] A. McWilliams, *The maturing nanotechnology market: Products and applications*, (2016).
- [14] M. Boeije, *Influencing the nanoparticle generation and deposition process*, (2018).
- [15] J. Feng, G. Biskos, and A. Schmidt-Ott, *Toward industrial scale synthesis of ultrapure singlet nanoparticles with controllable sizes in a continuous gas-phase process*, in *Scientific reports* (2015).
- [16] D. L. Glenn Marion, *An introduction to mathematical modelling*, (2008).
- [17] M. Yu and L. Yueyan, *Methods of moments for resolving aerosol dynamics*, in *Aerosols - Science and Case Studies*, edited by K. Volkov (InTech, Rijeka, 2016) Chap. 02.
- [18] R. N. Sinn, *Dekker Encyclopedia on nanoscience and nanotechnology*, edited by J. A. S. C. I. C. K. Putyera, Vol. 1 A-C 1-892 (Marcel Dekker, Inc., 2004) pp. 36–38.
- [19] T. Trzeciak, *Brownian Coagulation at High Particle Concentrations.*, Ph.D. thesis, Delft University of Technology (2012).
- [20] P.-I. Au, J. Liu, and Y.-K. Leong, *Yield stress and microstructure of washed oxide suspensions at the isoelectric point: experimental and model fractal structure*, Rheologica Acta **55**, 847 (2016).
- [21] A. Schmidt-Ott, *New approaches to in situ characterization of ultrafine agglomerates*, Journal of Aerosol Science **19**, 553 (1988).

- [22] E. Newman and K. Kingsley, *An introduction to the method of moments*, Computer Physics Communications **68**, 1 (1991).
- [23] P. R. Estrada and J. N. Cuzzi, *Solving the coagulation equation by the moments method*, The Astrophysical Journal **682**, 515 (2008).
- [24] G. C. Razvan Tamas, Ana Dumitrascu, *Alternative applications of the method of moments: from electromagnetic waves to source synthesis, deconvolution, and data processing in navigation systems*, (2015).
- [25] M. Yu, J. Lin, and T. Chan, *A new moment method for solving the coagulation equation for particles in brownian motion*, Aerosol Science and Technology **42**, 705 (2008), <https://doi.org/10.1080/02786820802232972>.
- [26] M. Kraft, *Modelling of particulate processes*, KONA Powder and Particle Journal **23**, 18 (2005).
- [27] M. Yamamoto, *A moment method of the log-normal size distribution with the critical size limit in the free-molecular regime*, Aerosol Science and Technology **48**, 725 (2014), <https://doi.org/10.1080/02786826.2014.922161>.
- [28] M. Frenklach and S. J. Harris, *Aerosol dynamics modeling using the method of moments*, Journal of Colloid and Interface Science **118**, 252 (1987).
- [29] K. W. Lee and H. Chen, *Coagulation rate of polydisperse particles*, Aerosol Science and Technology **3**, 327 (1984), <https://doi.org/10.1080/02786828408959020>.
- [30] C. Vuik, F. Vermolen, M. Gijzen, and M. Vuik, *Numerical Methods for Ordinary Differential Equations* (DAP, Delft Academic Press, 2015).
- [31] D. J. Carstensen and D. J.-M. Wagner, *University of kiel, lecture notes: Advanced mathematics – computer mathematics*, (2018), uRL: https://www.tf.uni-kiel.de/matwis/amat/comp_math/index.html.
- [32] R. Grainger, *Some Useful FORMulae for Aerosol Size Distributions and Optical Properties*, (2017).
- [33] A. Wiedensohler, *An approximation of the bipolar charge distribution for particles in the submicron size range*, Journal of Aerosol Science **19**, 387 (1988).
- [34] *A NOMETER SCALE PARTICULATE DEFINING PARTICLE DIAMETER* (2016).
- [35] N. J. ZIMMERMAN and P. C. REIST, *The critical orifice revisited: A novel low pressure drop critical orifice*, American Industrial Hygiene Association Journal **45**, 340 (1984), PMID: 6234789, <https://doi.org/10.1080/15298668491399893>.
- [36] *Electrostatic classifier model 3082. Scanning mobility particle sizer spectrometer model 3938.*
- [37] *Kinetic Theory of Granular Gases.*
- [38] R. R. Zagidullin, A. P. Smirnov, S. A. Matveev, and E. E. Tyrtysnikov, *An efficient numerical method for a mathematical model of a transport of coagulating particles*, Moscow University Computational Mathematics and Cybernetics **41**, 179 (2017).
- [39] V. Smorodin, *Revising the fuchs “boundary sphere” method*. Wagner P.E. (eds) Nucleation and Atmospheric Aerosols (2007).
- [40] N. Morgan, *Numerical Modelling of the Growth of Nanoparticles*, Ph.D. thesis, University of Cambridge (2007).

A

MODEL FRAMEWORK MATHEMATICAL EQUATIONS

A.1. SMOLUCHOWSKI

The extended Smoluchowski equation accounts for almost all aerosol dynamics including external mechanisms due to aerosol transport through air [17], which introduces the spatial coordinate x , and incorporates the Navier-Stokes equation:

$$\begin{aligned}
 & \frac{\partial n(v, x, t)}{\partial t} + \frac{\partial(un(v, x, t))}{\partial x} + \frac{\partial(u_{th}n(v, x, t))}{\partial x} \\
 &= \frac{\partial}{\partial x} \left(D_B \frac{\partial n(v, y, t)}{\partial x} \right) + \frac{\partial(G_r n(v, x, t))}{\partial v} + J(v^*, x, t)\delta(v - v^*) \\
 & - \frac{1}{2} \int_{v^*}^v \beta(v', v - v', t) n(v', x, t) n(v - v', t) dv' \\
 & - n(v) \int_{v^*}^{\infty} \beta(v, v', t) n(v', x, t) dv' + \int_v^{\infty} a(v') b(v|v') n(v', t) dv' \\
 & - a(v) n(v, t) + \dots
 \end{aligned} \tag{A.1}$$

where $n(v, x, t)$ is the particle number density for particle volume v , spatial coordinate x , and time t ; the value β represents the collision frequency; u is the particle velocity, u_{th} is the velocity of particles in response the change in temperature; D_B is the Brownian diffusion coefficient; G_r is the particle surface growth rate; J is the source term, i.e. the nucleation rate of atomic-sized particles v^* ; a and b are parameters accounting for the breakage of (non)-spherical particles due to shear force along the walls of the tube. [17].

A.2. CUNNINGHAM FREQUENCY CONSTANT

Rader [4] obtained different values for the parameters used in the Cunningham Slip Correction Factor in the transition regime. Recall:

$$C(Kn) = 1 + Kn \left(\alpha + \beta \exp(-\gamma/Kn) \right)$$

Parameters	Argon	Nitrogen	Air
α	1.227	$1.207 \pm 5\%$	1.207
β	0.42	$0.40 \pm 5\%$	0.40
γ	0.85	$0.78 \pm 5\%$	0.78

Table A.1: Parameters for Cunningham Slip Correction factor for different gasses in the transition regime according to [4] under standard conditions: $T_0 = 296.15$ K; $P_0 = 101.325$ kPa

B

SOLUTION METHOD

B.1. OVERVIEW OF FUNCTIONS IN MODEL EQUATION

The model solves the following dimensionless, nonlinear ordinary differential equation for $k = 0$, $k = 1$, and $k = 2$:

$$\frac{\widetilde{M}_k}{d\tau} = \tilde{g}_k \left[\frac{1 + \tilde{B}(\tau_{Co}) \frac{\tilde{g}_k}{2h_k}}{1 + a(\sigma) \tilde{B}(\tau_{Co}) \frac{\tilde{g}_k}{2h_k} + 2 \left(\tilde{B}(\tau_{Co}) \frac{\tilde{g}_k}{2h_k} \right)^2} \right] + \tilde{l}_k, \quad (B.1)$$

Where:

$$\begin{aligned} \tilde{g}_0 = & - \left(\widetilde{M}_0^{\frac{151}{72}} \widetilde{M}_1^{-\frac{13}{36}} \widetilde{M}_2^{\frac{19}{72}} \exp\left(\frac{25}{8} \ln^2 \sigma_0\right) \dots \right. \\ & \dots + 2 \widetilde{M}_0^{\frac{131}{72}} \widetilde{M}_1^{\frac{7}{36}} \widetilde{M}_2^{-\frac{1}{72}} \exp\left(\frac{5}{8} \ln^2 \sigma_0\right) \dots \\ & \left. \dots + \widetilde{M}_0^{\frac{127}{72}} \widetilde{M}_1^{\frac{11}{36}} \widetilde{M}_2^{-\frac{5}{72}} \exp\left(\frac{1}{8} \ln^2 \sigma_0\right) \right) \end{aligned}$$

$$\tilde{g}_1 = 0$$

$$\begin{aligned} \tilde{g}_2 = & 2 \left(\widetilde{M}_0^{\frac{19}{72}} \widetilde{M}_1^{\frac{47}{36}} \widetilde{M}_2^{\frac{31}{72}} \exp\left(\frac{109}{8} \ln^2 \sigma_0\right) \dots \right. \\ & \dots + 2 \widetilde{M}_0^{-\frac{7}{72}} \widetilde{M}_1^{\frac{67}{36}} \widetilde{M}_2^{\frac{11}{72}} \exp\left(\frac{89}{8} \ln^2 \sigma_0\right) \dots \\ & \left. \dots + \widetilde{M}_0^{-\frac{5}{72}} \widetilde{M}_1^{\frac{71}{36}} \widetilde{M}_2^{\frac{7}{72}} \exp\left(\frac{85}{8} \ln^2 \sigma_0\right) \right) / \exp(18 \ln^2 \sigma_0) \end{aligned}$$

$$\begin{aligned} \tilde{h}_0 = & - \left(\widetilde{M}_0^2 + \widetilde{M}_0^{\frac{19}{9}} \widetilde{M}_1^{-\frac{2}{9}} \widetilde{M}_2^{\frac{1}{9}} \exp(\ln^2 \sigma_0) \dots \right. \\ & \left. \dots + \tilde{A} \left(\widetilde{M}_0^{\frac{23}{9}} \widetilde{M}_1^{-\frac{7}{9}} \widetilde{M}_2^{\frac{2}{9}} \exp\left(\frac{1}{2} \ln^2 \sigma_0\right) + \widetilde{M}_0^{\frac{25}{9}} \widetilde{M}_1^{-\frac{11}{9}} \widetilde{M}_2^{\frac{4}{9}} \exp\left(\frac{5}{2} \ln^2 \sigma_0\right) \right) \right) \end{aligned}$$

$$\tilde{h}_1 = 0$$

$$\begin{aligned} \tilde{h}_2 = & 2 \left(\exp(9 \ln^2 \sigma_0) + \widetilde{M}_0^{\frac{1}{9}} \widetilde{M}_1^{\frac{16}{9}} \widetilde{M}_2^{\frac{1}{9}} \exp(10 \ln^2 \sigma_0) \dots \right. \\ & \left. \dots + \tilde{A} \left(\widetilde{M}_0^{\frac{2}{9}} \widetilde{M}_1^{\frac{1}{9}} \widetilde{M}_2^{-\frac{1}{9}} \exp\left(\frac{13}{2} \ln^2 \sigma_0\right) + \widetilde{M}_0^{\frac{4}{9}} \widetilde{M}_1^{\frac{13}{9}} \widetilde{M}_2^{\frac{1}{9}} \exp\left(\frac{17}{2} \ln^2 \sigma_0\right) \right) \right) / \exp(18 \ln^2 \sigma_0) \end{aligned}$$

$$\begin{aligned} \tilde{l}_0 = & - \frac{1.67}{N_0 R_t^2 \pi} \left(\widetilde{M}_0^{\frac{14}{9}} \widetilde{M}_1^{-\frac{7}{9}} \widetilde{M}_2^{\frac{2}{9}} \nu_{g0}^{-\frac{1}{3}} \exp\left(\frac{1}{2} \ln^2 \sigma_0\right) \dots \right. \\ & \left. \dots + 2.67 \lambda \widetilde{M}_0^{\frac{20}{9}} \widetilde{M}_1^{-\frac{16}{9}} \widetilde{M}_2^{\frac{5}{9}} \nu_{g0}^{-\frac{2}{3}} \exp(2 \ln^2 \sigma_0) \right) \end{aligned}$$

$$\begin{aligned}
\tilde{l}_1 = & -\frac{1.67}{N_0 R_t^2 \pi} \left(\tilde{M}_0^{\frac{20}{9}} \tilde{M}_1^{-\frac{16}{9}} \tilde{M}_2^{\frac{5}{9}} \nu_{g0}^{-\frac{1}{3}} \exp(2 \ln^2 \sigma_0) \dots \right. \\
& \left. \dots + 2.67 \lambda \tilde{M}_0^{\frac{5}{9}} \tilde{M}_1^{\frac{5}{9}} \tilde{M}_2^{-\frac{1}{9}} \nu_{g0}^{-\frac{2}{3}} \exp\left(\frac{1}{2} \ln^2 \sigma_0\right) \right) / \exp\left(\frac{9}{2} \ln^2 \sigma_0\right) \\
\tilde{l}_2 = & -\frac{1.67}{N_0 R_t^2 \pi} \left(\tilde{M}_0^{-\frac{1}{9}} \tilde{M}_1^{\frac{5}{9}} \tilde{M}_2^{\frac{5}{9}} \nu_{g0}^{-\frac{1}{3}} \exp\left(\frac{25}{2} \ln^2 \sigma_0\right) \dots \right. \\
& \left. \dots + 2.67 \lambda \tilde{M}_0^{-\frac{1}{9}} \tilde{M}_1^{\frac{8}{9}} \tilde{M}_2^{\frac{2}{9}} \nu_{g0}^{-\frac{2}{3}} \exp(8 \ln^2 \sigma_0) \right) / \exp(18 \ln^2 \sigma_0)
\end{aligned}$$

$$\begin{aligned}
\tilde{B}(\tau) = & \frac{d\tau}{d\tau_F B(\tau)} = \frac{d\tau}{d\tau_F} \left(1 + 1.2 \exp(-2\sigma(\tau)) - 0.646 \exp(-0.35\sigma(\tau)^2) \right) \\
\tau = & N_0 K_{Co} t, \quad \tau_F = N_0 \nu_{g0}^{1/6} K_F t \\
\tilde{A} = & A \lambda \left(\frac{4}{3} \pi \right)^{1/3} \frac{1}{\sqrt[3]{\nu_{g0}}}
\end{aligned}$$

\tilde{g}_k is a function describing the time-derivative of the k^{th} -moment in the free molecular regime, \tilde{g}_k is the equivalent but then for the continuum regime, and \tilde{l}_k accounts for the diffusion effects on moment k .

$\tilde{B}(\tau)$ is a collected function that prevents non-linearity in \tilde{g}_k and converts $\tau_F \Rightarrow \tau_{Co}$.

τ is the dimensionless time used in this thesis, while τ_F it the definition for dimensionless time when only solving for Brownian coagulation in the free-molecular regime.

\tilde{A} is a dimensionless constant used in \tilde{h}_k , where λ is the mean free path of the gas and ν_{g0} is the initial volume of the solid particle.

Lastly, N_0 is the initial concentration and σ is the geometric standard deviation with initial value σ_0 . R_t is the tube radius, K_{Co} the collision constant for the continuum regime, K_F the collision constant for the free-molecular regime, and t is time.

C

EXPERIMENTAL RESULTS

C.1. EXPERIMENTAL AND MODELLED RESULTS

	Experimental Input		Model Input		Output parameters			
validation experiment	$P[\text{J/s}]$	$Q[\text{lpm}]$	$N_0[\text{m}^{-3}]$	$t_R[\text{ms}]$	$d_M[\text{nm}]$	$d_g[\text{nm}]$	$N(t_R)[\text{m}^{-3}]$	σ
1	1	9	2.02×10^{18}	26.8	1.80	2.01	3.68×10^{15}	1.34
2	2.8	9	5.67×10^{18}	26.8	2.76	2.99	3.36×10^{15}	1.33
3	5.4	9	1.09×10^{19}	26.8	3.51	3.79	3.28×10^{15}	1.32
4	8.8	9	1.78×10^{19}	26.8	4.17	4.49	3.29×10^{15}	1.31
5	13	9	2.63×10^{19}	26.8	4.76	5.12	3.34×10^{15}	1.31
6	1	7	2.60×10^{18}	34.5	2.24	2.43	2.70×10^{15}	1.33
7	2.8	7	7.29×10^{18}	34.5	3.21	3.58	2.55×10^{15}	1.32
8	5.4	7	1.41×10^{19}	34.5	4.19	4.51	2.55×10^{15}	1.31
9	8.8	7	2.29×10^{19}	34.5	4.93	5.30	2.61×10^{15}	1.31
10	13	7	3.38×10^{19}	34.5	5.60	6.00	2.69×10^{15}	1.30
11	1	3	6.08×10^{18}	80.1	4.17	4.49	1.08×10^{15}	1.31
12	2.8	3	1.70×10^{19}	80.1	5.87	6.24	1.16×10^{15}	1.3
13	5.4	3	3.28×10^{19}	80.1	7.20	7.69	1.25×10^{15}	1.29
14	8.8	3	5.35×10^{19}	80.1	8.32	8.87	1.34×10^{15}	1.29
15	13	3	7.90×10^{19}	80.1	9.31	9.93	1.43×10^{15}	1.29

Table C.1: Results corresponding to the validation process described in Chapter 6. Material = gold, gas = argon, flowtype = insert, tube length = 9 cm, ablation rate = 0.504 [nmol/J].

C.2. QUANTIFYING DEPOSITION FOR CROSSFLOW

Four mass measurement experiments were conducted using filters to collect the output at the end of the transport tube. The model is run with corresponding initial conditions, defined by the settings of each experiment. The computed nanoparticle concentration to leave the end of the tube is converted to a mass and compared to the actual mass gain in the filter. The sink term in the model is accurate if these values comply.

C.2.1. EXPERIMENTAL SET-UP

Gold electrodes were ablated by the VSP-G1 using 3 lpm argon crossflow. At a distance of 16 cm from the spark the particles were collected by a filter. Four experiments were performed with the power as only variable, this influences the initial concentration, not the residence time.

INITIAL CONCENTRATION

Just as in Section 6.1.1, the initial concentration was determined by the electrode mass loss after each experiment. However, the ablation rate was skipped here and N_0 was directly computed from the electrode mass loss.

$$N_0 = \frac{m_{\text{el, loss}}}{m_m} \frac{\text{Na}}{Q},$$

where $m_{\text{el, loss}}$ is the mass loss of the electrodes in [mg/h], m_m is the molar mass of the electrode material, Na is Avogadro's number, and Q is the volumetric flowrate.

MASS OUTPUT

The nanoparticles in the filter formulate the experimental mass output $m_{\text{e,output}}$. If it is comparable with the mass output computed by the model the sink term is accurately approximates the diffusion impact in the system.

$$m_{\text{e,output}} \stackrel{?}{=} m_{\text{m,output}} = \frac{m_m}{\text{Na}} \frac{M_1(t_R)}{v_{g0}} Q \quad (\text{C.1})$$

where $M_1(t_R)$ is the total particle volume at time t_R , and v_{g0} is the initial particle volume (equivalent to the atomic volume). Figure C.1 is a schematic overview of the process.

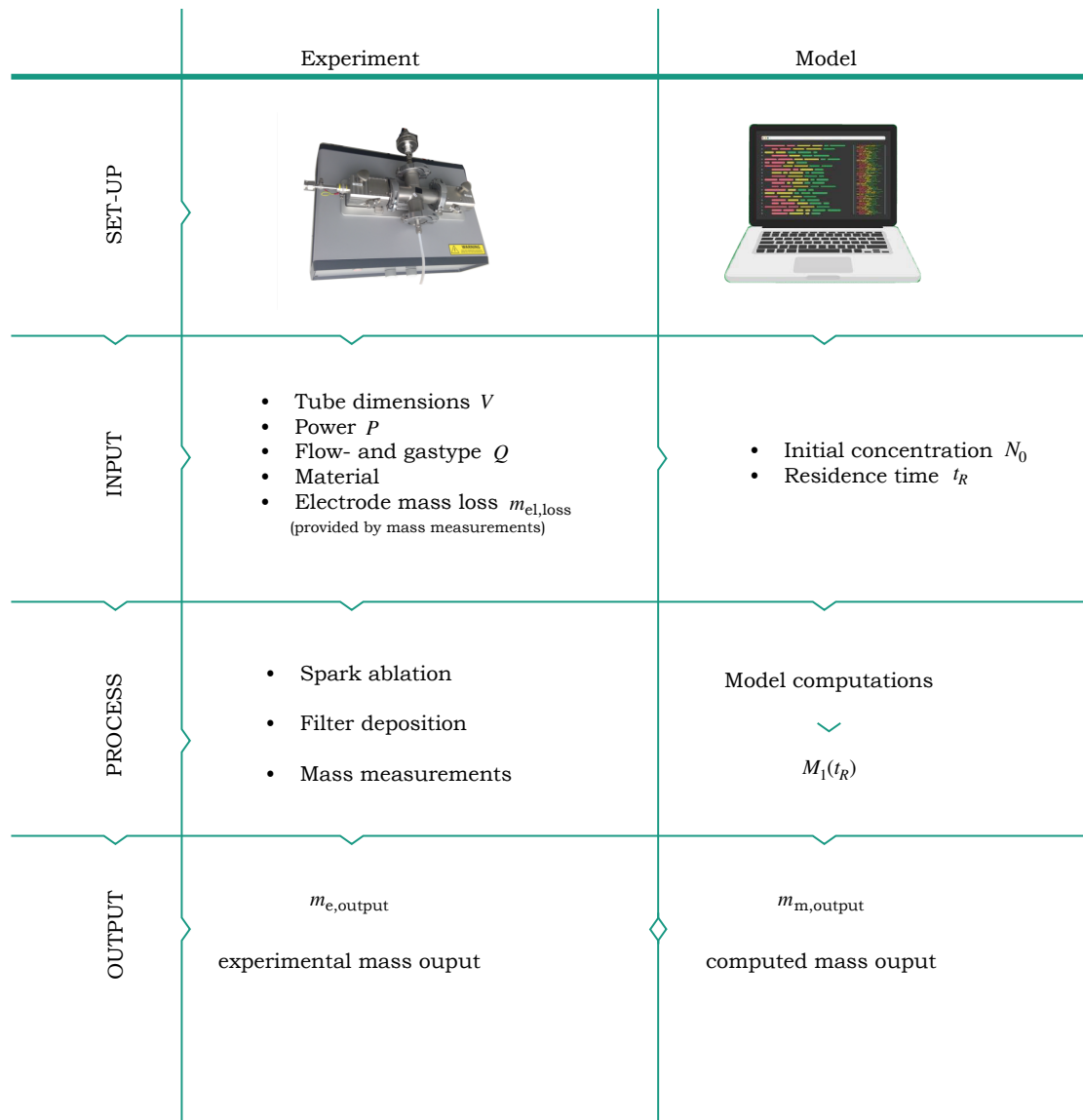


Figure C.1: Diffusion validation using cross flow, gold electrodes and argon gas.

C.2.2. RESULTS

Figure C.2 shows that the mass output derived by the model is much higher than it is experimentally measured under equivalent conditions. This suggests that the theoretically derived sink term is too weak to obtain reliable predictions for the nanoparticle concentration of the VSP-G1 when using cross flow.

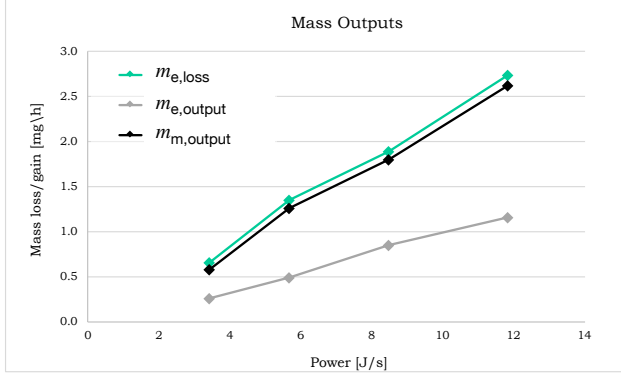


Figure C.2: mass loss of electrode corresponding to mass of N_0 (green), experimental mass output (grey), modelled mass output (black)

C.2.3. POSSIBLE EXPLANATIONS

Recall the sink term:

$$\frac{dn_{sink}(v)}{dt} = -\frac{4.117D(v)}{R^2\pi a}C(v)n(v), \quad (C.2)$$

which was derived from:

$$\frac{n}{n_0} = \exp\left(-\frac{4.117DL}{R^2\bar{u}}\right),$$

There are possible explanations for under-approximated diffusion effects in the current model:

1. The diffusion coefficient is interpreted incorrectly due to the absence of transition regime parameters defined by Rader [4].
2. The residence time is under-approximated.
3. Particles deposit onto surface areas inside the system that are not taken into account in the model.

WRONG DIFFUSION COEFFICIENT

The diffusion term is defined by [8] and written terms of particle volume:

$$D(v) = \frac{K_{Co}}{4\sqrt[3]{\frac{3}{4\pi}}\pi} v^{-\frac{1}{3}} \quad (C.3)$$

$$C(v) = 1 + \frac{\lambda}{\sqrt[3]{\frac{3}{4\pi}}} v^{-\frac{1}{3}} \left(\alpha + \beta \exp\left(-\frac{\gamma}{\lambda} \sqrt[3]{\frac{3}{4\pi}} v^{\frac{1}{3}}\right) \right) \quad (C.4)$$

Section 5.2 showed that particles do enter the transition regime for initial conditions that are comparable to those of this experiment ($N_0 \approx 1E19m^{-3}$, $t_R > 0.5s$). The parameters for Cunningham in the transition regime according to [4] are: $\alpha = 0.1227$, $\beta = 0.42$, $\gamma = 0.85$. The affect this has on the diffusion coefficient $D(r)$ is shown in figure ?? (- -).

The diffusion coefficients using both Cunningham factors are plotted for a radius range that is applicable for this experiment: $1nm < r_p < 15nm$. Since the diffusion coefficient has a 1:1 impact on the sink term, and the difference between D_{model} and D_{Rader} is negligible, the first option is not a possible explanation for the gap between experimental and modelled diffusion mass loss.

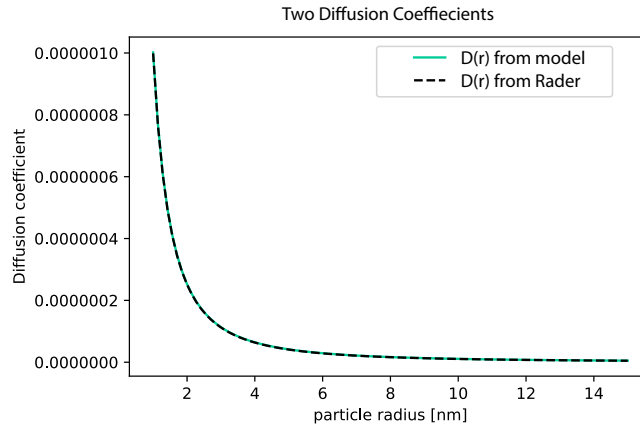
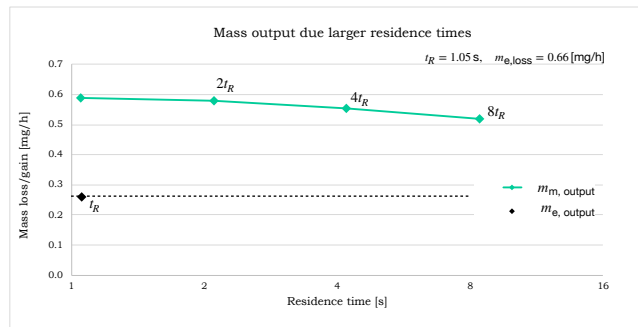


Figure C.3: Diffusion coefficients for transition- and free molecular regime

UNDER-ESTIMATED RESIDENCE TIME

The residence time could be underestimated due to the presence of turbulent flow. A longer residence time allows more particles to be affected by diffusion and therefore contributes to a greater mass loss and smaller mass output. Figure C.4 shows the affect of a larger residence time on the modelled mass output with respect to the experimental data. Clearly, the impact of a longer residence time on the mass loss (green) is still too weak to approach the experimental results (black). The largest residence time corresponds to 8.4 s which makes it eight times larger than the original t_R , this is physically nearly impossible to realize. Hence, even though the residence time could be overestimated, it is not an explanation for the extreme experimental mass loss.

Figure C.4: An increase in t_R does not close the gap between experimental- and modelled mass outputs.

UNMODELLED SURFACE AREAS

The third possible explanation is the large deposition of particles onto surface areas inside the system that are not taken into account in the model.

Examples of such areas are the electrode holders and the adapter between the G1 and the tube (Figure 6.6). Recall that for cross flow the diameter inside the reactor chamber is approximately 10 times larger than the tube diameter. This sudden change can result in particles depositing and sticking onto the surface of the adapter, rather than gradually flowing into the tube. This change in diameter is taken into account when calculating the residence time, but is not directly incorporated into the sink term.

The impact of this effect is quantified with an amplification factor which strengthens the models sink term and closes the mass gap. The amplification factor is determined iteratively for each experiment such that when it is multiplied with the the sink term the model mass output matches the experimental mass output.

$$\frac{d\widetilde{M}_{k,sink}}{d\tau} = A_a \tilde{l}_k$$

Where A_a is an empirical amplification factor derived with linear regression.

$$A_a = 3N_0 \cdot 10^{-x} + 5.5985 \quad (C.5)$$

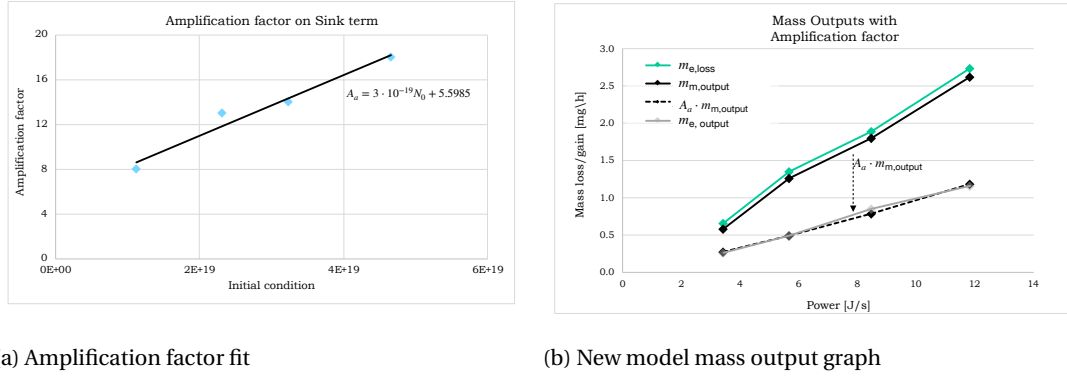


Figure C.5: Mass Ouput with A_a

Model test runs have shown that it runs into errors for $x < 19$ in Equation C.5. This is due to the fact that the sink effect becomes so large, that all particles are lost due to diffusion and there is no mass left to output.

It is also predicted that the flow has a greater impact on the sink term than the magnitude of the initial condition. Unfortunately, the current experiment was executed using a constant inflow and therefore it is unable to quantify this effect. Advised is to repeat the experiment with different flow rates and types, and to proceed with a flow and N_0 dependant function A_a . For the current research the amplification factor is excluded in further calculations.

C.3. PROPERTIES OF AIRBORNE PARTICLES FROM HINDS [1]

Particle diameter [μm]	Slip Correction Factor	Coagulation Coefficient [cm^3/s]
0.001	224.332	3.11×10^{-10}
0.0015	149.753	3.81×10^{-10}
0.002	112.463	4.40×10^{-10}
0.003	75.174	5.39×10^{-10}
0.004	56.530	6.21×10^{-10}
0.005	45.344	6.93×10^{-10}
0.006	37.888	7.56×10^{-10}
0.008	28.568	8.63×10^{-10}
0.01	22.976	9.48×10^{-10}
0.015	15.524	1.09×10^{-9}
0.02	11.801	1.15×10^{-9}
0.03	8.083	1.14×10^{-9}
0.04	6.229	1.07×10^{-9}
0.05	5.120	9.92×10^{-10}

Table C.2: Properties of Airborne Particles[1], Calculated for standard density spheres at 293 K and 101 kPa.